國立臺灣大學工學院土木工程學系

博士論文

Department of Civil Engineering

College of Engineering

National Taiwan University

Doctoral Dissertation

非整數動力學之下的隨機泥砂傳輸

Stochastic Suspended Sediment Transport by Fractional Dynamics

洪毓茹

Yu-Ju Hung

指導教授: 蔡宛珊 博士

Advisor: Christina W. Tsai, Ph.D.

中華民國 111 年 12 月

December, 2022

doi:10.6342/NTU202300192

國立臺灣大學博士學位論文
口試委員會審定書
National Taiwan University
Doctoral Dissertation Acceptance Certificate

非整數動力學之下的隨機泥砂傳輸

Stochastic Suspended Sediment Transport by Fractional Dynamics

本論文係 洪毓茹 君 (D05521007) 在國立臺灣大學土木工程學系完成之博士學位論文，於民國111年12月22日承下列考試委員審查通過及口試及格，特此證明

This is to certify that this Doctoral Dissertation is completed by 洪毓茹 (D05521007) during his/her studying in Department of Civil Engineering at National Taiwan University, and that the oral defense of this thesis/dissertation is passed on 2022/12/22 in accordance with decision of following committee members:

口試委員 Oral Defense Committee members：

蔡宛珊 (指導教授 Advisor)	蔡宛珊 Dec 22, 2022 11:53 EST
Rafik Absi	Rafik Absi Dec 22, 2022 12:39 GMT+1
謝平城	謝平城 Dec 22, 2022 19:05 GMT+8
周逸儒	周逸儒 Dec 23, 2022 13:05 GMT+8
余化龍	余化龍
游景雲	游景雲
何昊哲	何昊哲 Dec 23, 2022 09:31 GMT+8

系主任、所長 高宇甯 (簽名 Signature)

(Department Chair/Program Director)

doi:10.6342/NTU202300192

doi:10.6342/NTU202300192

Acknowledgements

First and foremost, I express my deepest gratitude to my advisor, Dr. Christina W. Tsai, for the exceptional guidance, encouragement, and support throughout my doctoral journey. Her expertise and mentorship have been invaluable in shaping my research and inspiring me to achieve my goals. I would also like to extend my sincere thanks to my committee members: Dr. Ping-Cheng Hsieh, Dr. Rafik Absi, Dr. Yi-Ju Chou, Dr. Hwa-Lung Yu, Dr. Gene Jiing-Yun You, and Dr. Hao-Che Ho for their critical feedback, and suggestions. Their contributions have been constructive in refining my research and making it what it is today. I would like to acknowledge the contributions of the civil engineering family, including the faculty, staff, and students, for providing me with a vibrant academic environment and the resources and facilities necessary for conducting my research. Finally, I would like to acknowledge the love and support of my family and lovely friends, who have been a constant source of inspiration and motivation. Without their unwavering support, this accomplishment would not have been possible. I dedicate this thesis to them with heartfelt gratitude and appreciation. As Alessandro Michele (2022) states: ” may you continue to feed on your dreams, the subtle and intangible matter that makes life worth living. May you continue to nourish yourselves with poetic and inclusive imagery, remaining faithful to your values. May you always live by your passions, blown by the wind of freedom.”

doi:10.6342/NTU202300192

doi:10.6342/NTU202300192

摘要

工程實務上，懸浮泥砂的濃度為水質和水庫管理的重要因子。汙染物會附著於懸浮泥砂上，藉由紊流的擴散機制造成汙染的傳播，而懸浮泥砂本身亦會對水質造成影響，其沉降後對水庫造成的淤積也是一大工程問題。若對懸浮泥砂顆粒的運動機制有更深入的探討，便能更準確地估計懸浮泥砂濃度，並且藉由了解泥砂顆粒的運動軌跡，便能對潛在的汙染區域提前進行預防及整治。在科學理論中，泥砂受水流作用發生運動，泥砂運動又會影響水流性質，兩者相互影響，運動機制複雜。在過往研究中，懸浮泥砂顆粒一般使用平流擴散方程 (advection-diffusion equation, ADE) 或泥砂率定曲線 (sediment rating curves) 來做定率的懸浮泥砂濃度估計。然而，由於紊流的不穩定，水流中的泥砂不僅僅會順著水流方向運動，也會在水體中進行隨機的擴散。本研究利用序率隨機模擬，更深入地以機率方法描述泥砂顆粒在明渠流中，受到紊流影響的運動行為，並以科學方法量化泥砂濃度和其運輸率的變化及不確定性。本研究考量不同尺度紊流結構對懸浮泥砂運動所造成的影響，提出一序率模型: 非整數布朗運動驅動之隨機擴散粒子追蹤模型 (fractional stochastic differential diffusion particle tracking model, FSD-PTM)，此模型旨在模擬明渠流中懸浮泥砂顆粒的隨機運動軌跡，並利用蒙地卡羅方法計算紊流中懸浮泥砂的濃度與輸砂率。此模型為一進階的隨機拉格朗日模型 (Lagrangian model)，可以描述底床邊界附近，受到在時間上具有持續性之紊流擬序結構 (time-persistent turbulent coherent structures) 的影響，懸浮泥砂粒子所

doi:10.6342/NTU202300192

反映出的隨機運動行為。本研究利用實驗數據與模型模擬結果 (系統平均速度和泥砂濃度等) 進行模型驗證。模擬結果除一般定率模型能模擬之懸浮泥砂濃度和輸砂率外，還可量化濃度與輸砂率的變化率及其相對應之不確定性。在水質泥砂濃度標準已知的情況下，方能提供時間和空間上所對應的超越機率值，即為水質汙染風險機率，應用於風險管理範疇中評估風險容忍度與制定應對政策時，可提供決策者有效的風險評估依據。

關鍵字：隨機泥砂傳輸模型、隨機擴散粒子追蹤模型、非整數布朗運動、紊流擬序結構

doi:10.6342/NTU202300192

Abstract

The study focuses on the Lagrangian particle tracking of suspended sediment particles whose motions are strongly coupled with surrounding turbulent flows. The diffusion of suspended particles is often linked to turbulence diffusion theories. The high irregularity and protean properties of turbulence generally lead to the usage of Brownian diffusion. It implies that the spreading of suspended sediment particles is normally distributed and embeds independent properties in particle motions. However, the non-Gaussian phenomenon in sediment movements has been observed and recognized during the last decades. The sediment-laden flow experiments have suggested that coherent structures in turbulent shear flow strongly impact particles' suspension near the boundary. This study proposes an advanced Lagrangian particle tracking model, whose driven fluctuation process is the fractional Brownian motion (FBM). By introducing the fractional stochastic process to the particle tracking model (PTM), the correlated increments aim to describe anomalous suspended sediment particles' movements resulting from in-

doi:10.6342/NTU202300192

termittent and time-persistent coherent turbulent structures near the boundary. The proposed model is applied to simulate suspended sediment transport in two-dimensional open channel flow. Via Monte Carlo simulation, the ensemble statistics results are presented, including mean, variance, skewness of particle positions, and particle velocity fluctuations. The anisotropic sediment behaviors can be found in the probability density function (PDF) of particle velocity fluctuations at different water depths. Simulation results show improvements in the streamwise particle velocity profiles and in predicting sediment concentrations near the boundary.

Keywords: particle tracking model, turbulent coherent structure, stochastic suspended sediment transport, anomalous transport by fractional process, fractional Brownian motion

doi:10.6342/NTU202300192

Contents

doi:10.6342/NTU202300192

doi:10.6342/NTU202300192

doi:10.6342/NTU202300192

doi:10.6342/NTU202300192

List of Figures

doi:10.6342/NTU202300192

doi:10.6342/NTU202300192

doi:10.6342/NTU202300192

doi:10.6342/NTU202300192

List of Tables

doi:10.6342/NTU202300192

doi:10.6342/NTU202300192

Chapter 1

Introduction

1.1 Anomalous diffusion in suspended sediment transport

Suspended sediment transport in open-channel flows is essential in engineering applications because of its high relevance to water quality control in ecosystems and sedimentation issues in reservoirs. Transport mechanisms of suspended sediment particles are inextricably bound to the carrying flows. Movements of suspended particles and turbulent flow structures are closely linked and mutually affected. The interplay between sediment particles and turbulent flows keeps challenging researchers and inspiring extensive field, laboratory, and numerical experiments. This study aims to propose an advanced Lagrangian particle tracking model which is capable of describing the anomaly of suspended sediment transport subject to the anisotropic turbulent forces.

Since the late 1960s, scientists have found the existence of streamwise velocity streaks in the vicinity of the boundary. The low-speed velocity streaks (or simply called streaks) are regions with lower flow velocities that lie between high-speed velocity zones. They are the results of the *bursting process*. A bursting process is developed from a lift-up of an

doi:10.6342/NTU202300192

eddy. When fluids move outward from the lower velocity region, the three-dimensional hairpin-shaped eddies then elongate, oscillate, and grow in spanwise and normal directions. The low-speed streaks with lower momentum fluids ejecting from the bottom are termed *ejections*. As they encounter the faster-moving fluids outside, the hairpin structures become unstable and cannot maintain their shape. When the structures burst out, collapse, and break down, it causes high-speed fluids inrush from the outer region toward the boundary, known as a *sweep*. Then a sweep causes a new low-speed velocity streak to move upward again. The whole bursting process is cyclic. The breakdown and reconstruction of the eddies cause positive and negative velocity fluctuations (Brandt and De Lange, 2008; Kline et al., 1967; Lee et al., 2014; Robinson, 1991; Smith and Metzler, 1983) and are responsible for sustaining and generating turbulence in the wall-bounded open-channel turbulent flow (Kline et al., 1967; Nakagawa and Nezu, 1981).

Ejections and sweeps are two significant coupled turbulent structures during a bursting process. Together they are known as *coherent structures*. While 'structure' implies something that is organized, 'coherent' has the meaning of consistency (Davidson, 2015). The wording 'coherent structures' indicates structures that exhibit correlation over a range of space or time. Recent turbulent visualization shows that in the near-wall region of wall-bounded shear flows, particularly the buffer and viscous sub-layers, turbulent flows are full of coherent structures called hairpin forests (Chen et al., 2021; Jiménez, 2018). Since sediment particles transport within turbulent flows, lots of field, laboratory, and numerical experiments have been conducted to establish and quantify the interactions among sediment motions with these turbulent flow structures. Jackson (1976) pointed out that in low-concentration flows, the bursting process is the primary fluid-dynamic mechanism for sediment suspension. Kaftori et al. (1995a,b) used neutrally buoyant polystyrene parti-

doi:10.6342/NTU202300192

cles with a specific density of 1.05 to investigate particle behaviors in the boundary layer. They presumed a funnel type of coherent structure and described how it affects particles' entrainment and deposition processes. Their experimental results suggest coherent structures significantly affect particles' behavior near the boundary. It was pointed out that the downward turbulence might bring particles toward the wall and cause deposition; on the opposite, the upward turbulence might lift the particle up and make it suspend. Ninto and Garcia (1996) studied the interaction between sediment and coherent flow turbulence. Their results indicate the ejections would induce the entrainment and lift up particles away from the bed. Cellino and Lemmin (2004) pointed out that ejections not only pick up the suspended particles but also carry and maintain the suspension of particles, thus playing an essential role in erosion.

Muste et al. (2005, 2009) used particle image and particle tracking velocimetry (PIV and PTV) to examine the influence of suspended particles' motion on open-channel turbulence. Two particle densities with diameter 0.23 mm in dilute concentrations were used in the experiments: natural sand (NS) with a specific density of 2.65 and neutrally-buoyant sand (NBS) with a specific density of 1.05. They found that the existence of particles reduces the bulk flow velocity irrespective of particle density. Noguchi and Nezu (2009) used different particle sizes from 0.25 to 1 mm with specific density 1.2 and 1.5 to investigate the particle-turbulence interactions. They observed that stronger ejection events would increase the local particle concentrations while stronger sweep events decrease them. They pointed out that sediment transport is more active with stronger ejections. Using high-frequency acoustic Doppler velocimeters (ADVs), Salim et al. (2017) conducted flume experiments in fluvial conditions to highlight the importance of instantaneous turbulent events on sediment resuspension. They pointed out that the bursting event induces

doi:10.6342/NTU202300192

sediment resuspension despite the shear stress being smaller than the mean critical threshold for sediment particle with a diameter of 0.31 mm and specific density 1.905. Salim and Pattiaratchi (2020) used field measurements to examine the coherent structures of sediment resuspension in wave-dominate near-shore regions. Their analysis indicated that sediment flux is dominated by ejection and sweep events and was confirmed by wavelet analysis.

The proceeding remarks implicate the significance and influence of coherent structures on suspended sediment movements near the boundary. This research introduces fractional process into PTMs to describe temporally correlated probabilistic trajectories when suspended sediment particles dwell in turbulent coherent structures.

1.2 Research aim and research objectives

As mentioned in the introduction, recent advanced turbulent visualization techniques and high-resolution experimental observations open a window to a more comprehensive understanding of the interplay between sediment particles and turbulent structures. As such, more and more researchers have observed the non-Gaussian fluctuations in sediment particle movements, and these studies have suggested that suspended sediment particles' movements are not totally random, especially in time-or-spatial persistent turbulent structures. In other words, when the turbulent force acting on a suspended sediment particle is not isotropic, fluctuations of particle movements are non-Gaussian distributed. The aim of this research is to propose an advanced Lagrangian particle tracking model which is capable of describing the anomaly of suspended sediment transport subject to the anisotropic turbulent forces.

doi:10.6342/NTU202300192

In the study, coherent structures near the boundary are the target structures that cause non-Gaussian fluctuations. Therefore, this study hypothesizes that the prediction of the suspended particle velocity profile and concentration profile near the boundary will be improved by including the influence of coherent structure by means of dependent increments in the proposed fractional PTM. In order to provide a description of the anomaly in suspended sediment transport, the research objectives are listed as follows:

1. A conceptual model is proposed for suspended sediment transport accounting for the influence of coherent structures. The model provides a description that when a settable suspended sediment particle settles down to the inner layer in an open-channel flow, its movements might be affected by the hairpin vortices consisting of coherent structures. If a suspended sediment particle encounters coherent structures, its activities are correlated. On the other hand, if a particle transports in the outer region or is not in coherent structures, the fluctuations are normally distributed.

2. A mathematical model is proposed to address individual suspended particles' trajectories. In order to simulate the sediment particles' non-Gaussian fluctuations, a fractional process, the fractional Brownian motion (FBM), is introduced to PTM. The study proposes a fractional diffusion particle tracking model (FSD-PTM) aiming to describe the anomalous diffusive movements of individual suspended sediment particles subject to the anisotropic turbulent forces.

3. The implementation of the governing equation is proposed for the numerical simulation of suspended sediment transport. A suitable numerical scheme is applied for numerical discretization. Physical processes of suspended sediment transport are introduced to the FSD-PTM.

doi:10.6342/NTU202300192

4. The proposed FSD-PTM is validated by experimental data. In order to confirm that the proposed model actually achieves its intended purpose, simulation outcomes are validated by experimental data proposed by Muste et al. (2005).

5. Finally, potential applications are discussed to explore and extend the model's applicability.

1.3 Overview of the thesis

Following the introduction, background information on physical processes for individual suspended sediment particle transport in open-channel flow is provided. It includes a brief overview of open-channel flow turbulence. Then a more detailed review of coherent structures, including their generation mechanisms and properties, is carried out. It is followed by how a Lagrangian description of individual suspended sediment particles can be provided by the stochastic diffusion particle tracking model (SD-PTM).

Regarding the research objectives, the following chapter 3 introduces the study's conceptual model and the proposed FSD-PTM. In chapter 3, a conceptual model is proposed to describe sediment particles' movements affected by anisotropic turbulent velocity fluctuations in the inner layer of open-channel turbulent flows. Then chapter 3 introduces the mathematical model of the proposed fractional model, which aims to interpret the anomalous diffusive movements of individual suspended sediment particles. The governing equation is a stochastic differential equation (SDE) driven by fractional Brownian motion (FBM). The incremental process of the FBM achieves the correlated increments of particles caused by the influence of coherent structures.

Chapter 4 uses the proposed FSD-PTM to simulate suspended sediment transport

doi:10.6342/NTU202300192

in open-channel flows. Flow conditions and particle properties used for simulation are reviewed. Ensemble simulation results of sediment particle velocity and concentration profiles are used to validate the proposed model.

Chapter 5 discusses how a Hurst parameter can be utilized to interpret the long-range influence of a flow event on suspended sediment transport. Discussions and further potential modifications are provided for future applications. For demonstration, though embryonic, the proposed FSD-PTM attempts to provide an application for suspended sediment transport in a geophysical-scaled flow event. Finally, conclusions and future recommendations are drawn in chapter 6.

doi:10.6342/NTU202300192

doi:10.6342/NTU202300192

Chapter 2

Overview of the physical processes in suspended sediment transport in open channel turbulent flows

In this chapter, an overview of open-channel flow turbulence is reviewed including the flow velocity profile in a steady, fully-developed open-channel flow. Then special attention has been put to the characteristics of coherent flow structures near the boundary. This is followed by an introduction to a Lagrangian particle tracking model, which is the foundation of the proposed research model. Finally, the determination of the particle's diffusive behavior is provided.

2.1 Turbulence in open-channel flow

It is generally accepted that flows in natural rivers or artificial channels are often turbulent. Turbulence is characterized by its irregular and chaotic properties both in time and space. In turbulent flows, the wide range of eddies' length and time scale cause in-

doi:10.6342/NTU202300192

termittency and random fluctuations in physical quantities, such as flow velocity. The intensity of turbulent velocity fluctuations decides how efficiently turbulence mixes energy, momentum, and substance. Specifically, the mixing process in turbulent flows not only transfer flow momentum but exchange sediment particles between adjacent flow layers. Therefore, understanding turbulence in open-channel flow is essential for further understanding suspended sediment transport in open-channel flow.

2.1.1 Reynold's decomposition and RANS equation

For an incompressible flow, the mass conservation can be described by the continuity equation in tensor form using Einstein's summation convention,

$$\frac{\partial u_i}{\partial x_i} = 0. \tag{2.1}$$

where u_i represents the instantaneous flow velocity in i-direction. The Navier-Stokes equation can describe the momentum balance in flow motion,

$$\frac{\partial u_i}{\partial t} + u_j \frac{\partial u_i}{\partial x_j} = g_i - \frac{1}{\rho}\frac{\partial P}{\partial x_i} + \nu \frac{\partial^2 u_i}{\partial x_j^2}, \tag{2.2}$$

where g_i denotes body force such as gravity force, $\frac{\partial P}{\partial x_i}$ denotes the pressure gradient, and ν is the kinematic viscosity.

Theoretically, when sufficient initial and boundary conditions are prescribed, the Navier-Stokes equation can be solved numerically called direct numerical simulation (DNS). The solutions of DNS contain information from the mean flow and turbulence of all scales. However, resolving such wide ranges of length and time scales in turbulent flow with a high Reynolds number will cost a lot of computational resources. Therefore, for practi-

doi:10.6342/NTU202300192

cal applications, it is preferred to know essential pieces of information from mean flow motion, that is, to solve the equation without resolving all turbulence fluctuations. In turbulent flows, hydrodynamic quantities such as the flow velocity at a given point in space will not remain constant but always fluctuates along with time. Reynolds (1895) proposed *Reynolds decomposition* to describe hydrodynamic quantities by separating the time-averaged value from its highly irregular fluctuations. The instantaneous velocity can be expressed as,

$$u_i = \bar{u}_i + u_i', \tag{2.3}$$

where $\bar{u}_i$ represents the time-averaged flow velocity in i-direction, and is defined as,

$$\bar{u}_i = \frac{1}{t_\infty} \int_{t_0}^{t_0+t_\infty} u_i \, dt. \tag{2.4}$$

The u_i' in Eq. 2.3 denotes the velocity fluctuation whose time-average value is always zero. For most practical applications, it would be enough to solve the time-averaged equations of fluid flow motion without solving all scales of turbulence. Therefore, after applying the Reynolds decomposition to flow velocity, body forces, and pressure terms, we can decompose the Navier-Stokes equation by averaging in time to get the time-averaged Navier-Stokes equation. After eliminating the zero-value terms due to time-averaged fluctuation and continuity terms, the time-averaged momentum equation using Reynolds decomposition is called the Reynolds averaged Navier-Stokes equation (RANS) and can be written as,

$$\frac{\partial \bar{u}_i}{\partial t} + \bar{u}_j \frac{\partial \bar{u}_i}{\partial x_j} = g_i - \frac{1}{\rho}\frac{\partial \bar{P}}{\partial x_i} + \nu \frac{\partial^2 \bar{u}_i}{\partial x_j \partial x_i} - \frac{\partial \overline{u_i' u_j'}}{\partial x_j}, \tag{2.5}$$

where

$$\frac{\partial^2 \bar{u}_i}{\partial x_j \partial x_i} = \frac{\partial^2 \bar{u}_i}{\partial x_j \partial x_i} + \cancelto{Continuity}{\frac{\partial^2 \bar{u}_j}{\partial x_j \partial x_i}} = \frac{\partial}{\partial x_j}\left(\frac{\partial \bar{u}_i}{\partial x_j} + \frac{\partial \bar{u}_j}{\partial x_i}\right).$$

doi:10.6342/NTU202300192

The RANS equation describes the momentum change of mean flow motion. Compare the Navier-Stokes equation (Eq. 2.2) with the RANS equation (Eq. 2.5), an additional last term pops out and causes the closure problem. By multiplying the flow density ρ, the unit of RANS changes from acceleration to stress unit,

$$\rho\frac{\partial \bar{u}_i}{\partial t} + \rho\bar{u}_j\frac{\partial \bar{u}_i}{\partial x_j} = \rho g_i + \frac{\partial \bar{P}}{\partial x_i} + \frac{\partial}{\partial x_j}\left[\mu\left(\frac{\partial \bar{u}_i}{\partial x_j} + \frac{\partial \bar{u}_j}{\partial x_i}\right) - \rho\overline{u_i' u_j'}\right], \tag{2.6}$$

where $\mu = \nu\rho$ is the fluid dynamic viscosity. $\mu\left(\frac{\partial \bar{u}_i}{\partial x_j} + \frac{\partial \bar{u}_j}{\partial x_i}\right)$ is the mean viscous stress tensor. The last term, $-\rho\overline{u_i' u_j'}$ aroused from the interactions of turbulence with the mean flow is referred to as the *turbulence stress* or *Reynolds stress*. The Reynolds stress represents the average momentum flux due to turbulent velocity fluctuations.

The intensity of turbulent fluctuations is quantified in terms of the normal Reynolds stress components denoted by the symbol k,

$$k = \frac{1}{2}\overline{u_i' u_i'} \tag{2.7}$$

where k is the kinetic energy of the turbulence fluctuations per unit mass.

Turbulent eddy viscosity

In order to deal with the closure problem of the RANS equation, the additional Reynolds stress term should be approximated and modeled as functions of the mean flow. Boussinesq (1877) was the first one trying to solve the problem by introducing the concept of *eddy viscosity*, μ_t. The turbulent models solving μ_t to calculate Reynolds stress are called eddy viscosity models. Boussinesq approximation is an analogy with the molecular viscosity in the kinetic theory of gas, i.e., the Brownian motion. Brownian motion

doi:10.6342/NTU202300192

describes the gas particles randomly moving inside a box. The individual gas particles collide and bounce off, thus exchanging momentum energy. The Boussinesq approximation assumed the turbulent fluctuations behave the same ways as the gas particles. The turbulent viscosity μ_t captures the flow features related to the momentum transfer caused by the turbulent mixing process. The Boussinesq approximation of μ_t in a three-dimensional incompressible turbulent flow is shown as following equation,

$$-\rho\overline{u_i'u_i'} = \mu_t\left(\frac{\partial\bar{u}_i}{\partial x_j} + \frac{\partial\bar{u}_j}{\partial x_i} - \frac{1}{3}\frac{\partial\bar{u}_k}{\partial x_k}\delta_{ij}\right) - \frac{2}{3}\rho k\delta_{ij}, \tag{2.8}$$

where δ_{ij} is the Kronecker delta, defined as $\delta_{ij}(i=j)=1$, otherwise $\delta_{ij}(i\neq j)=0$. k is the kinetic energy of the turbulence fluctuations defined in Eq. 2.7.

In a two-dimensional turbulent flow with thin boundary layer, the Boussinesq approximation can be simplified as,

$$-\rho\overline{u'w'} \approx \mu_t\frac{\partial\bar{u}}{\partial z}, \tag{2.9}$$

where u' and w' represent the velocity fluctuations in streamwise and vertical directions, and $\bar{u}$ is the time-averaged streamwise velocity. Once μ_t has been calculated by turbulence models, the Reynolds stresses can then be used to solve the RANS equation.

Prandtl mixing length model

Prandtl (1925) introduced the mixing length concept for the Boussinesq approximation in a flow near a solid boundary. The mixing length theory uses the physical intuition of length, representing the distance a fluid particle needs to traverse by turbulence momentum before it becomes blended in with neighboring layers. The length l is referred

doi:10.6342/NTU202300192

to the *mixing length*. One assumption is that the velocity fluctuation magnitudes in the streamwise and vertical directions are of the same order,

$$u' \approx w' \approx l\frac{\partial \bar{u}}{\partial z}. \tag{2.10}$$

The Reynolds stress in the Prandtl mixing length model can be approximated as,

$$-\rho\overline{u'w'} = \rho l\frac{\partial \bar{u}}{\partial z} l\frac{\partial \bar{u}}{\partial z}. \tag{2.11}$$

Then according to Boussinesq approximation in Eq. 2.10, the eddy viscosity is

$$\mu_t = \rho l^2 |\frac{\partial \bar{u}}{\partial z}|. \tag{2.12}$$

For the region outside the boundary layer, it is assumed that turbulent effect dominates and are not affected by the viscosity. Turbulent features though differ in length and time scales, are similar. On the other hand, near the wall boundary with a no-slip boundary condition, the mixing length must decrease to zero as no fluid particle can transport through the boundary. Thus eddy viscosity becomes zero on the boundary. The mixing length l is damped because the viscous effect dominates within the wall shear layer and according to Prandtl, l varies linearly with vertical length,

$$l = \kappa z \tag{2.13}$$

where κ is the von Kármán constant whose value is a universal constant 0.41 in flow over solid boundaries.

doi:10.6342/NTU202300192

2.1.2 Flow field in open-channel flows

In the research, we focus on two-dimensional open-channel flow in streamwise x- and vertical z-directions with flow velocity u and w, respectively. The assumptions of the flow conditions are listed below:

- The flow is steady, $\cancelto{0}{\frac{\partial}{\partial t}}$
- The physical quantity is fully-developed in streamwise direction, $\cancelto{0}{\frac{\partial}{\partial x}}$, and the flow depth remains constant h
- The slope S_0 is small enough that it is parallel to streamwise direction, $S_0 \approx \sin\theta$, and thus $g_z = -g\cos\theta$ and $g_x = g\sin\theta$
- The mean vertical flow velocity is zero, $\bar{w} = 0$

Then for a two-dimensional, steady, uniform flow, the RANS equation (Eq. 2.5) in x- and z-directions can be simplified,

$$\cancel{\frac{\partial \bar{u}}{\partial t}} + \bar{u}\cancel{\frac{\partial \bar{u}}{\partial x}} = g_x - \frac{1}{\rho}\frac{\partial \bar{P}}{\partial x} + \nu\left(\cancel{\frac{\partial^2 \bar{u}}{\partial x^2}} + \frac{\partial^2 \bar{u}}{\partial z^2}\right) - \left(\cancel{\frac{\partial \overline{u'u'}}{\partial x}} + \frac{\partial \overline{u'w'}}{\partial z}\right), \text{ and} \tag{2.14}$$

$$\cancel{\frac{\partial \bar{w}}{\partial t}} + \bar{w}\cancel{\frac{\partial \bar{w}}{\partial z}} = g_z - \frac{1}{\rho}\frac{\partial \bar{P}}{\partial z} + \nu\left(\cancel{\frac{\partial^2 \bar{w}}{\partial x^2}} + \cancel{\frac{\partial^2 \bar{w}}{\partial z^2}}\right) - \left(\cancel{\frac{\partial \overline{w'u'}}{\partial x}} + \frac{\partial \overline{w'w'}}{\partial z}\right). \tag{2.15}$$

To calculate $\bar{P}$, use the boundary conditions $\bar{P}(z = h) = 0$ and $\overline{w'w'}(z = h) = 0$ on z-component of the RANS equation Eq. 2.15, we can get

$$\bar{P}(z) = \rho g(h - z)\cos\theta - \rho\overline{w'w'}\,|_z\,. \tag{2.16}$$

Substituting Eq. 2.16 into x-component of the RANS equation Eq. 2.14 can be rearranged

doi:10.6342/NTU202300192

into

$$-\frac{\mathrm{d}\tau}{\mathrm{d}z} = -\frac{\mathrm{d}}{\mathrm{d}z}\left[\mu\frac{\mathrm{d}\bar{u}}{\mathrm{d}z} + (-\rho\overline{u'w'})\right] = \frac{\tau_0}{h}, \tag{2.17}$$

where $\tau_0 = \rho g h S_0$ is the bed stress. From the right hand-side of Eq. 2.17, the terms inside the square bracket are the summation of the shear stress from viscosity and turbulence, which is the total shear stress τ at z. Therefore, the relationship between bed shear stress τ_0 and total shear stress τ can be obtained,

$$\tau = \left(1 - \frac{z}{h}\right)\tau_0 \tag{2.18}$$

With a completely damped turbulent effect and a negligible pressure gradient inside the viscous sublayer, the shear stress is assumed to be constant. After knowing how the shear stress distributes, we can then find the velocity distribution in open-channel flow with classical turbulence theory, i.e., Boussinesq approximation and Prandtl's mixing length.

doi:10.6342/NTU202300192

Flow velocity profile

A flow filed is classified into three layers: viscous sublayer, turbulent wall shear layer including buffer layer and turbulent outer layer. The non-dimensional vertical distance $z^+ = zu_*/\nu$ and $\tilde{z} = z/h$ is used for distinguish different layers as shown in Fig. 2.1 and Table 2.1.

Table 2.1: Division of turbulent flow structures in open-channel flows.

Classification	Region	Velocity distribution
Viscous sublayer	$z^+ > 5$	$u^+ = z^+$
Turbulent wall shear & buffer layer	$z^+ > 5,\ \tilde{z} < 0.2$	$u^+ = \frac{1}{\kappa} \ln \frac{z}{z_0}$
Turbulent outer layer	$\tilde{z} > 0.2$	$u^+ = \frac{1}{\kappa} \ln \frac{z}{z_0} + \frac{2\Pi}{\kappa} sin(\frac{\pi \tilde{z}}{2})$

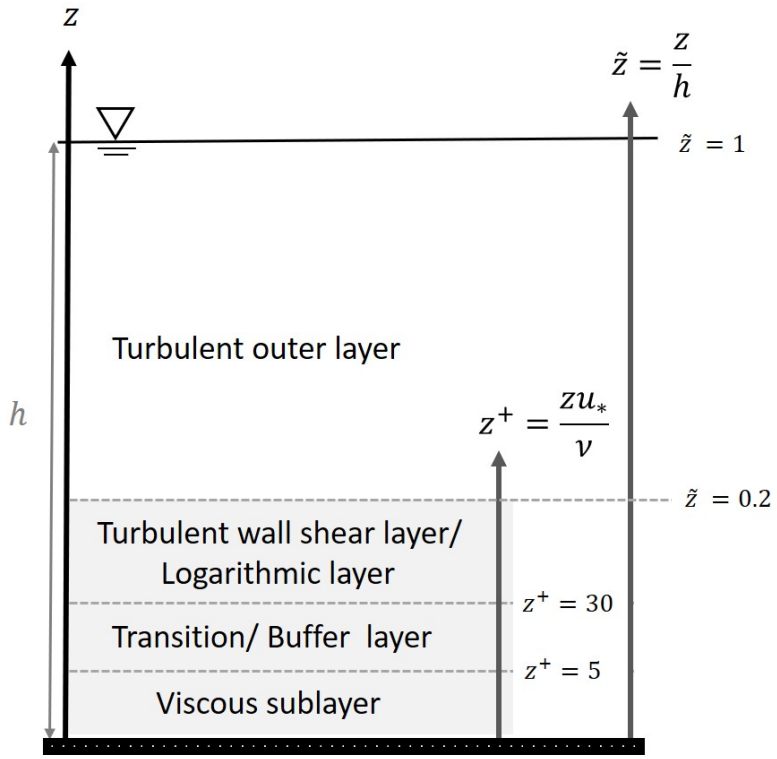

Figure 2.1: Division of turbulent open-channel into layers (not to scale).

doi:10.6342/NTU202300192

Viscous sublayer ($z^+ < 5$)

Viscous sublayer, also know as laminar sublayer, is a thin layer adjacent to the no-slip boundary where viscosity dominates. With a completely damped turbulent effect and a negligible pressure gradient inside the viscous sublayer, the viscous shear stress is assumed to be constant and equal to the bed stress, $\tau_0 = \rho u_*^2$.

$$\tau = \mu \frac{\mathrm{d}\bar{u}}{\mathrm{d}z} = \rho u_*^2. \tag{2.19}$$

Integrating Eq. 2.19 and applying the no-slip boundary condition, i.e., $\bar{u}(z = 0) = 0$, yield the linear velocity distribution in the region $z^+ < 5$,

$$u^+ = \frac{\bar{u}}{u_*} = \frac{u_* z}{\nu} = z^+. \tag{2.20}$$

where $u^+ = \bar{u}/u_*$.

Logarithmic layer ($z^+ > 30$, $\tilde{z} < 0.2$)

The logarithmic layer, also known as the turbulent wall shear layer, is where the total stress contains only the turbulent shear stress. According to the Prandtl mixing length theory in Eq. 2.11, the turbulent stress can be approximated

$$\tau = \rho l^2 \left(\frac{\partial \bar{u}}{\partial z} \right)^2 = \rho u_*^2. \tag{2.21}$$

Substituting the Prandlt length into Eq. 2.13 and integrating with the boundary condition $\bar{u}(z = z_0) = 0$, yield a logarithmic velocity distribution,

$$u^+ = \frac{1}{\kappa} \ln \frac{z}{z_0}, \tag{2.22}$$

doi:10.6342/NTU202300192

where z_0 denotes the reference height. The reference height is where the time-averaged streamwise velocity is zero. Since the zero velocity is related to the roughness of the boundary, z_0 is determined by the roughness Reynolds number, also known as shear Reynolds number, $\mathrm{Re}_* = u_* k_s/\nu$. The effective sand roughness height k_s introduced by Nikuradse (1932) assumes that a solid boundary is covered by a layer of sediment particles lining up as closely as possible. The value of k_s related to the diameter of sediment particles can be determined by experiments. Experimental findings use shear Reynolds number Re_* to classify flows in to smooth, rough, and transitional flow regimes as shown in Fig. 2.2.

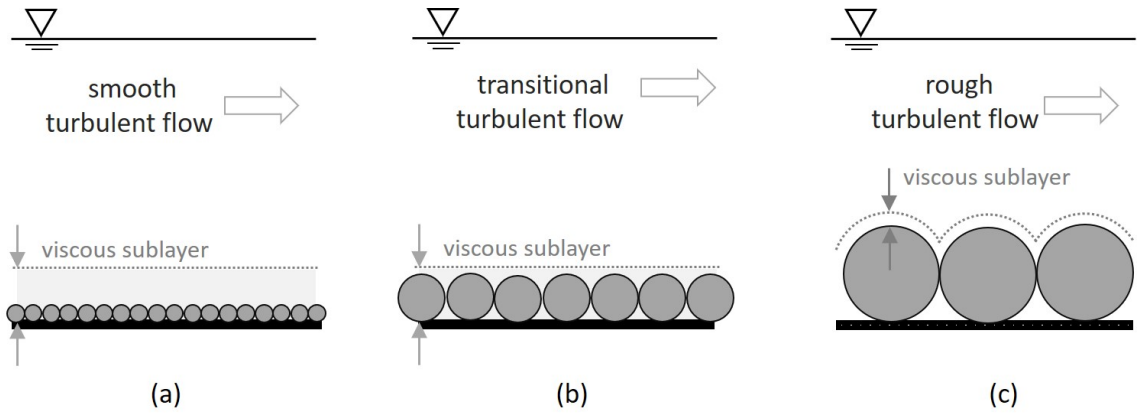

Figure 2.2: Three flow regimes (a) Smooth, (b) transition, and (c) rough flows.

Table 2.2: Determination of different flow regimes and their corresponding reference height.

Flow regimes	Re_*	z_0
Smooth	$\mathrm{Re}_* < 5$	$z_0 = 0.11\frac{\nu}{u_*}$
Transition	$5 < \mathrm{Re}_* < 70$	$z_0 = 0.11\frac{\nu}{u_*} + \frac{k_s}{30}$
Rough	$\mathrm{Re}_* > 70$	$z_0 = \frac{k_s}{30}$

doi:10.6342/NTU202300192

For hydraulically smooth flow, the roughness height related to the particle diameter on the boundary is much smaller than viscous sublayer thickness. As shown in Fig. 2.2(a), the particles are submerged in the viscous sublayer. It indicates the flow outside the viscous sublayer will not be affected by the boundary roughness but only fluid viscosity. In Fig. 2.2(b) shows the transition flow regime. The thickness of the viscous sublayer and roughness height is of a similar order. In such a case, flow velocity will be affected by fluid viscosity and boundary roughness. Compared with smooth and transition flow, the rough flow regime in Fig. 2.2(c) illustrates the situation that roughness height is larger than the thickness of the viscous sublayer. In such a case, the eddies caused by the boundary roughness will impact the turbulent shear layer. Table 2.2 lists the determination of z_0 according to different flow regimes based on the different decisive Re_* value.

The transition buffer layer ($5 < z^+ < 30$ **)**

The buffer layer is where the viscous sublayer transits to the turbulent wall shear layer. In the buffer layer, both viscous shear and turbulent shear stress are essential, and here is also known as the turbulence-generation layer. In some divisions of turbulent open-channel flow, the buffer layer is a region above the viscous sublayer and below the outer layer. Therefore, besides the empirical equations, the flow velocity profile in this layer often adapts the logarithmic equation (Eq. 2.22).

The turbulent outer layer ($1 > \tilde{z} > 0.2$ **)**

The turbulent outer layer is a region where turbulence dominates. Turbulent shear stress responds to momentum transport in this layer, and viscous shear stress is negligible. It seems the assumption is similar to the turbulent wall shear layer; however, researchers

doi:10.6342/NTU202300192

Table 2.3: Flow velocity profile using flume conditions proposed by Coleman (1986). Note that the Π in their research is around 0.19 under smooth boundary condition.

Flow conditions	Value	units
Flow depth	0.171	m
Shear velocity	0.041	m/s
Von Karman coefficient	0.433	-

find the velocity profile deviates from logarithmic velocity distribution, especially for $z^+ > 1000$. The velocity deviation is due to the constant shear stress and linear mixing length assumption. Coles (1956) added a wake function to the logarithmic velocity function in order to describe the increasing velocity. The velocity profile becomes,

$$u^+ = \frac{1}{\kappa} \ln \frac{z}{z_0} + \frac{2\Pi}{\kappa} \sin \frac{\pi \tilde{z}}{2}, \tag{2.23}$$

where Π is called as Cole's wake parameter. The wake function increases as the vertical distance increases and reaches the maximum value at the water surface. Π values are often decided by experiments.

For demonstration, Fig. 2.3 shows the velocity profiles using different equations introduced in different layers. In Fig. 2.3, the yellow line represents the dimensionless velocity $\bar{u}^+$ in the viscous sublayer calculated according to Eq. 2.20; the Red line represents logarithmic layer including the buffer and turbulent wall shear layer based on Eq. 2.22. Flow velocity deviation is shown as the orange dash line around z^+1000 which aims to represent the difference between Eq. 2.22 and Eq. 2.23.

doi:10.6342/NTU202300192

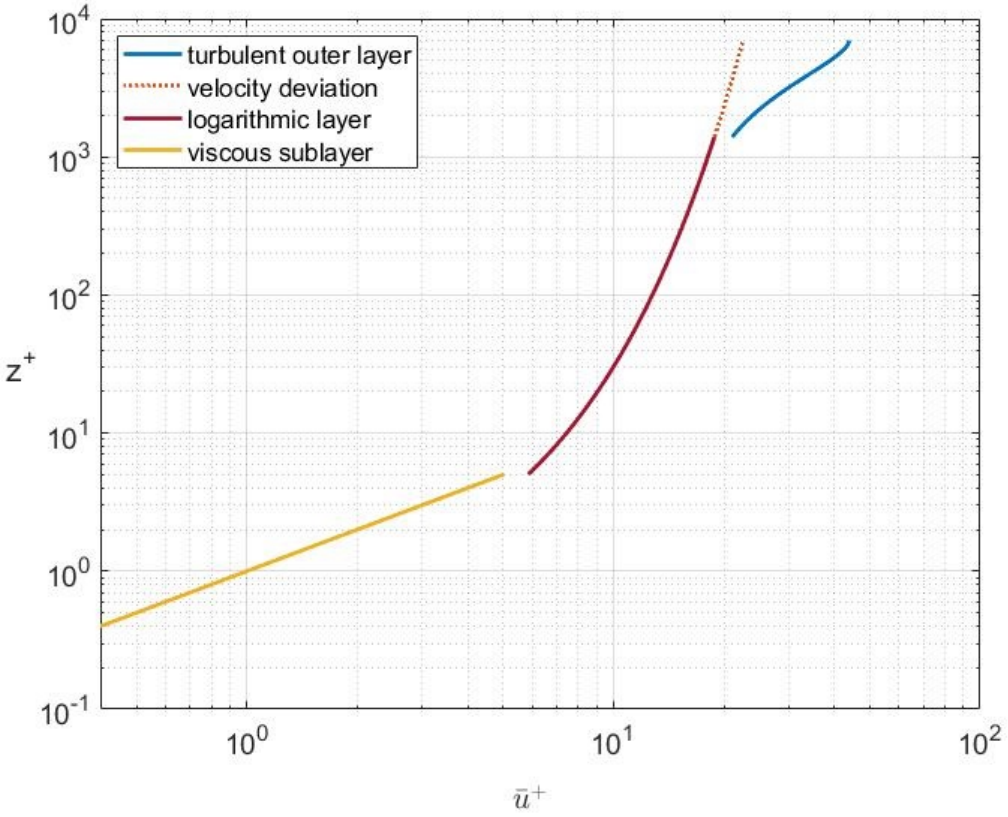

Figure 2.3: Demonstration of velocity profiles using flume conditions in Coleman (1986).

doi:10.6342/NTU202300192

2.2 Coherent structures in turbulent shear flow

"... these are irregular but repetitive eddy structures, or flow patterns, in time and space, with distinctive shapes and histories of formation, evolution, and dissipation."

John Southard

MIT

Before the 1960s, randomness had been always a prominent feature of turbulence because of the numerous time and length scales of turbulent eddies included. With the improvements in the measurement of the fluid flow field, i.e., velocimetry, experimental results indicate that the turbulence is not as random as initially assumed. Most statistical descriptions in the models of boundary layer turbulence reveal that turbulence fluctuations are the manifestation of the cyclic coherent turbulent structures, the spatially or temporally ordered turbulent motions in the vicinity of the boundary. As mentioned in the introduction section, these motions are responsible for the maintenance of turbulence in the boundary layer (Brandt and De Lange, 2008; Dennis, 2015; Kline et al., 1967; Lee et al., 2014; McKeon, 2017; Nakagawa and Nezu, 1981; Robinson, 1991; Smith and Metzler, 1983).

Before briefly elucidating the characteristics of coherent structures and how they are formed, it is necessary to emphasize that this research focuses on the smaller-scale turbulent coherent structures responsible for Reynolds stress up to 80% in the inner layer. Compared with the study's focus, there are large-scale coherent structures whose scales are related to the free-stream velocity that often governs the flow body's outer region. These larger-scale coherent structures are associated with the long-range velocity fluctu-

doi:10.6342/NTU202300192

ation caused by vortex pockets in the streamwise direction and are termed larger-scale motions (LSMs). The classification is based on the structures' influential region due to the wide range of length scale of a coherent structure (Davidson, 2015; Jiménez, 2018; McKeon, 2017).

Back to the coherent structures in the inner layer of a wall shear turbulent flow, the advent of direct numerical simulation (DNS) and improved experimental techniques, such as particle image velocimetry (PIV), have allowed not only a qualitative but also a quantitative measure of the flow field associated with these coherent structures. The followings are a brief introduction to the generation mechanism and general descriptions of coherent motions in the turbulent boundary layer.

2.2.1 Formation of coherent structures

The exquisite schematic diagram of the turbulence near the wall during a cyclic process in Fig. 2.4 is proposed by Salim et al. (2017), which is based on the conceptual model originated proposed by Hinze in 1975. Fig. 2.4 draws the formation and evolution of the hairpin vortice during a bursting process in a fully developed turbulence open channel flow. A structure, the low-speed streak, is formed due to the velocity difference at the interface. Faster-moving fluids cause the slower fluids to accelerate, which increases the instability of the flow and develops small-scale turbulence. Then as drawn in Fig. 2.5, fluids with lower velocity are lifted between the legs of the hairpin vortex. Fluids with lower momentum lift and cause an unstable shear layer. Then while the structure transports to downstream, it elongates, oscillates, and grows in spanwise and normal directions. The low-speed streaks with lower momentum fluids ejecting from the bottom are termed *ejections*. As upper parts of strcutres encounter the faster-moving fluids outside, the hairpin

doi:10.6342/NTU202300192

structures become unstable and cannot maintain their shape. When the structures burst out, collapse, and break down, it causes high-speed fluids inrush from the outer region toward the boundary, known as a *sweep*. Then a sweep causes new low-speed fluids to move upward again. The whole process is continuing and cyclical but not strictly periodic. Any stage of the cycle can start at a random time as the development of a vortex differs. Therefore, intermittency is one of the distinguished properties of turbulent coherent structures. Intermittent property is a result of random variation in the size and strength of hairpin vortices (Davidson, 2015; Dennis, 2015; Jiménez, 2018).

Observation of the bursting process often found low-speed streaks exist around $z^+ > 5$ above the boundary. z^+ denotes the wall-normal height in the wall unit, $z^+ = zu_*/\nu$. Fig. 2.6 depicts a bursting process with length scales in streamwise direction λ_1, spanwise direction λ_2, and wall normal vertical direction λ_3. Despite the high standard deviations from study to study, the observed height λ_3 was around $5 < z^+ < 30$. Specifically, the bursting process significantly influences the shear stress at $10 < z^+ < 15$. The length scale of a bursting process depends heavily on the strength of vortices, and it is often related to the boundary layer thickness. The larger scale coherent structures can be identified when the length in streamwise direction λ_1 is larger than three times a boundary layer thickness (Chen et al., 2021). Compared with the length scales in vertical and streamwise directions, the span-wise length scale λ_2 is rather stable and is roughly 100 in wall unit. (Chien and Wan, 1999; Davidson, 2015; Dennis, 2015; Robinson, 1991).

Another essential property of coherent structures is that they are time-persistent. Smith and Metzler (1983) examined the low-speed velocity streaks in the near-wall region using high-speed video and found the persistent property. They observed that the low-speed streaks maintain their integrity and reinforce for longer than the bursting time.

doi:10.6342/NTU202300192

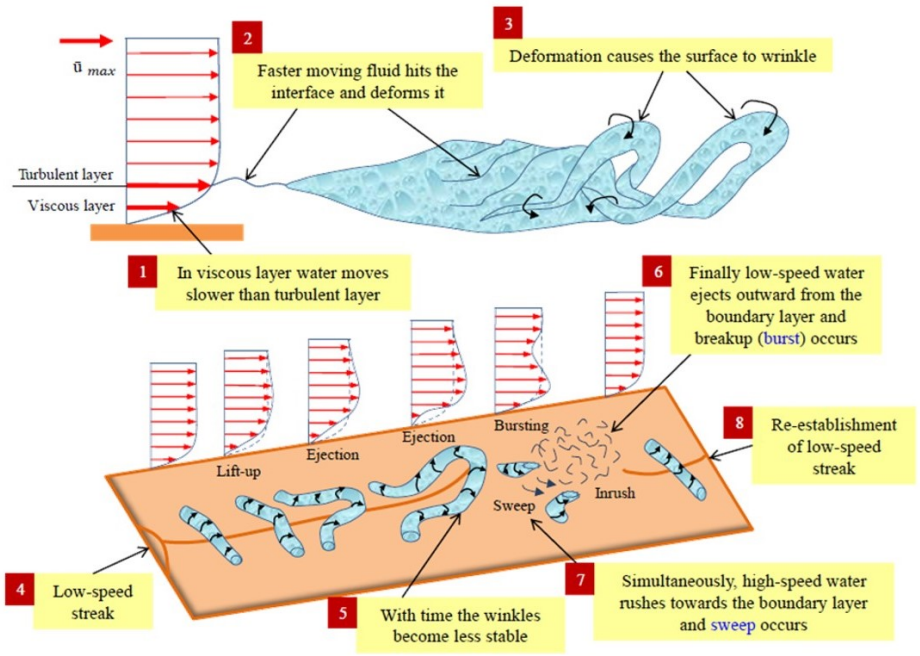

Figure 2.4: Sketch of bursting phenomenon proposed by Salim et al. (2017)

The bursting time t_b is defined as the duration of a bursting process, from the generation of low-speed hairpin streak ejects until the structure collapses. Dimensionless bursting time $t_b^+ = t_b \frac{u_*^2}{\nu}$ ranges from 480 (Smith and Metzler, 1983) to 2000 (Nakagawa and Nezu, 1981).

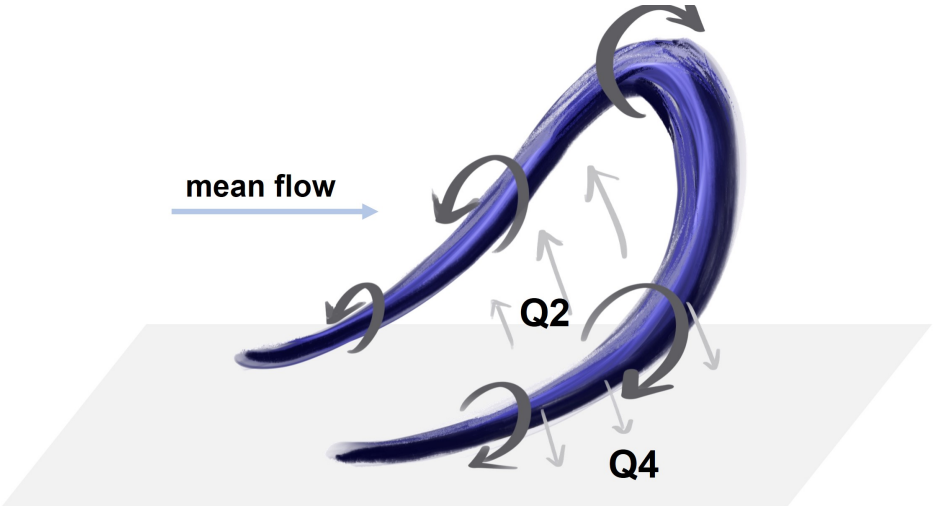

Figure 2.5: Schematic image of a hairpin eddy. Q2 represents the ejection ($u' < 0,\ w' > 0$) and Q4 represents the sweep ($u' > 0,\ w' < 0$). The left part is the legs of a hairpin vortex. On the right side, in the middle of the Ω shape, is the head of a vortex. The inclined angle of a vortex varies from 5 to 45 ° to the boundary (Chien and Wan, 1999; Dennis, 2015).

doi:10.6342/NTU202300192

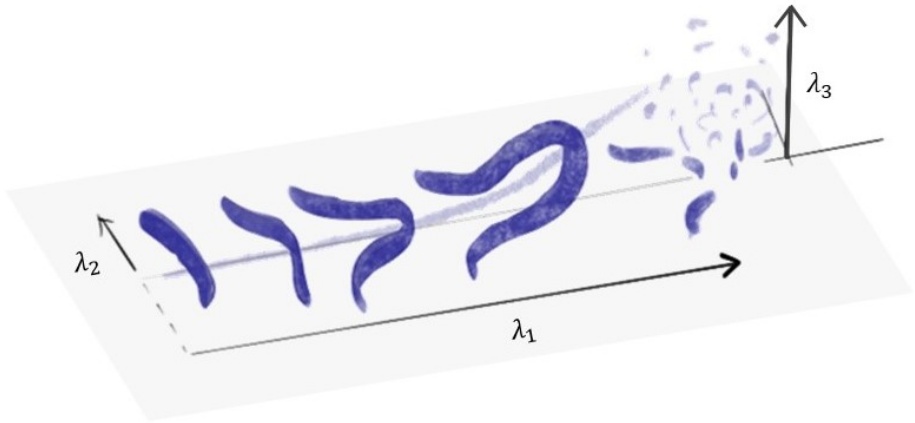

Figure 2.6: A bursting process with length scales in streamwise direction λ_1, spanwise direction λ_2, and wall normal vertical direction λ_3.

2.2.2 Quadrant analysis

To quantitatively analyze the turbulent coherent structures, i.e., sweeps and ejections, the quadrant analysis is applied by plotting the streamwise and vertical velocity fluctuations on $u' - w'$ planes (Lu and Willmarth, 1973). The velocity fluctuations are decomposed by Reynolds decomposition. Recently, an extending quadrant analysis into three-dimension known as Octant analysis has been used to analyze three-dimensional turbulent structures near the boundary (Keylock et al., 2014; Ölçmen et al., 2006; Volino and Simon, 1994). However, due to the simplicity and the capability of revealing turbulent physic properties, the two-dimensional quadrant approach is chosen for this study. For two-dimensional quadrant analysis, the four quadrants are labeled Q1 to Q4 as shown in Fig.2.7. Q1 with ($u' > 0$, $w' > 0$) is the outward interactions; on the other hand, Q3 with ($u' < 0$, $w' < 0$) represents the inward events. The second quadrant Q2 with ($u' < 0$, $w' > 0$) represents ejections, while the fourth quadrant Q4 with ($u' > 0$, $w' < 0$) represents sweeps. Quadrant analysis gives a way to distinguish downward high-speed sweep and upward low-speed ejection events. By quadrant analysis, researchers found that the shape of velocity fluctuations on the quadrant near the boundary is not symmetric.

doi:10.6342/NTU202300192

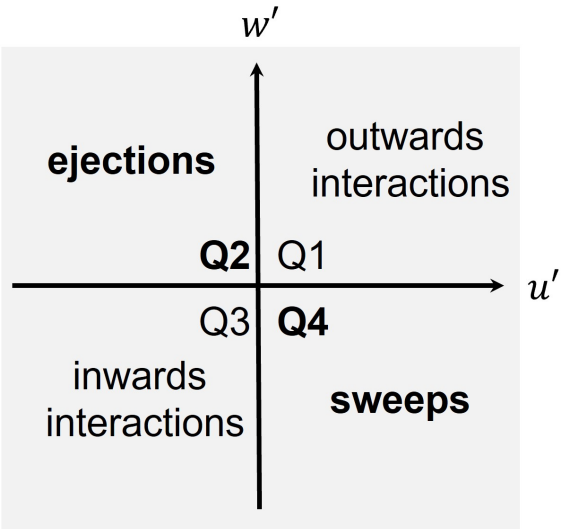

Figure 2.7: Quadrant analysis of coherent structures. Velocity fluctuations are obtained based on Reynolds decomposition of flow velocity.

This phenomenon implies that near the boundary, turbulence are not isotropic (Cellino and Lemmin, 2004; Dennis, 2015; Muste et al., 2009; Nezu, 1993; Robinson, 1991; Smith C, 1996). Since the elliptical shape indicates that the turbulent velocity fluctuations are anisotropic, adding a random velocity fluctuation term such as the Wiener process to the time-averaged flow velocity in the Langevin equation (Eq. 2.24) is not an adequate way to simulate the influence of turbulence near the boundary.

doi:10.6342/NTU202300192

2.3 Lagrangian Particle tracking models

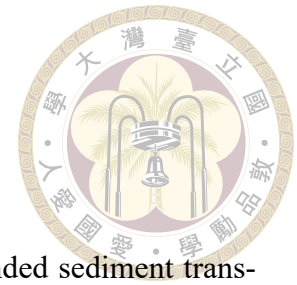

This section introduces a classical Lagrangian PTM for suspended sediment transport in a fully-developed open-channel flow. A PTM is a random-walk-based model for non-cohesive sediment particles. The governing equation is based on the integration of a Langevin equation which is one of the stochastic differential equations (SDE). A SDE is a differential equation with at least one term a stochastic process. The following Langevin equation describes the velocity change per unit mass due to forces applied on a particle (Gardiner and others, 1985),

$$d\boldsymbol{X}(t) = \boldsymbol{\mu}(\boldsymbol{X}(t), t) + \boldsymbol{\sigma_r}(\boldsymbol{X}(t), t)\boldsymbol{\xi}(t)\,, \tag{2.24}$$

where $\boldsymbol{X}(t)$ denotes the particle position vector consisting of particle location in stream-wise and vertical positions, $\boldsymbol{X}(t) = \{X(t), Z(t)\}$. $\boldsymbol{\mu}(\boldsymbol{X}(t), t)$ represents the velocity resulting from deterministic force and the second term at right-hand side of the equation, $\boldsymbol{\sigma_r}(\boldsymbol{X}(t), t)\boldsymbol{\xi}(t)$, denotes fluctuated velocity caused by the random force. For suspended sediment transport in open-channel flows, the deterministic force is from the mean drift flow motion that carries the sediment particles, and gravity force that pulls particles down. The $\boldsymbol{\xi}(t)$ is an arbitrary two-dimensional stochastic process composed of random values that can be interpreted as the random and chaotic nature of turbulence. $\boldsymbol{\sigma_r}(\boldsymbol{X}(t), t)$ is a known term that characterizes the random turbulent forces. The time evolution of the PDF of an individual particle velocity in Eq. 2.24 can be described by a Fokker-Plank equation. By interpreting a two-dimensional advection diffusion equation (ADE) without sources and sinks as a Fokker-Plank equation, a stochastic diffusion particle tracking model (SD-PTM) is derived (Argall et al., 2004; Borgas and Sawford, 1994; Dimou and

doi:10.6342/NTU202300192

Adams, 1993; Heemink, 1990; Man and Tsai, 2007; Risken, 1989).

2.3.1 Stochastic diffusion particle tracking model (SD-PTM)

The SD-PTM is a Lagrangian model that is used to describe irregular suspended particle trajectories. Since $\boldsymbol{\xi}(t)$ aims to interpret the random and chaotic nature of turbulence, the mathematical description of Brownian motion, the Wiener process $\{\boldsymbol{W}(t),\ t \geq 0\}$ is commonly utilized. The mathematical properties of the Wiener process is provided in Appendix B.2. Integrating Eq. 2.24 by Ito's stochastic integral, the integration form of the Langevin equation becomes,

$$\boldsymbol{X}(t) = \boldsymbol{X}(0) + \int_0^t \boldsymbol{\mu}(\boldsymbol{X}(s), s)ds + \int_0^t \boldsymbol{\sigma_r}(\boldsymbol{X}(s), s)d\boldsymbol{W}(s) \quad t \in [0, T]\,. \tag{2.25}$$

In order to apply the SDE (Eq. 2.25) to suspended sediment transport, a two-dimensional ADE is utilized to determine the forms of $\boldsymbol{\mu}(\boldsymbol{X}(s), s)$ and $\boldsymbol{\sigma_r}(\boldsymbol{X}(s), s)$. Let's consider the general form of two-dimensional ADE i.e., a two-dimensional mass transport model,

$$\frac{\partial c}{\partial t} + \frac{\partial \bar{u}c}{\partial x} + \frac{\partial \bar{w}c}{\partial z} = \frac{\partial}{\partial x}\left(D_{xx}\frac{\partial c}{\partial x} + D_{xz}\frac{\partial c}{\partial z}\right) + \frac{\partial}{\partial z}\left(D_{zx}\frac{\partial c}{\partial x} + D_{zz}\frac{\partial c}{\partial z}\right). \tag{2.26}$$

Eq.2.26 describe the transport of a conservative substance with no sources and sinks, where c denotes the particle concentration, $\bar{u}, \bar{w}$ are the flow velocity in x and z directions, and $D_{xx}, D_{xz}, D_{zx}, D_{zz}$ are diffusion coefficients. One can rearrange Eq. 2.26, [1]

$$\begin{aligned}\frac{\partial c}{\partial t} + \frac{\partial}{\partial x}\left(\bar{u}c + c\frac{\partial D_{xx}}{\partial x} + c\frac{\partial D_{xz}}{\partial z}\right) + \frac{\partial}{\partial z}\left(\bar{w}c + c\frac{\partial D_{zx}}{\partial x} + c\frac{\partial D_{zz}}{\partial x}\right) \\ = \frac{\partial}{\partial x}\left(\frac{\partial cD_{xx}}{\partial x} + \frac{\partial cD_{xz}}{\partial z}\right) + \frac{\partial}{\partial z}\left(\frac{\partial cD_{zx}}{\partial x} + \frac{\partial cD_{zz}}{\partial z}\right).\end{aligned} \tag{2.27}$$

[1] Let $D_{xx}(\partial c/\partial x) = \partial(cD_{xx})/\partial x - c(\partial D_{xx}/\partial x)$ and same for the rest diffusion coefficients.

doi:10.6342/NTU202300192

Then consider the conditional probability of particle position in Eq. 2.25, $p(\boldsymbol{X}(t), t|\boldsymbol{X}(t_0), t_0)$, which describes the probability of particle arriving $\boldsymbol{X}(t)$ at time t given that at time t_0, initial position of the particle is $\boldsymbol{X}(t_0)$. The conditional probability density function of particle position is the following Fokker-Plank equation [2],

$$\frac{\partial p}{\partial t} + \frac{\partial}{\partial x_i}(\mu_i p) = \frac{\partial}{\partial x_i x_j}\left(\frac{1}{2}\sigma_{ik}\sigma_{jk}\, p\right) . \tag{2.28}$$

The form of $\boldsymbol{\mu}(\boldsymbol{X}(s), s)$ and $\boldsymbol{\sigma_r}(\boldsymbol{X}(s), s)$ in Eq. 2.25 can be determined by comparing the rearranged ADE (Eq. 2.27) to the Fokker-Plank equation (Eq. 2.28). Eq. 2.27 and Eq. 2.28 are equivalent when the concentration is interpreted as the probability. Then the forms of mean drift and diffusion can be obtained (Argall et al., 2004; Dimou and Adams, 1993; Heemink, 1990; Man and Tsai, 2007),

$$\mu_i = \begin{bmatrix} \bar{u} + \frac{\partial D_{xx}}{\partial x} + \frac{\partial D_{xz}}{\partial z} \\ \bar{w} + \frac{\partial D_{zx}}{\partial x} + \frac{\partial D_{zz}}{\partial x} \end{bmatrix} , \tag{2.29}$$

$$\frac{1}{2}\sigma_{ik}\sigma_{jk} = \begin{bmatrix} D_{xx} & D_{xz} \\ D_{zx} & D_{zz} \end{bmatrix} . \tag{2.30}$$

When the coordinate system is aligned with the principal axes, the off-diagonal elements in Eq. 2.30 are zero , $D_{xz} = D_{zx} = 0$.

By matching the ADE (Eq. 2.26) with the conditional PDF of particle position (Eq. e PTM is consistent with the ADE. In the following thesis, particle diffusion coefficients are used to present the diffusion coefficients in ADE, i.e., $\varepsilon_x = D_{xx}$ & $\varepsilon_z = D_{zz}$. In particle tracking models, local time-average flow velocity from the hydrodynamic model (e.g., the flow profile in the previous section) can be set as the input of the particle velocity,

[2] Herein, tensor form of the fluctuation coefficient $\boldsymbol{\sigma_r}$ is denoted as σ_{ij}.

doi:10.6342/NTU202300192

assuming the particle is fine enough. Otherwise, the velocity lag between a particle and the local flow field, i.e., the particle relaxation time, should be included.

Applying the Euler-Maruyama scheme[3] to Eq. 2.25, one can obtain the iterative equations of the Lagrangian SD-PTM in streamwise x and vertical z directions,

$$\begin{aligned} X_{n+1} &= X_n + \left(\bar{u_p} + \frac{\partial \varepsilon_x}{\partial x}\right)\Delta t + \sqrt{2\varepsilon_x}\Delta W_n \,, \\ Z_{n+1} &= Z_n + \left(\bar{w_p} - w_s + \frac{\partial \varepsilon_z}{\partial z}\right)\Delta t + \sqrt{2\varepsilon_z}\Delta W_n \,, \end{aligned} \tag{2.31}$$

where $\bar{u_p}, \bar{w_p}$ and $\varepsilon_x, \varepsilon_z$ are the mean particle velocities and sediment particles diffusions in streamwise and vertical directions [4]. Again, if a suspended particle is sufficiently fine, the particle velocity and particle diffusion can be approximated by the mean flow velocity and turbulent diffusion. w_s is sediment particle's settling velocity. The SD-PTM simulates the probabilistic trajectories of suspended sediment particles. The coefficient in deterministic term, $\boldsymbol{\mu}(\boldsymbol{X}(s), s)$ includes the mean drift flow velocity, spatial of derivative sediment diffusivity, and the settling velocity due to gravity force in the vertical direction. The random term in SD-PTM utilizes the Wiener process to describe diffusion-like fluctuations of suspended sediment movements.

In mathematics, a one-dimensional Wiener process is a centered Gaussian process whose mean is zero and has the covariance function, [5] $\mathrm{Cov}(W(s), W(t)) = \mathbb{E}[W(s)W(t)] = \min(s, t)$. The most well-known property of the Wiener process is its stationary and independent increments. Independent increments imply the process has a Markovian property, i.e., *memorylessness* [6]. According to Einstein (1950), the independent increments of a sediment particle's locations are the results of stochastic motions induced by numer-

[3] See appendix D.2.1
[4] $\bar{u_p}, \bar{w_p}$ and $\varepsilon_x, \varepsilon_z$ are not constants
[5] The symbol "$\mathbb{E}$" denotes the expected value of a random variable.
[6] See appendix A.1

doi:10.6342/NTU202300192

ous collisions with fluid particles. In such case, the increments are normally distributed,[7] meaning that $\Delta W_s = W(t+s) - W(t) \sim \mathcal{N}(0, s)$. The underlying assumption of applying the Wiener process is that the velocity fluctuations of particle movements caused by turbulence are isotropic. Without any tendency in orientation, it implies the spread of particles follows the Fick's law manifesting as a normal distribution, which is known as the Fickian diffusion or normal diffusion. The SD-PTM is suitable for simulating suspended sediment transport in a high turbulent kinetic energy environment Therefore, the diffusion of particle movements is normally distributed.

[7] $\mathcal{N}(0,\ t-s)$ denote a multivariate Gaussian distribution with a zero mean and a covariance, $t-s$.

doi:10.6342/NTU202300192

2.3.2 Analysis of particle diffusive behaviors

Any diffusion that deviates from normal diffusion is defined as anomalous diffusion. In the study, a typical method to define the anomaly of particle diffusion is the deviation of the mean squared particle displacement $\langle r \rangle$,

$$\langle r(\Delta t)^2 \rangle = \langle (r - \langle r \rangle)^2 \rangle \propto t^{\gamma}, \tag{2.32}$$

where $r(\Delta t) = X(t + \Delta t) - X(t)$ is the displacement in x of a particle moving from time t to $t + \Delta t$. The exponent γ represents the scaling diffusion exponent. For a normal or the Fickian diffusion, the ensemble variances increase linearly with time and $\gamma = 1$. The anomalous diffusion with exponent $\gamma \neq 1$ can be categorized as *super-diffusion* if $\gamma > 1$, or *sub-diffusion* if $1 > \gamma > 0$.

In sediment transport, there are similarities and differences among diffusive behaviors of bedload particles and suspended particles. Similarities reside in that the concept of diffusion is problematically based and different diffusion types rely heavily on observing time frame size (Ancey and Pascal, 2020; Furbish et al., 2017; Metzler and Klafter, 2004; Nikora et al., 2002; Pierce and Hassan, 2020; Pusey, 2011). Particle diffusion may be transient from anomalous to normal depending on different sizes of the time frame when observing individual particles' random movements. On the other hand, dissimilarities reside in different underlying assumptions of transport mechanisms that drive sediment particles. Bedload particles transport along the bottom by rolling, sliding, or bouncing/jumping. The non-Gaussian fluctuations of bedload tracers' paths or transport rates mainly caused by particle activities, such as collisions among bedload particles and channel bottom causing non-local jumps, or long random waiting time due to morphology (Ancey

doi:10.6342/NTU202300192

and Pascal, 2020; Furbish et al., 2017; Martin et al., 2012; Nikora et al., 2002).

Unlike heavier bedload particles or floating wash loads, in this study, suspended sediment particles are settleable solids that are fine enough to be carried by turbulence and heavy enough to settle on the bottom. Therefore, some overlapping behaviors can be found between bedload tracers and suspended sediment particles near the bottom. However, suspended sediment particles focus more on turbulent-particle interactions than particle-particle interactions in bedload transport. Anomalous diffusive behaviors of suspended sediment particles often stem from the anisotropic properties of carrying flows (Argall et al., 2004; Hurst, 1957; Man and Tsai, 2007; Mathieu et al., 2021; Muste et al., 2005, 2009; Salim et al., 2017; Thomson, 1987; Tsai et al., 2021, 2020). In the study, we assume that the existence of coherent structures near the boundary causes the non-Gaussian diffusive behaviors of suspended sediment particles.

doi:10.6342/NTU202300192

doi:10.6342/NTU202300192

Chapter 3

Fractional stochastic diffusion particle tracking model (FSD-PTM)

3.1 Anomaly in suspended sediment transport

The SD-PTM introduced in the last chapter 2.3 is appropriate to describe probabilistic suspended particle trajectories in fully-developed turbulent flows where the driven turbulent forces are random. The independent increments of the Wiener process are suitable to address the isotropic fluctuations of suspended particle movements resulting from surrounding fully developed turbulence.

However, it is now clear that in open-channel turbulence, the bursting process is a sequence of coherent structures often observed in the vicinity of the boundary. The bursting process, therefore, could be the primary fluid-dynamic mechanism for sediment suspension, especially in low sediment concentration flows (Jackson, 1976). Flume experiments in Kaftori et al. (1995a,b) suggest coherent structures significantly affect particles' behavior near the boundary around 30 wall units ($z^+ \approx 30$). In their experiments, particle

doi:10.6342/NTU202300192

streaks were observed and brought out by ejections, while the downward turbulence fluctuations brought particles toward the wall causing particle deposition. Similar phenomena were observed by Ninto and Garcia (1996). They pointed out that the interaction between sediment and coherent flow turbulence shows that the ejections would induce the entrainment and lift up particles away from the bed. Cellino and Lemmin (2004) pointed out that near the wall region where turbulence is generated and dissipated, ejections not only pick up the suspended particles but also carry and maintain the suspension of particles, thus playing an essential role in erosion.

Experiments proposed by Muste et al. (2005, 2009) provide more insights into the influence of suspended particles' motion on open-channel turbulence. The experiments used two particle densities (specific density of 2.65 & 1.05 with diameter 0.23 mm) in dilute concentrations. Since particles would extract energy from the flow, experimental results show that the existence of particles reduces the bulk flow velocity irrespective of particle density. Noguchi and Nezu (2009) pointed out that sediment transport is more active with stronger ejections. Their experimental results show that stronger ejection events increase the local particle concentrations while stronger sweep events decrease them.

Moreover, suspended sediment particles' velocity is higher than the mean flow velocity in the inner flow region due to the effect of coherent structures. Salim et al. (2017) conducted flume experiments in fluvial conditions to highlight the importance of instantaneous turbulent events on sediment resuspension. They applied the two-dimensional quadrant analysis and identified that the bursting event induces sediment resuspension despite the shear stress being smaller than the mean critical threshold for sediment particles. The anisotropic particle velocity fluctuations indicated that sediment flux is dominated by ejection and sweep events which was confirmed by wavelet analysis.

doi:10.6342/NTU202300192

The above flume experiments proved and evidence that the existence of coherent structures affects sediment particle's motions (Agrawal et al., 2020; Bagherimiyab and Lemmin, 2018; Cellino and Lemmin, 2004; Dey, 2014; Muste et al., 2009; Robinson, 1991; Tsai and Huang, 2019; Tsai et al., 2021). Hence, when a suspended sediment particle settles, it may be engulfed in coherent turbulent structures near the boundary. These time-persistent coherent structures can carry suspended sediment particles for some time and cause anomalous particle diffusion manifested as anisotropic fluctuations. This means that sediments' movements are not random but have a tendency, which can be described mathematically as correlated movements. In this research, we use fractional Brownian motion (FBM) to replace the Wiener process in the PTM (Eq. 2.25) in order to describe the anisotropic particle fluctuations caused by these persistent structures.

A standard FBM or fractional Brownian process denoted as $\{B^H(t),\, t \geq 0\}$ is a self-similar centered Gaussian stochastic process. In an FBM, H denotes the Hurst parameter. The value of the Hurst parameter determines the correlation of increments in an FBM and is called the Hurst value in this thesis. When $H = 0.5$, the process becomes the Wiener process, and the increments are correlated for $H > 0.5$. The larger the Hurst value, the stronger the correlation. A mathematical definition of the fractional Brownian process is provided in appendix B.3."

3.1.1 Fractional Brownian motion

Initially introduced by Mandelbrot and Van Ness (1968), a standard FBM or fractional Brownian process, $\{B^H(t),\, t \geq 0\}$, with Hurst parameter $H \in (0, 1)$ is a self-similar centered Gaussian process defined by the following covariance function,

doi:10.6342/NTU202300192

$$\text{Cov}(B^H(s), B^H(t)) = \mathbb{E}[B^H(s)B^H(t)] = \frac{1}{2}(|s|^{2H} + |t|^{2H} - |t-s|^{2H}), \quad \forall s, t \in \mathbb{R}. \tag{3.1}$$

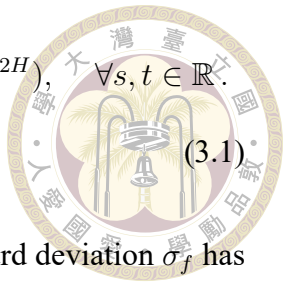

Definition 3.1.1 (fractional Brownian motion)**.** A FBM with a standard deviation σ_f has the following properties:

(1). $B^H(0) = 0$ with probability 1

(2). $\mathbb{E}[B^H(t)] = 0$ and $\mathbb{E}[(B^H(t))^2] = \sigma_f^2 t^{2H}$

(3). $\{B^H(t),\, t \geq 0\}$ is continuous but nowhere differentiable

(4). $\{B^H(t),\, t \geq 0\}$ is a self similar process

(5). $\{B^H(t),\, t \geq 0\}$ has stationary and correlated increments

Unlike the Wiener process, which has independent increments, FBM allows its disjoint increments to be correlated. To understand the dependence property of FBM, we consider the sequence of its increments. This incremental process is also known as fractional Gaussian noise (FGN) denoted as $\{Y(t),\, t \geq 0\}$. A FGN can be expressed as the difference between two consecutive values of a FBM at two different times $t+1$ and t,

$$Y(t) = B^H(t+1) - B^H(t). \tag{3.2}$$

A FGN is a stationary Gaussian process with corresponding autocorrelation,

$$\mathbb{E}[Y(t)Y(s)] = \frac{1}{2}(|t-s|^{2H} - |t|^{2H} - |s|^{2H}) \tag{3.3}$$

where H is the Hurst parameter, t and s are time points, and $\mathbb{E}[\cdot]$ denotes expectation. This expression shows that the increments of a FBM are correlated and the amount of

doi:10.6342/NTU202300192

correlation depends on the value of H. For $H = 0.5$, the FBM becomes a Wiener process with independent increments, and the autocorrelation function is equal to 0 for $t \neq s$.

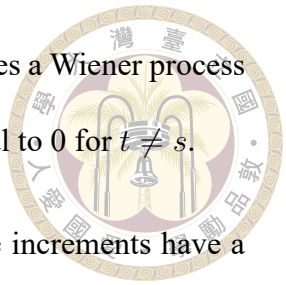

According to the autocorrelation function of FGN (Eq. 3.3), the increments have a power law decay when $H \neq 1/2$, With $H < 1/2$, the increments are negatively correlated and it is called anti-persistent. Conversely, when $H > 1/2$ the increments are positively correlated, and the process is known as the persistent process. The autocorrelation of a FGN is zero when $H = 1/2$, indicating increments are independent. Thus the collection of the incremental process corresponds to the ordinary Brownian motion.

3.1.2 Memory in correlated increments

In this study, in comparison to the memoryless property[1] with the independent increments , the term *memory* indicates the correlated increments of particles' movements. Specifically, in this research, *memory* shares the same definition of long-range dependence or long-range persistency.

Definition 3.1.2 (long-range dependence)**.** If the auto-correlation function of a stochastic process, $\rho(n) := \mathrm{Cov}(X(k), X(k+n))$, decays slowly as n tends to infinity, then the sequence, $\{X(t),\, t \in \mathbb{R}\}$, is said to exhibits long-range dependence (Biagini et al., 2008; Pipiras and Taqqu, 2017).

$$\lim_{n\to\infty} \frac{\rho(n)}{c_1 n^{-\alpha}} = 1\,, \tag{3.4}$$

where $c_1 \in \mathbb{R}$ and $\alpha \in (0, 1)$ are constants.

For an FBM, the auto-correlation function (Eq. 3.3) can be used to check if the increments have long-range dependence. When $n \to \infty$, $\rho(Y(k), Y(k+n)) \approx H(2H -$

[1] See Appendix A.1.

doi:10.6342/NTU202300192

$1)n^{2H-2}$. Then set $c_1 = H(2H-1)$ and $\alpha = 2-2H$, Eq. 3.4 would approach 1 when $H \in \left(\frac{1}{2}, 1\right)$. According to definition of long-range dependence (Eq. 3.4), FBM has long-range persistency on its increments with $H > 1/2$.

doi:10.6342/NTU202300192

3.2 Conceptual model of the research

If I have seen further it is by standing on the shoulders of giants.

Issac Newton

From a Lagrangian point of view, Muste et al. (2009) proposed a conceptualization of the water interaction with particles. Using PIV for water and PTV for particle observations, they proposed three particle phases. For the inner flow regions where $z/h < 0.2$, phase 1 describes a particle taking off from the bottom due to ejections with $u' < 0,\ w' > 0$. Then for phase 2, a particle moves with local flow structures. Phase 3 is when a particle approaches the bed following a fluid sweep with $u' > 0,\ w' < 0$.

Standing on the model proposed by Muste et al. (2009), this study proposes a more detailed conceptual model sketched in Fig. 3.1, where h is the average water height, ν is the fluid kinematic viscosity, and u_* denotes the shear velocity. The vertical direction is divided into classical two layers: the inner layer ($z/h < 0.2$) and the outer layer ($z/h \geq 0.2$). As shown in Fig. 3.1, when a particle settles down to the inner layer, its movements might or might not be affected by the coherent structures. When a particle encounters coherent structures, its movements are positively correlated with a Hurst value greater than 0.5 for a random period. On the other hand, if a particle doesn't experience any event, the Hurst value is 0.5, such that the FBM becomes the Wiener process with independent increments. Then the behaviors of a particle are totally random subjected to the isotropic turbulence.

doi:10.6342/NTU202300192

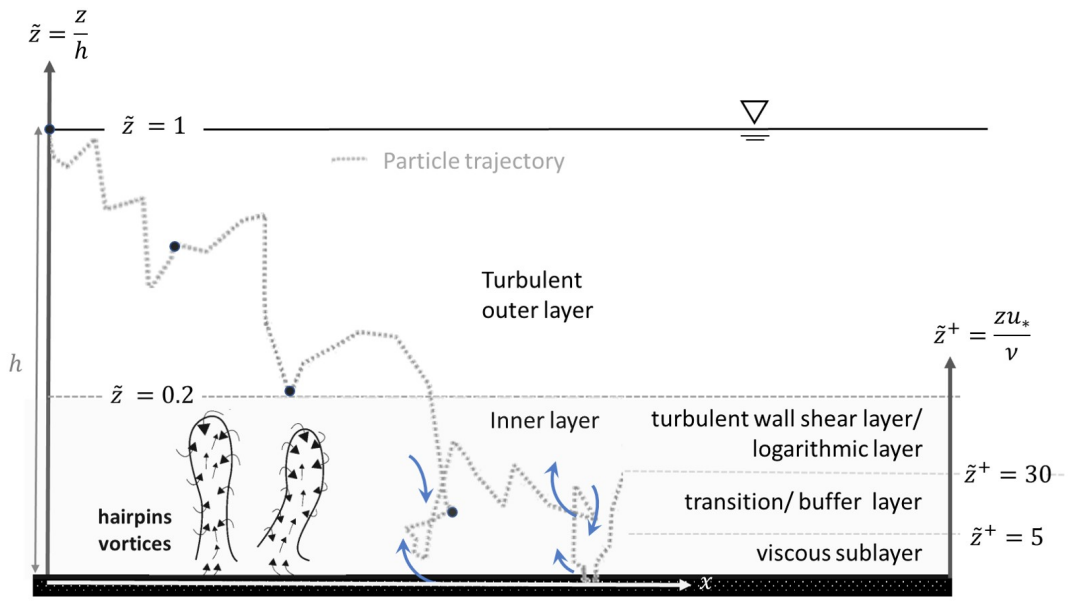

Figure 3.1: Conceptual sketch of research hypothesis.

3.2.1 Boundary conditions

The boundaries of a two-dimensional open channel flow are the water surface and the channel bed. In this study, it is assumed that the water surface remains constant during fully-developed turbulence. As for the bottom, the roughness height has been determined to be equal to two particle diameters, as suggested by Wu and Lin (2002). The reference height is defined based on the shear Reynolds number, which is presented in Table 2.2.

For a particle tracking model, interactions between individual particles and the boundaries are crucial. Deposition of particles occurs when the particle's vertical location is equal to or lower than the reference height. Fig. 3.1 shows that sweeps with $w' < 0$ may cause deposition. In the study, resuspension of particles is a random process that depends on the balance between the lift force from the flow and the particle's weight due to gravity. Modern studies of turbulence in wall-bounded sediment-laden flows have adopted a probabilistic perspective to analyze the initiation of sediment motion. Whether a particle is

doi:10.6342/NTU202300192

picked up by near-bed flow velocity fluctuations caused by turbulence is random. Several models for pick-up probability as a function of bed shear stress or near-bed velocity fluctuations have been proposed and tested based on experimental evidence, including Bose and Dey (2010, 2013); Cheng and Chiew (1998); Chien and Wan (1999); Einstein (1950); Einstein and El-Samni (1949); Elhakeem et al. (2017); Subhasish et al. (2020); Wu and Chou (2003); Wu and Lin (2002).

Specifically, Bose and Dey (2013) proposed a probability model to determine resuspension of suspended sediment particles. Resuspension is triggered when the vertical local fluid velocity fluctuation, w', exceeds the particle settling velocity, w_s. This occurs due to the near-bed bursting process, and the simulation defines resuspension to take place if $w' > w_s$.

doi:10.6342/NTU202300192

3.3 Fractional stochastic diffusion particle tracking model (FSD-PTM)

In order to model the random suspended particle trajectories with memories in the long time-persistent flows, the FBM is introduced to replace the Wiener process in the Langevin equation.There are four reasons for choosing FBM as the fractional stochastic process. First of all, FBM belongs to one kind of Gaussian process; thus, the mean of FBM is zero. Accordingly, applying FBM as the stochastic process $\boldsymbol{\xi}(t)$ in the Langevin equation (Eq. 2.24) can fulfill the fundamental assumption of turbulence that the time-averaged velocity fluctuations is zero. The second reason is for the most distinguished property of a FBM, the *correlated increments* which are often applied for addressing anomalous dynamical properties, such as long-range temporal or spatial correlations (Biagini et al., 2008; Metzler and Klafter, 2004). Moreover, FBM carries a time- or space-dependent coefficient, the Hurst parameter H. The value of the Hurst parameter can determine how correlated the increments are. The correlated increments are expected to model the dependent movements as suspended particles encounter coherent structures. The last and most important reason is that the FBM has the ability to become the Wiener process. In this way, when suspended particles transport in the outer layer or not in a coherent turbulent event near the boundary, velocity fluctuations simulated by a FBM will remain isotropic.

A detailed introduction of FBM is provided in appendix B.3. The following points summarize the advantage of applying the FBM as the fluctuation process in the Langevin equation.

(1). $\mathbb{E}[B^H(t)] = 0$: fulfill the fundamental assumption of turbulence that the time-averaged velocity fluctuations is zero.

doi:10.6342/NTU202300192

(2). $\{B^H(t),\, t \geq 0\}$ is a self similar process: which is also another prominent property of turbulence

(3). $\{B^H(t),\, t \geq 0\}$ is continuous but nowhere differentiable : the same properties of the Wiener process interpreted as fluctuations

(4). FBM has the ability to become the Wiener process when $H = 1/2$. The dependence is captured by the Hurst parameter in a FBM.

(5). $\{B^H(t),\, t \geq 0\}$ has stationary and correlated increments when $1 > H > 0.5$

3.3.1 Governing equation of the FSD-PTM

The study proposed a fraction SD-PTM whose governing equation is a SDE driven by the FBM,

$$\boldsymbol{X}(t) = \boldsymbol{X}(t_0) + \int_{t_0}^{t} \tilde{\boldsymbol{\mu}}(\boldsymbol{X}(s), s)ds + \int_{t_0}^{t} \tilde{\boldsymbol{\sigma}}_{\boldsymbol{r}}(\boldsymbol{X}(s), s) \circ d\boldsymbol{B}^H(s), \quad t \in [0, T]\,, \tag{3.5}$$

where $\boldsymbol{B}^H$ is the FBM with Hurst index $H \in (0, 1)$. Similar to Eq. 2.25, $\tilde{\boldsymbol{\mu}}(\boldsymbol{X}(s), s)$ and $\tilde{\boldsymbol{\sigma}}_{\boldsymbol{r}}(\boldsymbol{X}(s), s)$ are coefficients of mean drift and fluctuation terms. "$\circ$" denotes the Stratonovich integral. Compared to the Wiener process, the increments of FBM process are not independent. As a result, the quadratic variation property of Ito integral cannot be utilized. However, the Stratonovich integral can still be applied and the normal chain rule can be employed.

doi:10.6342/NTU202300192

Fractional calculus

Throughout the thesis, we consider a fixed time interval $[0, T]$ with uniform partitions. The second fluctuation term in Eq. 3.5 can apply either the Stratonovich or Riemann-Stieltjes integral. The difference between the Stratonovich integral and the Riemann-Stieltjes integral when considering the SDE driven by FBM lies in the interpretation of the rules for stochastic calculus with respect to the underlying random process.

The Stratonovich integral is a type of stochastic integral that provides a mathematical framework for the integration of a random process over a specified interval of time. In the context of a SDE driven by FBM, the Stratonovich integral can be used to model the expected value of the cumulative change in the FBM over a specified interval of time. However, a Stratonovich integral results in implicit functions.

On the other hand, the Riemann-Stieltjes integral is a type of the definite integral that provides a mathematical framework for the integration of a continuous function with respect to another continuous function under certain smoothness condition. For Eq. 3.5, the Riemann-Stieltjes integral can be used to model the cumulative change in the FBM over a specified interval of time. According to Hu et al. (2016), if $\tilde{\boldsymbol{\sigma}}_{\boldsymbol{r}}$ is continuously differentiable and $\tilde{\boldsymbol{\mu}}$ is Lipschitz [2], Eq. 3.5 has a solution that is Hölder continuous of order γ for any $0 < \gamma < H \in (1/2, 1)$. The fractional integration of the fluctuation term with respect to a FBM can then be integrated by the Riemann-Stieltjes integral that can be regarded as a "fractional integration by parts". By applying the Riemann-Stieltjes integral, an explicit expression in terms of fractional derivatives can then be obtained when

[2] Denote the space of β-Hölder continuous function on the interval $[a, b]$ as $C^{\beta}(a, b)$. If $\tilde{\boldsymbol{\mu}} \in C^{\beta_1}(a, b)$ and $\tilde{\boldsymbol{\sigma}}_{\boldsymbol{r}} \in C^{\beta_2}(a, b)$ with $\beta_1 + \beta_2 > 1$, the Riemann-Stieltjes integral exists. we refer to research proposed by Hu et al. (2016) for additional details.

doi:10.6342/NTU202300192

$H > 0.5$. The numerical approximation scheme is introduced in the following section 3.3.3.

In summary, the Stratonovich and Riemann-Stieltjes integrals differ in their interpretation of the calculus rules for the underlying random process, where the Stratonovich integral models the expected cumulative change, and the Riemann-Stieltjes integral models the actual cumulative change.

Stratonovich and Ito Integral

Stratonovich integral is defined as a limit of Riemann sums. For a time interval $[0, T]$ with uniform partitions, $0 = t_0 < t_1 < ... < t_n = T$, a Stratonovich integral of a process $\{f(X(t)),\, t \geq 0\}$ on the random process $\{\xi(t),\, t \geq 0\}$ can be defined as,

$$\int_0^T f(X(t))d\xi(t) = \lim_{n\to\infty} \sum_{i=1}^{n} f\left(\frac{(X(t_{i-1}) + X(t_i)}{2}\right)\left[\xi(t_{i-1}) - \xi(t_i)\right]. \tag{3.6}$$

Herein, in comparison with the Stratonovich integral, the Ito integral is shown as follows,

$$\int_0^T f(X(t)) \circ d\xi(t) = \lim_{n\to\infty} \sum_{i=1}^{n} f(X(t_{i-1}))\left[\xi(t_{i-1}) - \xi(t_i)\right]. \tag{3.7}$$

Pathwise Riemann-Stieltjes integral

Consider a fixed time interval $[0, T]$ and $a < b$ where $a, b \in [0, T]$. Suppose that $f \in C^{\beta_1}(a, b)$ and $g \in C^{\beta_2}(a, b)$ with $\beta_1 + \beta_2 > 1$. Let $\beta_1 > \alpha$ and $\beta_2 < 1 - \alpha$, then the Riemann-Stieltjes integral $\int_a^b f dg$ exists and can be expressed by the following equation,

$$\int_a^b f(t)dg(t) = e^{i\pi\alpha} \int_a^b D_{a^+}^{\alpha} f(t) D_{b_-}^{1-\alpha} g_{b_-}(t)dt, \tag{3.8}$$

doi:10.6342/NTU202300192

where D^{α}_{a+} and $D^{1-\alpha}_{b-}$ are the fractional Weyl derivatives defined as,

$$D^{\alpha}_{a+}f(t) = \frac{1}{\Gamma(1-\alpha)}\left(\frac{f(t)}{(t-a)^{\alpha}} + \alpha\int_a^t \frac{f(t)-f(s)}{(t-s)^{1+\alpha}}ds\right), \text{and}$$
$$D^{\alpha}_{b-}f(t) = \frac{e^{-i\pi\alpha}}{\Gamma(1-\alpha)}\left(\frac{f(t)}{(b-t)^{\alpha}} + \alpha\int_t^b \frac{f(t)-f(s)}{(s-t)^{1+\alpha}}ds\right), \tag{3.9}$$

with $a < t < b$.

doi:10.6342/NTU202300192

3.3.2 Determination of the coefficients of drift and random terms

To determine the coefficients in the governing equation, we first consider the Wiener process as the random process. Since $H = 1/2$, the FBM becomes the Wiener process, then Eq. 3.5 becomes,

$$\boldsymbol{X}(t) = \boldsymbol{X}(t_0) + \int_{t_0}^{t} \tilde{\boldsymbol{\mu}}(\boldsymbol{X}(s), s)ds + \int_{t_0}^{t} \tilde{\boldsymbol{\sigma}}_{\boldsymbol{r}}(\boldsymbol{X}(s), s) \circ d\boldsymbol{W}_s \tag{3.10}$$

If the drift and fluctuation coefficients are the same, then governing equation of the SD-PTM (Eq. 2.25) and Eq. 3.10 are the same SDE driven by the same stochastic process, the Wiener process. The only difference between Eq. 2.25 and Eq. 3.10 is the different stochastic integrals. Since Eq. 2.25 is integrated by the Ito integral, it is often called Ito SDE; on the other hand, Eq. 3.10 is integrated by the Stratonovich integral, thus it is known as the Stratonovich SDE.

Intuitively, having the same governing equation, results of the Ito SDE (Eq. 2.25) should be equivalent to results of the Stratonovich SDE (Eq. 3.10). Accordingly, we can determine the forms of $\tilde{\boldsymbol{\mu}}(\boldsymbol{X}(s), s)$ and $\tilde{\boldsymbol{\sigma}}_{\boldsymbol{r}}(\boldsymbol{X}(s), s)$ based on the forms of $\boldsymbol{\mu}(\boldsymbol{X}(s), s)$ and $\boldsymbol{\sigma}_{\boldsymbol{r}}(\boldsymbol{X}(s), s)$ in Eq. 2.25. However, The *Ito-Stratonovich dilemma*[3] points out that the very same SDE can have different solutions depending on different stochastic integrals. The dilemma resides in the integral over the no-where differentiable stochastic process in the random term of the SDE. More specifically, for a non-constant diffusion coefficient, the Ito and Stratonovich interpretation of the same SDE can lead to different results (Oksendal, 2013).

The difference between the Ito and Stratonovich interpretation lies in the location

[3] See appendix C.1.1

doi:10.6342/NTU202300192

where $\boldsymbol{\sigma_r}(\boldsymbol{X}(s), s)$ is evaluated. Ito integral evaluates the function at the left endpoint while the Stratonovich integral at the mid-point of each interval (**?**). In short, if a physical phenomenon can be described by a Ito SDE (Eq. 2.25), then the same process is equivalent to a Stratonovich SDE (Eq. 3.10) by adding a correlation term to the drift coefficient:

$$\boldsymbol{X}(t) \overset{\text{Str}}{=} \boldsymbol{X}(t_0) + \int_{t_0}^{t} \left(\boldsymbol{\mu}(\boldsymbol{X}(s), s) - \frac{1}{2} \frac{\partial \boldsymbol{\sigma}(\boldsymbol{X}(s), s)}{\partial \boldsymbol{x}} \boldsymbol{\sigma_r}(\boldsymbol{X}(s), s) \right) ds + \int_{t_0}^{t} \boldsymbol{\sigma_r}(\boldsymbol{X}(s), s) d\boldsymbol{W}_s \,. \tag{3.11}$$

That is, the integration of Ito SDE (Eq. 3.11) leads to the same results as the integration of Stratonovich SDE (Eq. 3.10) when,

$$\tilde{\boldsymbol{\mu}}(\boldsymbol{X}(s), s) = \left(\boldsymbol{\mu}(\boldsymbol{X}(s), s) - \frac{1}{2} \frac{\partial \boldsymbol{\sigma}(\boldsymbol{X}(s), s)}{\partial \boldsymbol{x}} \boldsymbol{\sigma}(\boldsymbol{X}(s), s) \right) , \quad \tilde{\boldsymbol{\sigma}}_{\boldsymbol{r}}(\boldsymbol{X}(s), s) = \boldsymbol{\sigma_r}(\boldsymbol{X}(s), s) \,. \tag{3.12}$$

The relation in Eq. 3.12 is called *Ito-Stratonovich drift correlation formula*[4].

[4] See appendix C.1.2

doi:10.6342/NTU202300192

3.3.3 Numerical scheme for FSD-PTM

In the study, Monte Carlo simulation method is applied. By generating a large number of sample paths X_t^η, sufficiently robust ensemble statistics can then be obtained. For a modeling perspective, the modified Euler scheme proposed by Hu et al. (2016) and Liu and Tindel (2019) is used for the numerical approximation of equation Eq. 3.5:

$$X_t^\eta = X_{t_k}^\eta + \tilde{\mu}(X_{t_k}^\eta, t_k)(t-t_k) + \tilde{\sigma_r}(X_{t_k}^\eta, t_k)(B_t^H - B_{t_k}^H) + \frac{1}{2}(\nabla\tilde{\sigma_r}\tilde{\sigma_r})(X_{t_k}^\eta, t_k)(t-t_k)^{2H}, \tag{3.13}$$

where X_t^η is the generic approximation of X_t starting from the initial condition $X_0^\eta = x$. The uniform partition, $0 = t_0 < t_1 < ... < t_\eta = T$, is considered on the finite time interval $[0, T]$. Specifically, let $k = 0, ..., \eta - 1$ and then $t_k = kT/\eta$. In Eq. 3.13, $t \in [t_k, t_{k+1}]$. The $\nabla\sigma_r$ is a 2×2 matrix and $(\nabla\tilde{\sigma_r}\tilde{\sigma_r}) = \Sigma_{k=1}^2(\frac{\partial\tilde{\sigma_r}}{\partial x_k})\tilde{\sigma_r}$.

The convergence of the modified Euler approximation scheme is,

$$\sup_{0\le t\le T} \langle \mid X_t - X_t^\eta \mid^p \rangle^{1/p} \le C_1\gamma_\eta^{-1} \tag{3.14}$$

where C_1 is a constant and independent of η. For any $p \ge 1$, the convergence rate γ_η depends on the Hurst value (Hu et al., 2016),

$$\gamma_\eta = \begin{cases} \eta^{-1/2}, & H = 1/2 \\ \eta^{2H-1/2}, & 1/2 < H < 3/4 \\ \frac{\eta}{\sqrt{\log\eta}}, & H = 3/4 \\ \eta, & 3/4 < H < 1. \end{cases} \tag{3.15}$$

When $H = 1/2$, the convergent rate of Eq. 3.13 is the same as the convergent rate of

doi:10.6342/NTU202300192

the Euler-Maruyama's scheme for the following Stratonovich SDE driven by the Wiener process.

Correction term for discrete FBM

The FBM/FGN is widely applied to modeling phenomena with memory, which is defined as the long-range dependence in the research. Long-range dependence is a hallmark of a process that exhibits a slow decline in its autocorrelation function. It suggests that the process has a long-term memory of its past states, which continues to influence its current behavior across multiple scales. While FBM is often defined as a continuous stochastic process, in engineering applications, applications of FBM are usually discrete in time. The discrete-time FBM is generated by a cumulative sum of a finite number of FGN. In this situation, Delignières (2015) suggests a scaling coefficient C_{dfbm} should be included to rescale the variance of discrete fractional Brownian motion with length n.

$$C_{fbm} = \frac{\text{Var}(B_n^H)}{n^{2H}} = \frac{\sigma_f^2}{(n-1)n^{2H+1}} \sum_{i=1}^{n-1} \left[(n-1)i^{2H}\right] \tag{3.16}$$

doi:10.6342/NTU202300192

Chapter 4

Fractional suspended sediment transport in open channel flows

In the section, the proposed FSD-PTM is applied to simulate suspended sediment transport in a two-dimensional open channel flow in the streamwise and vertical directions. The particle properties and flow conditions utilized the suspended sediment transport experiments provided by Muste et al. (2005). The experimental results including particle velocity and concentration profiles then are used for model validation.

The proposed FSD-PTM can visualize the possible transport paths of suspended sediment particles. Fig. 4.1 illustrates one sample path in x and z directions as demonstration. In the z direction, the gray dash line marks out the boundary of inner layer ($z/h = 0.2$). At turbulent outer layer ($z/h > 0.2$), the particle' s movements are affected by the flow and fluctuates randomly with $H = 0.5$. As the particle transport and settles to the lower inner layer, its movements might be affected by the hairpin vortices including ejections (Q2, $u' < 0,\ w' > 0$) and sweeps (Q4, $u' > 0,\ w' < 0$). If the particle encounters events, the increments are correlated and simulated by an FBM with $H > 0.5$ until the

doi:10.6342/NTU202300192

affected duration is over. Inside the inner layer, the demonstrated trajectories affected by the ejections are colored in red while sweeps in blue. In the demonstration, it shows that the resuspension of a particle is a result of ejections. On the other hand, not all the depositions are caused by the sweeps because a sediment particle can simply settle to the bed by gravity. The intermittent movements of particles near the boundary can be observed in Fig. 4.1.

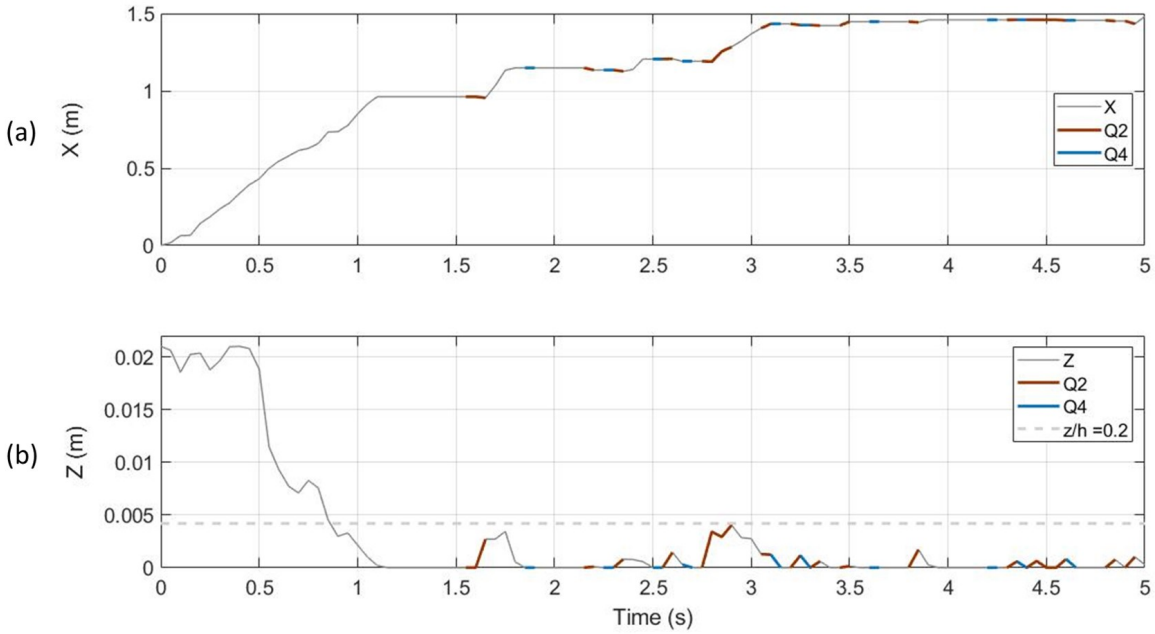

Figure 4.1: One sample path of sediment particle positions along with simulation time in (a) streamwise and (b) vertical directions. The trajectories affected by the ejections (Q2) are colored in red while sweeps (Q4) in blue. The gray dash line marks out the boundary of the inner layer in (b).

doi:10.6342/NTU202300192

4.1 Application to suspended sediment transport in fully-developed open-channel flows

To apply the proposed FSD-PTM to suspended sediment particle transport in a fully-developed turbulent flow, we first specify the initial conditions and boundary conditions. For the initial conditions, as shown in demonstration (Fig. 4.1), each particle is released at the water surface in the vertical direction and at origin in stremawise direction, i.e., $(X_0, Z_0) = (0,\ h)$. As mentioned in the conceptual model (Fig. 3.1), the simulation applies the classical two-layer approach in open channel flow: the inner layer ($z/h < 0.2$) and the outer layer ($z/h \geq 0.2$). If a particle settles down to the inner layer, its movements might or might not be affected by the hairpin vortices consisting of coherent structures. When a particle encounters coherent structures, its movements are correlated with a Hurst value larger than 0.5 for a random period, according to a PDF proposed by Agrawal et al. (2020). On the other hand, if a particle does not experience any event, the Hurst value is 0.5, such that the FBM becomes the Wiener process with independent increments. Then the behaviors of a particle are totally random due to isotropic turbulence.

For boundary conditions, deposition and resuspension of a particle are determined by following conditions. In the simulation, sweep events with $w' < 0$ might cause deposition. Deposition of a particle is defined when the vertical location of the particle is equal to or smaller than the reference height. The resuspension of a particle is determined when a vertical velocity fluctuation is larger than the particle settling velocity, i.e., $w' > w_s$ (Bose and Dey, 2013).

The followings introduce other variables, such as particle properties, particle velocity calculating based on hydrodynamic flow velocity with velocity lags, sediment particles'

doi:10.6342/NTU202300192

diffusion, and the occurrences of coherent structures.

4.1.1 Flow conditions and sediment particle characteristics

In the simulation, the sediment particle properties are from the particles in flume experiments conducted by Muste et al. (2005), who used two kinds of particles to investigate the influence of different particle densities on turbulence in the open channel flow under dilute sediment concentration environments. Muste et al. (2005) emphasized that there were few particle streaks from the channel bottom caused by particle-particle interference. In the experiments, little particle streaks can ensure the observations focused only on particle-turbulence interactions. The experimental conditions are listed in Table 4.1. In the experiments, the flow depth was set to be small to ensure a large 7.5-channel aspect ratio to prevent the influence of secondary flows. In the simulations, we assume the flow depth is small enough to ignore the wake effect in the outer layer because $z^+ < 1000$. Therefore, besides the viscous sublayer, turbulent wall shear and turbulent outer layer apply the logarithmic velocity distribution shown in Eq. 2.20 and Eq. 2.22.

$$u^+ = \bar{u}/u_* = z^+, \quad z^+ < 5$$

$$u^+ = \frac{1}{\kappa} \ln \frac{z}{z_0}, \qquad z^+ \geq 5.$$

where, the z_0 is the zero-velocity level based on smooth boundary condition, $z_0 = 0.11\nu/u_*$. The streamwise flow velocity profile in the simulation calculated based on Eq. 2.20 and Eq. 2.22 is shown in Fig. 4.2.

The blue dots in Fig. 4.2 are the flow velocity measured in the particle-laden experiments (Muste et al., 2005). The small difference between the calculated flow velocity profile and the experimental measured data points are discussed. According to Muste

doi:10.6342/NTU202300192

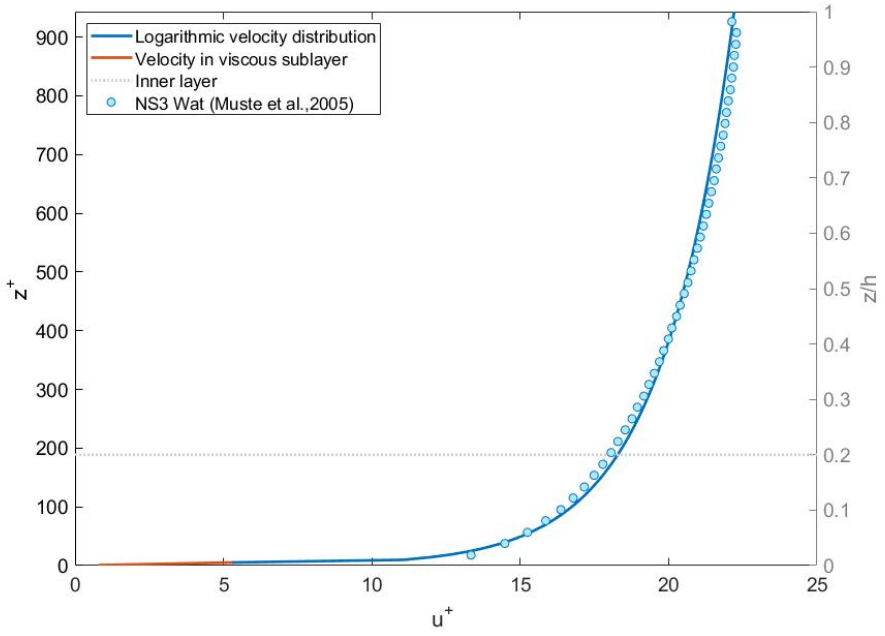

Figure 4.2: The streamwise flow velocity profile in the simulation.

et al. (2005), the slight difference between the log flow velocity and the flow velocity in the particle-laden flow experiments (NS3 Wat) is because particles enhance the bulk flow velocity in the upper flow region. While at the lower region, results seemed to attenuate the bulk flow velocity slightly but slightly increase in the vicinity of the boundary.

In the simulation, the NS particle with a specific density of 2.65 instead of 1.05 is chosen for model application. In the previous PTM research (Man and Tsai, 2007; Oh and Tsai, 2010; Tsai et al., 2018), validations of numerical simulations found that SD-PTMs were more suitable for lighter particles whose density is close to water, such as NBS particles. Simulation results of SD-PTM using NBS particles match well with the experimental particle velocity which is often similar to the flow velocity profiles in the experiments. However, besides velocity lag, the simulation results near the boundary deviate from the experimental data in concentration and particle velocity when heavier particles are simulated. Tsai et al. (2021, 2020) pointed out that the disagreement might be due to a lack of considering the correlation subject to turbulent structures, which reinforces

doi:10.6342/NTU202300192

the importance of including the influence of coherent turbulent structures in PTMs.

The experiments conducted by Muste et al. (2005) intended to see whether the existence of dilute suspended particles affects the turbulence intensity in open channel flows. Muste et al. (2005) pointed out that the averaged streamwise velocity lag between fluid and particle is 5.5% in the outer region. Therefore, the simulation's mean velocity of Lagrangian particles adopts the lag velocity in the outer layer.

Table 4.1: Flow and sediment particle characteristics in experiments (Muste et al., 2005)

Experimental Conditions (Muste et al., 2005)	**Value** (NS3)
Flow depth (m)	0.021
Bed slope	0.0113
Reynolds number	17340
Shear velocity (m/s)	0.043
von Karman coefficient	0.396
Particle specific gravity	2.65
Particle diameter (mm)	0.23
Settling velocity (m/s)	0.024
Particle volumetric concentration (%)	0.046

doi:10.6342/NTU202300192

4.1.2 Particle diffusion coefficient

The irregular movements of suspended sediment particles are highly related to the carrying turbulent flows. While the gravity force pulls sediment particles down, the turbulent momentum can provide enough energy for particles to suspend and transport among hydrodynamic layers in the vertical directions. Accordingly, sediment diffusion coefficients are often calculated based on the turbulent diffusivity, ν_t. The Schmidt number, Sc_t, is a dimensionless parameter used to describe the relationship between turbulent diffusivity and sediment diffusion, which is defined as,

$$Sc_t = \frac{\nu_t}{\varepsilon_z}, \tag{4.1}$$

and it has the expression of,

$$Sc_t = \left[\frac{St}{(1-\rho_f/\rho_p)} + \frac{1}{(1+St)}\right], \tag{4.2}$$

where ρ_p and ρ_s denote the particle density and fluid density. The St is the Stokes number. St is defined as the ratio between the particle time scale τ_p and the integral timescale of the surrounding turbulence τ_t. The value of $St = \tau_p/\tau_t$ is an index to see the degree of suspension of a particle in the turbulent flow. A smaller value implies particles transport quickly along with carrying flow with little relaxation time. The timescales τ_p and τ_t are defined as,

$$\begin{aligned} \tau_p &= \frac{w_s}{(1-\rho_f/\rho_p)g}, \\ \tau_t &= \frac{\nu_t}{C_\mu k}, \end{aligned} \tag{4.3}$$

doi:10.6342/NTU202300192

where C_μ is a constant coefficient with a value 0.09 (Absi et al., 2011). The parameter τ_t characterizes the turbulence's strength related to the turbulent kinetic energy (TKE). TKE can be calculated by a two-equation turbulence model such as the $k-\epsilon$ model. The k denotes the TKE, and ϵ is the turbulent dissipation rate. Based on the mixing length theory (Absi, 2019, 2021; Absi et al., 2011), the dimensionless $\nu_t^+ = \nu_t/\nu$ and $k^+ = k/u_\tau^2$ as a function of the friction Reynolds number Re_* and z^+ are applied to calculate the Schmidt number,

$$\begin{aligned} \nu_t^+ &= z^+ \exp\left\{-\frac{z^+ + 0.34Re_* - 11.5}{0.46Re_* - 5.98}\right\}, \\ k^+ &= \frac{1}{\sqrt{C_\mu}} \exp\left\{-\frac{z^+ - 0.3Re_* - 100}{0.58Re_* - 17}\right\}, \end{aligned} \tag{4.4}$$

for $z^+ > 30$. The equations are validated by open channel flow velocity in experiments with a smooth wall condition (Absi, 2021) with $300 < Re_* < 5200$. For $z^+ < 30$, the ν_t^+ and k^+ are

$$\begin{aligned} \nu_t^+ &= 0.3\kappa\sqrt{B_t}\,(z^+)^2 \exp\left\{-\frac{z^+}{16}\right\}\left(1 - \exp\left\{-\frac{z^+}{26}\right\}\right), \\ k^+ &= B_t (z^+)^2 \exp\left\{-\frac{z^+}{8}\right\}, \end{aligned} \tag{4.5}$$

where B_t is a coefficient defined as $B_t = 0.0164 \ln Re_* + 0.00334$. For viscous sublayer, $k^+ = (z^+)^2$. After having the Schmidt number and the turbulent diffusivity, one can obtain particle diffusion in the vertical direction based on Eq. 4.1. The particle diffusion value in the wall-normal direction is sketched in Fig. 4.3. The red line represents the particle diffusion coefficient in the region with $z^+ < 30$, while the black line represents $z^+ > 30$.

In the study, longitudinal particle diffusion is a constant that is often applied in the two-dimensional ADE (Elder, 1959; Fischer, 1966; Shin et al., 2020),

$$\varepsilon_x = 5.93 u_* h. \tag{4.6}$$

doi:10.6342/NTU202300192

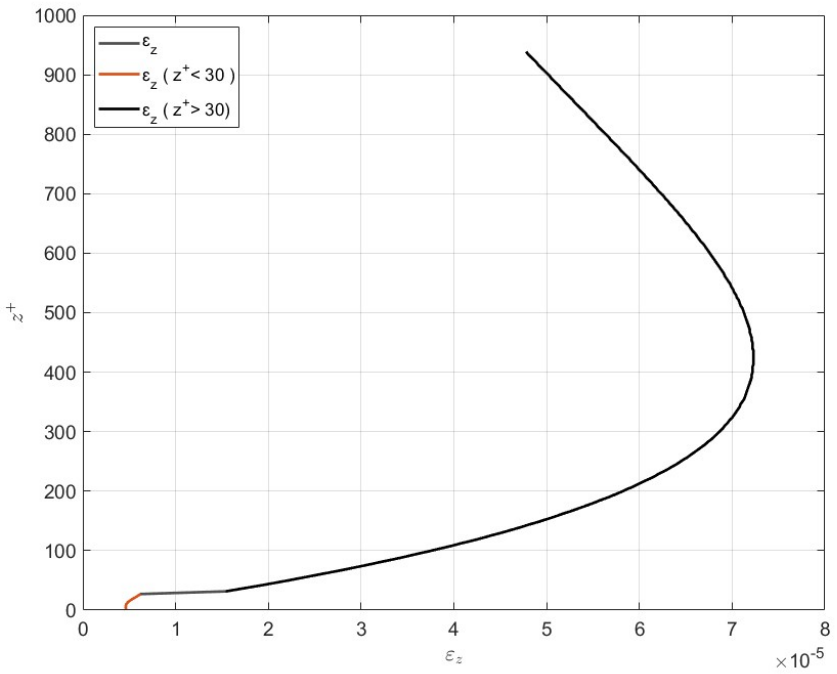

Figure 4.3: Particle diffusion in wall normal direction.

doi:10.6342/NTU202300192

4.1.3 Occurrence of coherent structures

In the simulation, when a particle settles to the inner layer, it might or might not encounter a turbulent coherent strucutre. Whether a particle's movements will be affected by an ejection or a sweep is a random process determined by the PDF of the occurrence of low- and high-drag events as a function of the event duration $\Delta t^+ = \Delta t^+ u_\tau / h$. Agrawal et al. (2020) used direct numerical simulation (DNS) data and experiments to examine the intermittencies of high- and low-drag events in turbulent channel flows. In their research, the high- and low-drag events can correspond to the subsets of ejection Q2 and sweep Q4 events, respectively. They analyzed the time-frequency data of instantaneous wall shear stresses and velocities and used a critical time $\Delta t^+_{cr} = 200$ as the minimum time-duration threshold. If values of the instantaneous wall stress time-series data are higher/ lower than 10% of the mean shear stress longer than Δt^+_{cr}, it would be recorded as high- or low-drag events. The number and duration of the events were used to calculate the PDF of the occurrences in the function of the event duration Δt^+. In their results, Agrawal et al. (2020) found the event occurrence decays exponentially with a longer event duration with the following equation,

$$P(\Delta t^+) = A \exp\left(-\lambda \Delta t^+\right). \tag{4.7}$$

The exponential variables of corresponding high- or low-drag events are listed below in Table.4.2. Agrawal et al. (2020) pointed out that the exponentially distributed decay duration indicates the occurrences of the events are random, i.e., memoryless. Therefore, the Poisson process is applied in the simulation to generate the random occurrences of Q2 and Q4 events according to the mean arriving rate listed in Table 4.2. When a particle settles

doi:10.6342/NTU202300192

down to the inner region, it can then be checked whether it encounters a Q2 or a Q4 event. Then by generating a random value between 0 and 1 as the probability, the duration of the corresponding event can be decided by the provided PDF.

Table 4.2: The PDF of event occurrences as the function of event duration for $Re_\tau = 180$ in turbulent channel flows (Agrawal et al., 2020).

	High drag (Q4)	**Low-drag (Q2)**
λ	0.0251	0.0185
A	0.0247	0.0183

doi:10.6342/NTU202300192

4.2 Simulation results and discussions

The simulation parameters are listed in the Table. 4.3. In the simulation, the selection of time step value is based on the suggestion for a two-dimensional random walk model that the vertical displacement between a Δt should be smaller than the particle diffusion gradient in the vertical direction (Follett et al., 2016; Israelsson et al., 2006),

$$\Delta t < \min\left(\frac{0.1h}{|\frac{\partial \nu_t}{\partial z} - w_s|_{max}}, \frac{(0.1h)^2}{\nu_t|_{max}}\right). \tag{4.8}$$

The time-step is set as $0.05s$, and the total simulation time is $10s$. The time step value is determined by Eq. 4.8. The ensemble simulation results are calculated based on 100,000 sample paths. In the study, the Hurst values should represent different strengths of the coherent structures acting on particles. However, calibration of the Hurst value is difficult without the availability of time-series particle trajectories data subject to the coherent structures near the boundary. Herein, the Hurst value is assumed to be a uniformly distributed random number between 0.51 to 0.7. In Table 4.3, the notation $\mathcal{U}_{[a,b]}$ denotes uniform distribution with PDF $f(x) = 1/(b-a)$ for $x \in [a, b]$.

Table 4.3: Simulation parameters (chapter4)

Simulation parameters	**Value**
Total simulation times (s)	10
Time step (s)	0.05
Realization	100,000
Hurt values	$\mathcal{U}_{[0.51,\,0.7]}$

doi:10.6342/NTU202300192

4.2.1 Ensemble statistics of particle positions

Firstly, one particle trajectory (i.e, one realization) is sketched for demonstration. The ensemble results of particle positions are calculated based on 100,000 realizations. Fig. 4.4 (a) and (b) sketch particle positions along with simulation time in the streamwise and vertical directions. Fig. 4.4(c) shows the Hurst values of every event the particle has encountered along with time, and the number of time steps that represents the duration of the particle engulfed in a Q2 or Q4 is shown in Fig. 4.4(d). In Fig. 4.4(c) and (d), the red lines represent ejections; the blue ones represent the sweeps. In the z direction, the gray dashed line marks out the boundary of the inner layer ($z/h = 0.2$). At the turbulent outer layer ($z/h > 0.2$), the particle' s movements are affected by the flow and fluctuate randomly with $H = 0.5$. As the particle transport and settles to the lower inner layer, its movements might be affected by the events. The demonstration in Fig. 4.4(c) and (d) aim to show that influence of coherent events happens randomly and duration would also differ every time.

Using Monte Carlo simulation, one can obtain the ensemble means, variances and skewness of particle locations in streamwise and vertical directions as shown in Fig. 4.5. Ensemble statistics are calculated based on 100,000 particle trajectories. In the simulation, the initial position of every particle is specified at the water depth, $h = 0.021\,m$. According to Muste et al. (2005), the NS with a diameter of $0.23\,mm$ and a specific density of 2.65 has a settling velocity of $0.024\,m/s$. Therefore, the expected duration is $0.875\,s$ for a sediment particle settles from the water surface to the bottom, which is shown in ensemble means of particles' vertical positions (Fig. 4.5(d)). As for streamwise directions (Fig. 4.5(a)), before the expected settling duration, most particles are moving; therefore,

doi:10.6342/NTU202300192

the ensemble mean of X positions increases faster. After $0.875\,s$, deposition of particles results in a slow increase. The increasing trend of x positions indicates particle motions are active throughout the simulation time. It can be expected that after $0.875\,s$, particles deposit on the bottom from time to time but overall keep moving due to coherent structures.

Differences among particles' x locations increase along with time, causing the growing ensemble variances in Fig. 4.5(b). On the other hand, the ensemble variances in vertical directions in Fig. 4.5(e), though increasing at the beginning, decrease and become stable in the long term because most particles eventually move in a narrow region around the bottom. Fig. 4.5(c) and (f) shows the skewness of particle positions in x and z directions. When a PDF is symmetric, the value of its skewness is zero. While the negative value of skewness suggests the distribution has a left tail, positive skewness indicates the distribution has a longer tail to the right. Both skewnesses of particle positions show a positive value in the end. The positive-value skewness implies a skewed tail of particle positions in both directions. In Fig. 4.5(f), the skewness values reveal that the PDF of particles' vertical positions skews much more to the left compared with the small skewness value in the streamwise direction.

4.2.2 Anomalous particle diffusion

Diffusion exponents γ are calculated based on ensemble variances according to Eq. 2.32 and are shown in Fig. 4.6(c). The multiple-scaling diffusion ranges are a result of particle behaviors. The initial diffusive particle motions depend on the initial condition of particles. Before the expected settling time, when most particles are moving in the streamwise direction, there is few constraint of particle movements in x. Therefore, the first shown

doi:10.6342/NTU202300192

exponent is very close to the normal diffusion, $\gamma_x = 1.012$ at the time $0.05 - 0.3\,s$. The slightly large value of $\gamma_z = 1.197$ is due to the constraint of water surface in the vertical direction. While in the model, the bottom is the boundary, the water surface is also another boundary. At the beginning of the simulation, particles have more chances of transporting upward but are constrained by the water surface. However, particles seldom transport upward. Because the particles are NS particles, the majority of particle movements transport downward fast due to large settling velocity. Then the variations of particle locations in x increase yet decrease in z due to particle settling. According to Pierce and Hassan (2020), particles either move or deposit on the bottom resulting in the local-range superdiffusive type in a streamwise direction whose value falls between $2 < \gamma_x < 3$. The observation explains $\gamma_x = 2.753$ at the time $0.7 - 1.1\,s$.

Finally, particles' motions vary within a stable, narrowed ensemble variance. At first glance, a nearly zero value of γ_z at the time $(2.5 - 10\,s)$ might suggest that all particles deposit in the end. Or as suggested by Pierce and Hassan (2020), all particles are buried in a geomorphic scale. However, this simulation demonstrates that ensemble variance values of particle positions are constant in the vertical direction due to an equilibrium situation, and particles are still active according to the increasing ensemble variances in the streamwise direction. Herein, the transitions of the diffusion type stem from the different boundary constraints that affect particles' motions.

doi:10.6342/NTU202300192

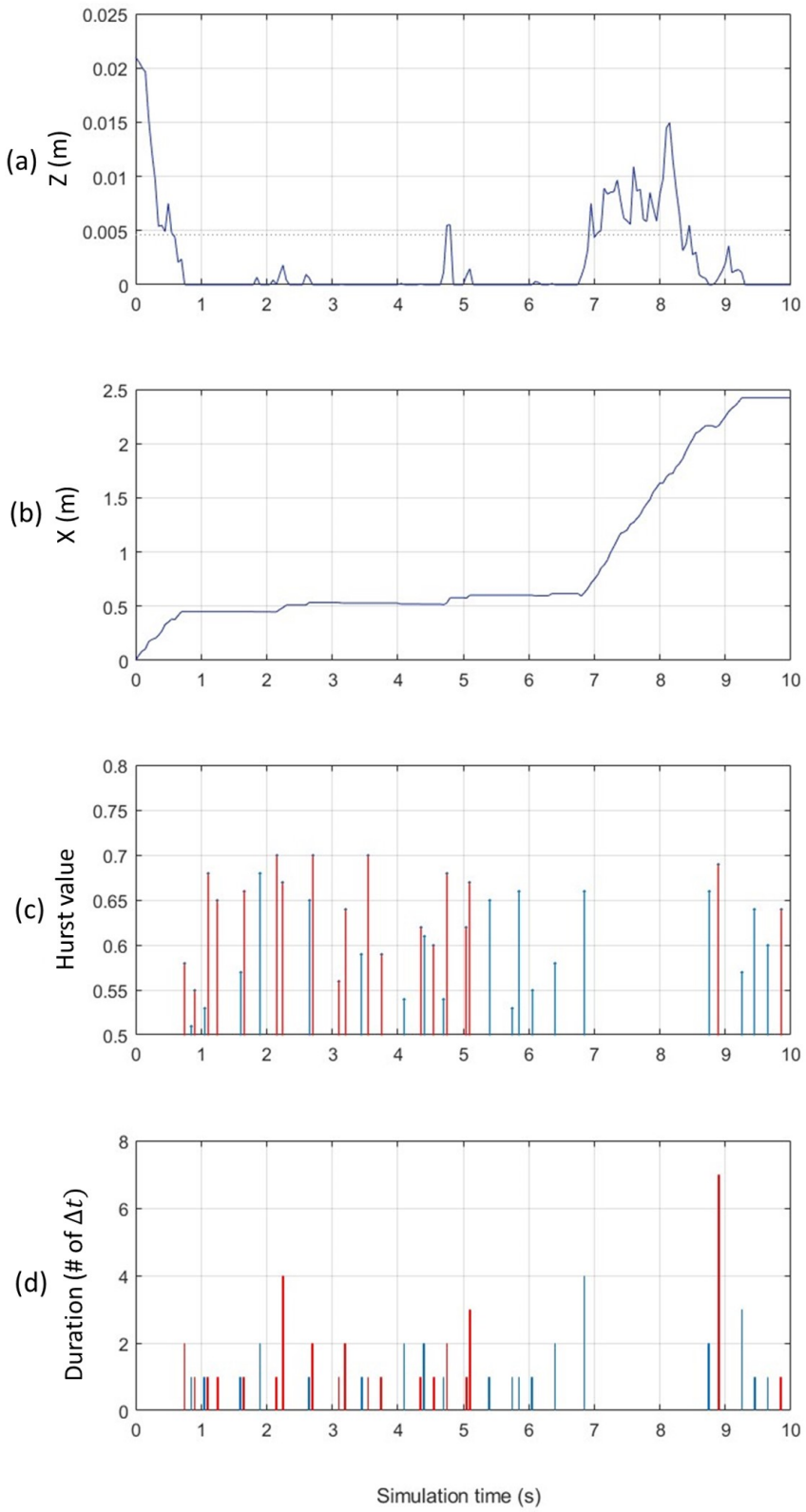

Figure 4.4: One sample path from 100,000 results. (a) Sediment particle positions along with simulation time in (a) vertical and (b) streamwise direction. (c) The Hurst values of every event the particle has encountered along with time. (d) The number of time steps which is the duration of the particle engulfed in a Q2 or Q4. In (c) and (d), the red lines represent Q2, ejections; the blue ones represent Q4, the sweeps.

doi:10.6342/NTU202300192

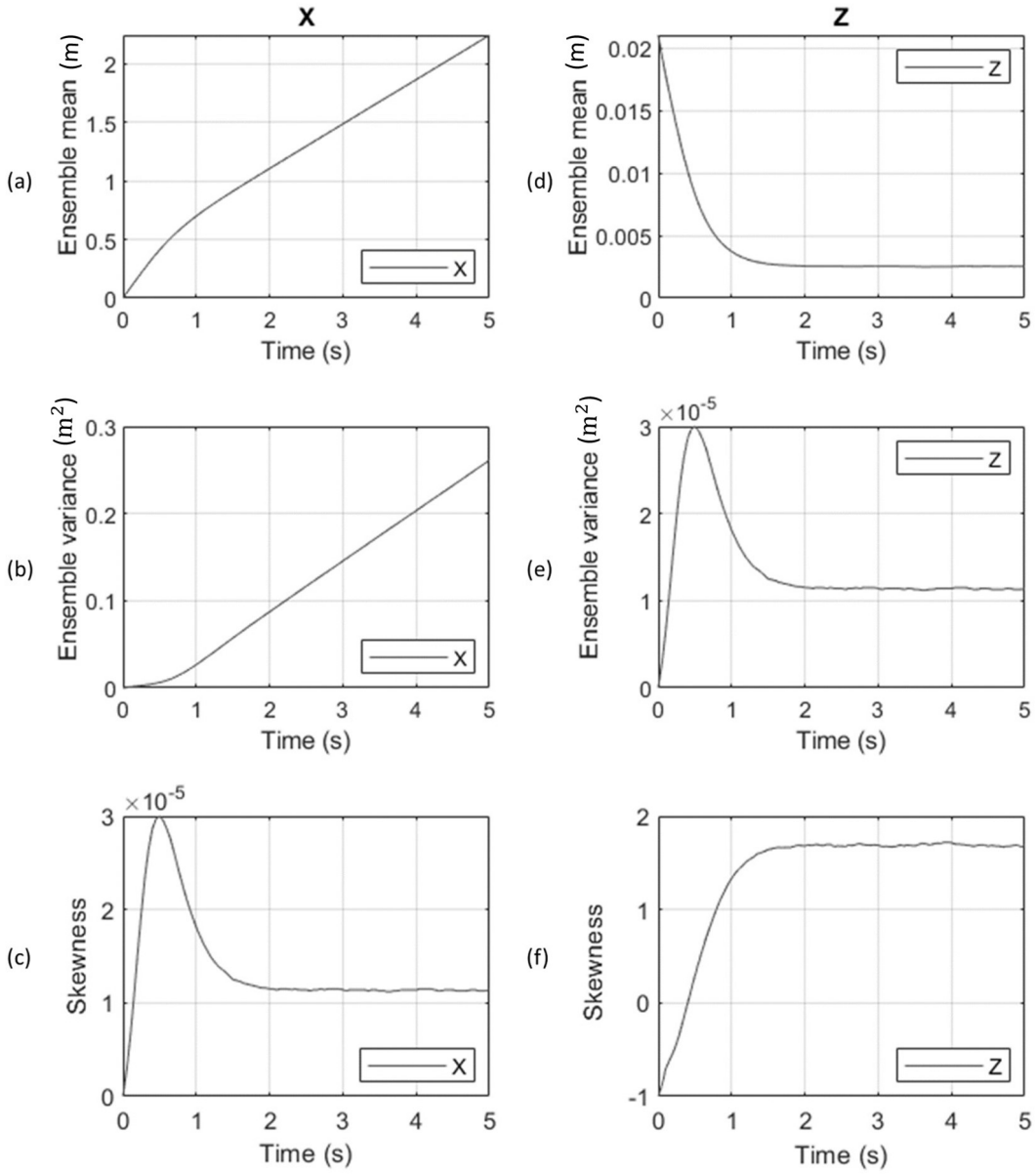

Figure 4.5: The ensemble means, ensemble variances, and skewness of particle location in streamwise x and vertical z directions along with simulation time.

doi:10.6342/NTU202300192

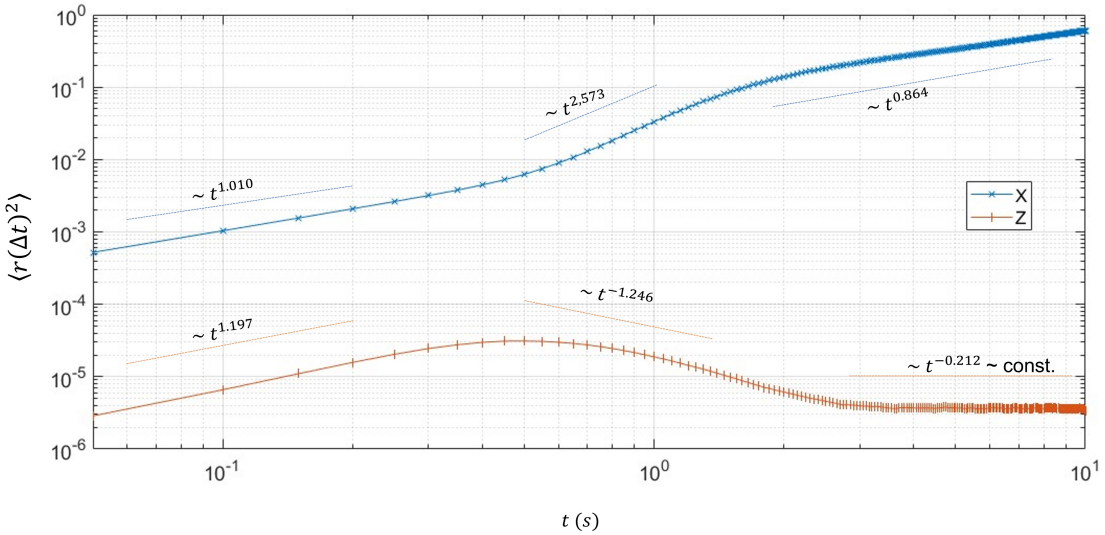

Figure 4.6: Diffusion exponents calculated based on Eq. 2.32. The three time durations for γ calculation are at the time $(0.05 - 0.3)$, $(0.7 - 1.3)$, and $(2.5 - 10)$ s.

doi:10.6342/NTU202300192

4.2.3 Model validation: sediment concentration

Herein, the ensemble particle concentration profile is calculated based on 100,000 particle trajectories. The concentration profiles are calculated based on the number of particles in 20 vertical layers. The concentration profile at a simulation time of 10 seconds is shown in Fig. 4.7. The circles are the concentration data in flume experiments provided by Muste et al. (2005). Simulation results agree well with the experimental data. A minor difference can be observed near the boundary that the concentration results from the simulation are smaller. Compared with the flume experiments, in the simulation, more particles are being lifted and transported to the outer layer.

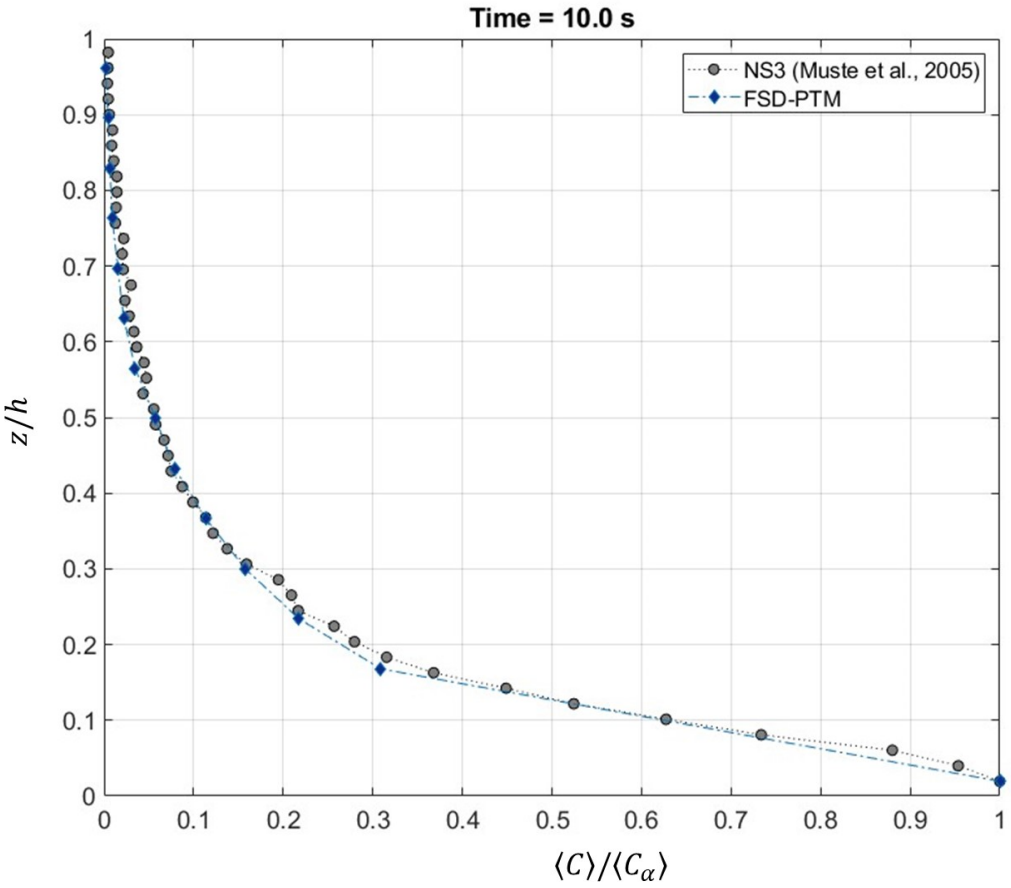

Figure 4.7: Validation with experimental data using ensemble concentration profile at time = 10s. $\langle C_\alpha \rangle$ is the reference concentration at $z/h = 0.05$

doi:10.6342/NTU202300192

The necessity of the proposed model can be observed in Fig. 4.8, which illustrates the comparisons of dimensionless concentration profiles between the SD-PTM and the FSD-PTM at different simulation time 1 , 2 , 3 , 4 , 5 and $10s$. The red line presents the results from FSD-PTM, while the blue dash line is from SD-PTM. At Fig. 4.8 (f), the experimental data from Muste et al. (2005) is added for comparison. The comparisons intend to provide a premise for the argument that the correlated increments resulting from coherent structures play an important role on particles near the boundary. The concentration profile should gradually become stable after the expected settling time of $0.85s$. The concentration profiles from the SD-PTM and the FSD-PTM have a similar trend at the beginning. However, since the particles in the simulation are heavier NS particles, they sink to the bottom quickly and are harder to resuspend. In the proposed FSD-PTM, the correlated increments give the particle a chance to remain in suspension after a particle resuspends. Therefore, along with time, the concentration profiles remain stable after achieving equilibrium. On the other hand, particles in SD-PTM applying the same resuspension method resuspend from time to time; however, it then settles to the bottom soon due to a larger settling velocity. Over time, more particles deposit, and the concentration profile of SD-PTM starts to disintegrate. Eventually, concentration profiles of SD-PTM show that in the long term, most particles remain on the bottom. The results of concentration profiles in Fig 4.8 suggest that introducing the fractional stochastic process to PTM improves the prediction of sediment concentrations near the boundary in the long term.

doi:10.6342/NTU202300192

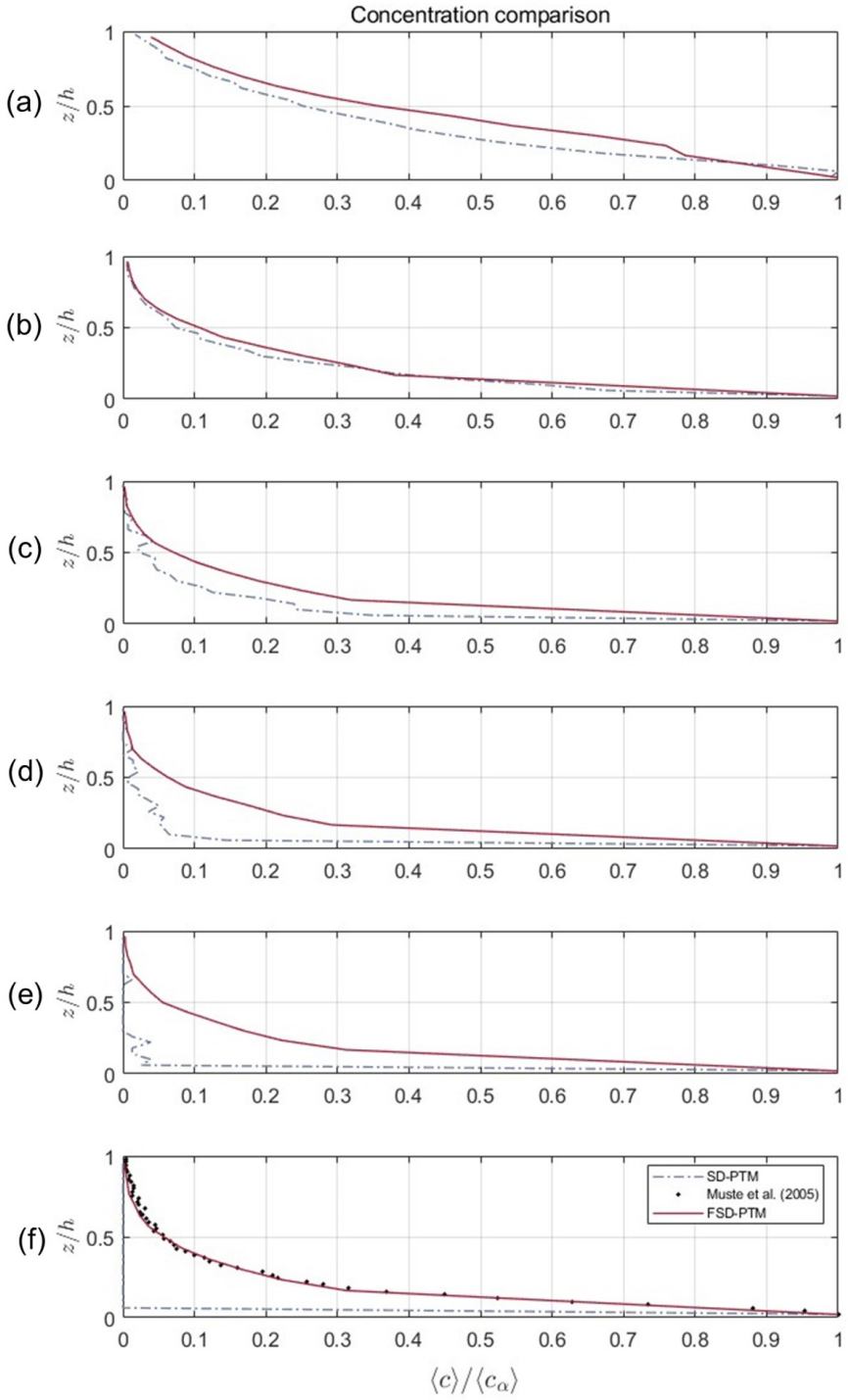

Figure 4.8: Concentration comparisons between SD-PTM (blue dash line) and FSD-PTM (red solid line): (a) $t = 1.0s$, (b) $t = 2.0s$, (c) $t = 3.0s$, (d) $t = 4.0s$, (e) $t = 5.0s$, and (f) $t = 10s$. C_a is the reference concentration at $z/h = 0.05$. The black dots in (f) are the experimental concentration data from Muste et al. (2005).

doi:10.6342/NTU202300192

4.2.4 Model validation: streamwise particle velocity profile

Particle velocity along with time is calculated using the finite difference method. The numerical formula for the numerical calculation of particle velocity at time t can be written as:

$$*u_p(n) = (X(n+1) - X(n))/\Delta t, \tag{4.9}$$

where Δt is the time step. The velocity can be calculated for each time step in a time series of particle positions. While the vertical position is recorded simultaneously, the ensemble particle streamwise velocity profile is calculated based on particle velocity data at different height in a scale of $10^{-5}m$.

In this study, the ensemble means of streamwise particle velocity are validated using experimental results from Muste et al. (2005). In Fig. 4.9, gray dots (NS3 Sed) are the particle velocities measured in the the sediment-laden flow experiments. The green triangles and red squares are the ensemble results of particle velocities calculated by the SD-PTM and the proposed FSD-PTM, respectively. Overall, the trends are similar; the value of streamwise velocity is the highest at the water surface and declines like a logarithmic profile as the flow height decreases.

The experimental particle streamwise velocities in the turbulent outer region are higher than PTMs near the water surface. This phenomenon might suggest that the wake effect of flow should be included in the simulation near the water surface. Inside the inner layer, Fig. 4.9 reveals the importance of considering the influence of coherent structures. The simulation assumption makes the proposed FSD-PTM the same as the SD-PTM in the outer layer as $H = 0.5$, the FBM becomes the Wiener process. It can be seen that the streamwise particle velocity calculated by the FSD-PTM and SD-PTM overlap when

doi:10.6342/NTU202300192

$z/h > 0.2$. However, the differences between results from two PTMs can be easily distinguished inside the inner layer. The simulation assumption follows the results from Muste et al. (2005) that the velocity lag of the particles is 5.5% slower than the bulk flow velocity in the outer region. Inside the inner region, the velocity used in PTMs to calculate particle locations is the bulk flow velocity without velocity lag. The results from SD-PTM transit quickly to the value of calculated flow velocity. On the other hand, though a little bit slower, the ensemble streamwise particle velocities of FSD-PTM match much better than SD-PTM compared with experimental data (NS3 Sed).

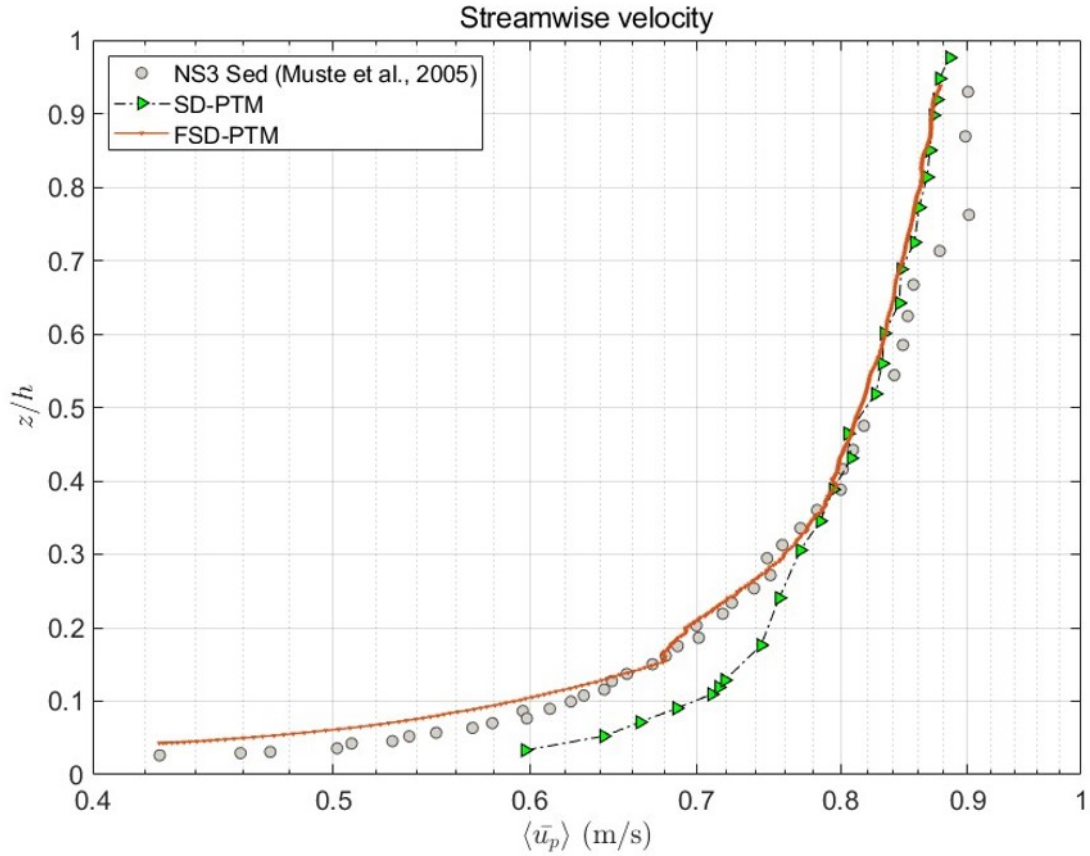

Figure 4.9: The streamwise particle velocities. The circles (NS3 SED) are sediment velocity data from the experiments (Muste et al., 2005). The red line are the ensemble mean of simulation results from the proposed FSD-PTM while the green triangles are from the original SD-PTM.

doi:10.6342/NTU202300192

4.2.5 Distributions of particle velocity fluctuations

The distributions of particle velocity fluctuations at four different heights are shown in Fig. 4.10. We record all the sample paths along with simulation time. In other words, every particle's location is recorded during the simulation, and the velocity fluctuation can be calculated by eliminating the ensemble averaged velocity. In Fig. 4.10, it can be seen that close to the boundary, the number of data points becomes larger. It is because particles' movements concentrated more near the boundary due to gravity for most of the simulation time. The not-so-small settling velocity makes particles spend less time in upper regions. Moreover, closer to the boundary, the particle velocity transforms like a delta function. The phenomena can be attributed to the influence of the boundary. In Fig. 4.10 (a), $z/h = 0.05$ where is in the vicinity of the reference height, most adjusted particle vertical velocities are larger than zero. On the other hand, at the higher region, particle vertical velocity fluctuates freely, and the values can either be positive or negative.

doi:10.6342/NTU202300192

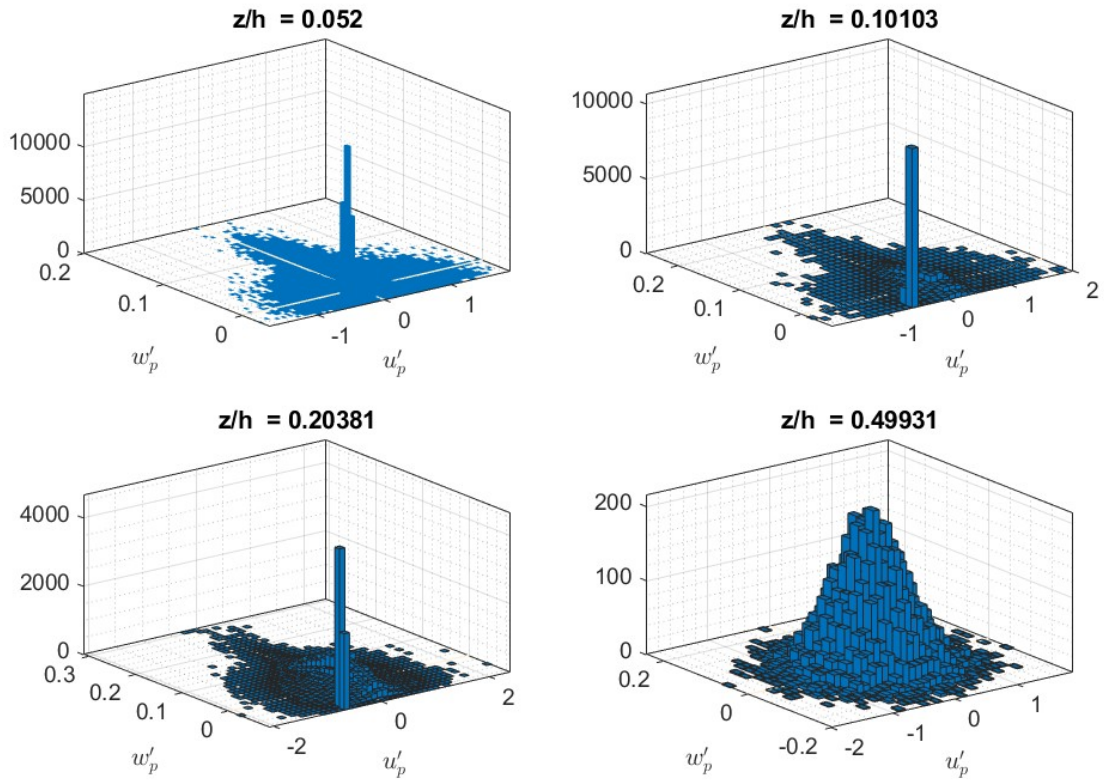

Figure 4.10: Distributions of particle velocity fluctuations at different water depths: (a) $z/h = 0.05$, (b) $z/h = 0.10$, (c) $z/h = 0.20$, and (d) $z/h = 0.50$

doi:10.6342/NTU202300192

doi:10.6342/NTU202300192

Chapter 5

Interpretation of Hurst parameter value

The Hurst parameter is a parameter used to describe the long-range dependence properties of an FBM. The Hurst parameter, denoted by H, takes on values in the range $0 < H < 1$ and is used to determine the strength of the dependence between increments of the FBM over different time scales. Most research analyzes time-series data that can characterize the memory by the Hurst parameter or a so-called Hurst exponent. In most time-series data, the Hurst value measures the persistence of a time-series pattern, where a low Hurst value indicates weak persistence and a high Hurst value indicates strong persistence.

Different time-series data can lead to a different interpretation of the Hurst parameter. A popular example is heart rate variability (HRV). HRV is a measure of the variation in time between consecutive heartbeats and is used as a non-invasive indicator of the balance between sympathetic and parasympathetic nervous system activity. Yeragani et al. (1993) discusses the concept of HRV and its association with panic disorder. The author mentions that HRV can be analyzed using various time-domain, frequency-domain, and non-linear techniques, including ”Hurst exponent analysis.” The Hurst parameter is a measure of the

doi:10.6342/NTU202300192

persistence of the HRV pattern, and a low Hurst value indicates a lack of persistence and is associated with increased sympathetic nervous system activity.

If the research is about stock prices in the financial field, a low Hurst value in the time-series data can indicate that any large increases or decreases are likely to be followed by fluctuations in the opposite direction rather than a persistent trend. Since the Hurst value measures the persistence of a time-series pattern, where a low Hurst value indicates weak persistence, a high Hurst value, on the other hand, indicates strong persistence. Therefore, a high Hurst value in a stock price time-series data suggests that the stock price fluctuations are persistent and that the stock price may be subject to less volatility and becomes more predictable.

In engineering applications, ever since the hydrologist Hurst examined the Nile river discharge variations and found the statistical dependency from the time-series water discharge data (Hurst, 1957), lots of research confirmed the non-Gaussian properties in geophysical records. The Hurst parameter is often used to characterize long-range dependence and irregular fluctuations that exhibit in stream flow, rainfall, and floods (Mandelbrot and Van Ness, 1968; Mandelbrot and Wallis, 1969).

A high Hurst value for river flow data indicates that the river flow has long-term persistence, which means that the flow in one year will likely be similar to the flow in the next year. A high Hurst value for climate data, such as temperature or precipitation, suggests that the climate changes gradually and consistently over time. Moreover, a high Hurst value for geophysical data, such as earthquakes or volcanic eruptions, indicates that the data has a long-term dependence, suggesting that the frequency and magnitude of events are likely to persist over time. In these applications, the Hurst parameter provides

doi:10.6342/NTU202300192

valuable information about the persistence and memory properties of the underlying time-series random process. Accordingly, the Hurst value plays a crucial role in the future prediction of these random processes.

In the previous chapter, the proposed FSD-PTM is validated against experimental flume data. However, the Hurst value has not yet been directly calibrated in a physical manner. In chapter 4, the Hurst value is a presumed uniform distribution in the earlier simulation. Given that the most decisive advantage of applying the FBM is to include the non-Gaussian fluctuations quantitatively by determining the Hurst value. Understanding the physical meaning of fractional dynamics in Hurst value can make applications of the proposed FSD-PTM more practical.

The study's underlying hypothesis is that particles' movements are not memoryless when a time-persistent flow event carries suspended sediment particles. Thus the value of the Hurst parameter can be determined by the flow events. This chapter provides another application for suspended sediment transport in geophysical events such as floods. Since the flood event carrying suspended sediment particles has time-persistent properties, sediment particles' movements are not memoryless. Thus the value of the Hurst parameter can be determined by the flow events such as flow discharge. In such a case, the determination of Hurst value can stand for a meaningful particle transport property by a robust calibration.

5.1 Estimation of Hurst value

In terms of the estimation of Hurst value, there are different methods, such as rescaled range (R/S) analysis, detrended fluctuation analysis (DFA), variance ratio method, and

doi:10.6342/NTU202300192

wavelet analysis. Herein, we provide the estimation based on the second-order wavelet analysis in the wavelet domain (Flandrin, 1992; Pipiras and Taqqu, 2017) . Given any resolution 2^J, a wavelet-based representation of the FBM is

$$B_t^H = B^H(t) = 2^{-J/2} \sum_{n=-\infty}^{\infty} a_{J,n}\, \phi(2^{-J}t - n) + \sum_{j=-\infty}^{J} 2^{j/2} \sum_{n=-\infty}^{\infty} d_{J,n}\, \psi(2^{-J}t - n)\,, \tag{5.1}$$

where $a_{J,n}$ and $d_{J,n}$ are wavelet coefficient and approximation coefficient,

$$\begin{aligned} a_{J,n} &= 2^{-j/2} \int_{-\infty}^{\infty} B^H(t)\phi(2^{-j}t - n)dt\,, \\ d_{J,n} &= 2^{-j/2} \int_{-\infty}^{\infty} B^H(t)\psi(2^{-j}t - n)dt\,. \end{aligned} \tag{5.2}$$

The index $n \in \mathbb{Z}$ refers to discrete location, and index $j \in \mathbb{Z}$ to scale or resolution. The function ϕ and ψ are orthogonal wavelet functions. ϕ is known as a scaling function (father wavelet) and $\psi(t)$ as a wavelet (mother wavelet) satisfied the admissibility condition

$$\int_{-\infty}^{\infty} \psi(t) = 0. \tag{5.3}$$

$\phi(2^{-J}t - n)$ is the translated copies of ϕ, and that $2^{j/2}\psi(2^{-J}t - n)$, is the translated and scaled copies of of ψ. The variance of wavelet coefficients is

$$\mathrm{Var}(d_{j,n}) = \frac{\sigma^2}{2} V_\psi(H)(2^j)^{2H+1}\,, \tag{5.4}$$

where $V_\psi(H)$ is a constant depending on the chosen wavelet and Hurst parameter,

$$V_\psi(H) = -\int_{-\infty}^{\infty}\int_{-\infty}^{\infty} \psi(t)\psi(t-\tau)|\tau|^{2H} dtd\tau. \tag{5.5}$$

doi:10.6342/NTU202300192

The Hurst value can be obtained based on the slope of the power-law behavior of the wavelet coefficient variance in Eq. 5.4,

$$log_2(\text{Var}(d_{j,n})) = (2H+1)j + \text{constant}. \tag{5.6}$$

doi:10.6342/NTU202300192

5.2 Application to suspended sediment transport in a geophysical-scaled flow event

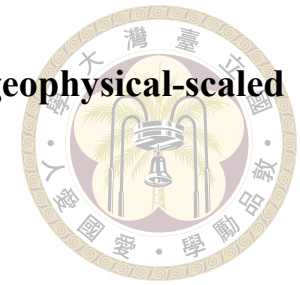

> ”A strength of the theoretical model is its versatility, which should allow consideration of scenarios much closer to reality”
>
> *Christophe Ancey*

For the present section, we attempt to apply the proposed FSD-PTM to suspended sediment transport in a more realistic yet simplified situation: the suspended sediment transport during a typhoon event in a reservoir. Typhoon events are mature tropical cyclones that can cause severe disasters due to strong winds and torrential rains. Floods caused by heavy rains might carry large amounts of suspended sediments and shorten the lifespan of a reservoir.

In the simulation, Typhoon event is the Typhoon MEGI struck Taiwan in September 2016. The Typhoon MEGI made its landfall on Taiwan at 2:00 p.m. on 27 September and left 7 hours later at 9:00 p.m. The sea warning was lifted at 5:00 p.m. on 28 September. According to the National Science & Technology Center for Disaster Reduction of Taiwan (NCDR), Typhoon MEGI caused landslides and flooding events, which resulted in economic losses estimated to NTD 3.3 billion and almost 4 million houses suffered from electric power outages.

As for the study area, the suspended sediment transport simulation is in the Shihmen reservoir as shown in Fig. 5.1. In northern Taiwan, the Shihmen reservoir is a rolled rockfill type reservoir that serves for multi-purpose, including power generation, public

doi:10.6342/NTU202300192

water supply, irrigation, and flood control. With only two-thirds of the design capacity left, Shihmen reservoir suffers from sedimentation. Large flooding events make matters worse and exacerbate accumulation sedimentation problems. Therefore, modeling suspended sediment transport during a typhoon event can provide relevant information for the Shihmen reservoir management.

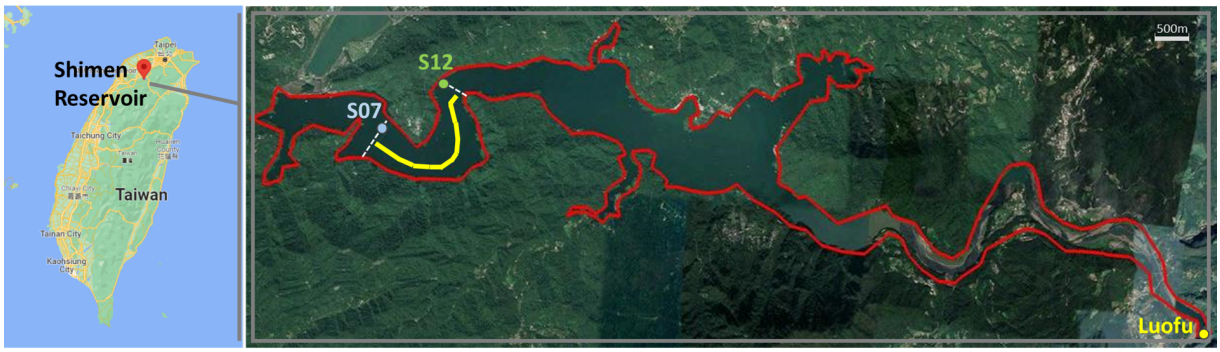

Figure 5.1: Study area: Shihmen Reservoir. Hydrograph was measured at Luofu station, shown at the bright yellow spot on the map at the right corner. The upstream station is station S12 and downstream station is S07.

5.2.1 Simulation assumptions

The proposed FSD-PTM is used to simulate suspended sediment transport in parts of the Shihmen reservoir during the MEGI typhoon. The simulation is a 2-D simulation in the streamwise and vertical directions. The simulation time duration is 24 hours in total, from 11:00 p.m., 27 September to 11:00 p.m. 28 September. However, with regard to the availability of the in-situ data, some simplifications and assumptions have been made for the simulation.

The first simplification is the constant Hurst value. The flow discharge pouring into the Shihmen reservoir during Typhoon is shown in Fig. 5.2. Herein, the Hurst parameter is determined based on the recessional limb of the hydrograph, highlighted as the gray area in Fig. 5.2. For the purpose of showing the long-range dependent flow property during

doi:10.6342/NTU202300192

Typhoon event, the autocorrelation function of the hydrograph after the peak discharge is examined in Fig. 5.3. The value of autocorrelation is always greater than zero, proving the relevance of considering the time-persistence property of flow events. The Hurst value of the discharge after the peak is 0.64, calculated by the wavelet estimation method introduced in the previous section.

The second simplification has no mean drift flow velocity. It is intuitive to assume that flow velocity becomes zero when a river's discharge enters a vast water body, like a reservoir. In the simulation, the suspended sediment transport is simulated between station S12 and S07, where time-series concentration data during typhoon MEGI at different elevations is available. The simulation area is away from the inlet station, Luofu station, the entrance station of the Shihmen reservoir, represented by a bright yellow dot in Fig. 5.1. Consequently, the zero mean drift velocity assumption is made in the simulation.

The last simplifications are a constant water level and constant diffusion coefficients. In the simulation, the initial position is at station S12, and the model results are validated with in-site concentration data at station S07. The distance between the two stations is 2.35 km, demonstrated as the yellow path in Fig. 5.1. Compared with the whole reservoir, the simulation domain between the two stations is relatively small; hence with roughly the same bed elevation (elev. $\approx 190.0m$), the water level is assumed to be a constant (elev. $\approx 243.16m$). Similarly, the diffusion coefficients in streamwise and vertical directions are set as time-averaged constants, $\varepsilon_x = 5.0m^2/s$ and $\varepsilon_z = 1.0 \times 10^{-5}m^2/s$. The diffusion coefficients are determined by the Hydrodynamics module of the Environmental Fluid Dynamics Code (EFDC). Liu (2021) utilized the EFDC coupled with genetic algorithms to search out the optimal parameters for quantifying sediment concentrations during Typhoon MEGI in 2016. The simulation uses the same particle properties and flow environmental

doi:10.6342/NTU202300192

parameters listed in Table 5.1.

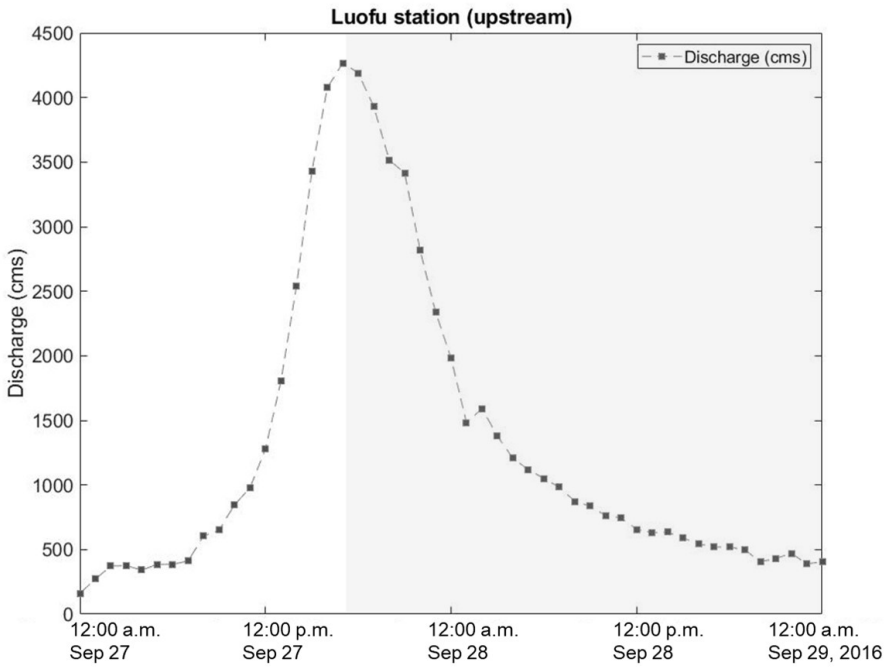

Figure 5.2: Hydrograph at Luofu station, the inlet station of Shihmen reservoir from 12:00 a.m. Sep 27 to 12:00 a.m. Sep 29, 2016.

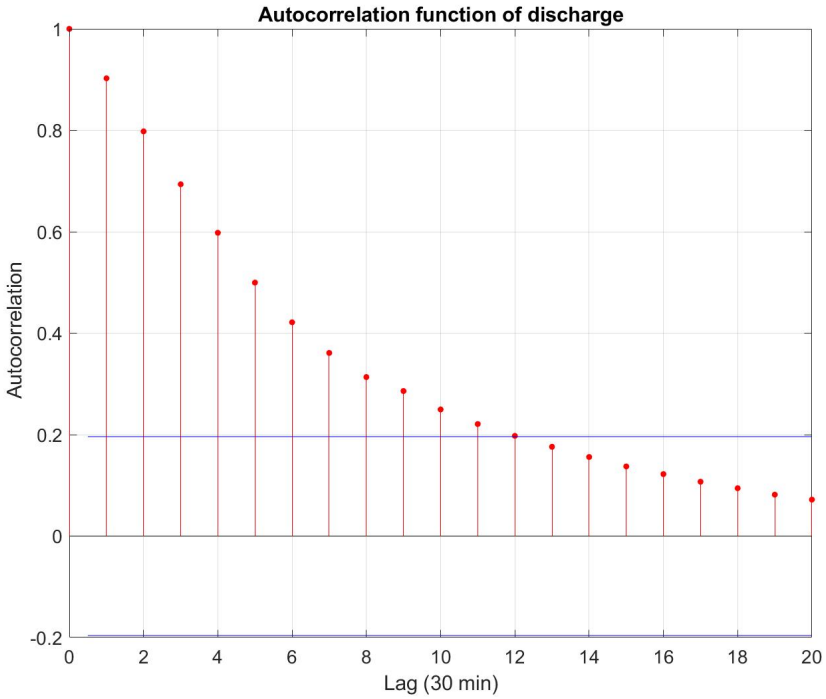

Figure 5.3: The autocorrelation function of hydrograph with the upper and lower confidence bounds drawn as blue lines.

doi:10.6342/NTU202300192

Table 5.1: Simulation parameters (chapter5).

Parameter (EFDC)	**Value**	**unit**
Sediment diameter	50	μm
Specific gravity	2.65	-
Settling velocity	0.0236	m/s
Bed roughness	0.0294	-
Critical shear stress	0.00015	m/s
Modeling Parameter	**Value**	**unit**
Total simulation time	24	hr
Time step	5	s
Monte Carlo simulation[a]	1000	-

[a] Every realization contains 11200 particle units.

Resuspension of suspended sediments

In suspended sediment transport, resuspension is a random process that follows a picked-up probability, also known as entrainment probability. The basis of sediment resuspension is a force balance between the instantaneous lift force from the flow and the submerged particle weight from gravity. Along with the growing attempts to study temporal and spatial properties in wall-bounded turbulence, a probabilistic viewpoint is applied to analyze the incipient motion of sediment particles. Different picked-up probability models as a function of bed shear stress or near-bed velocity fluctuations are developed and validated according to experimental observations (Bose and Dey, 2010, 2013; Cheng and Chiew, 1998; Chien and Wan, 1999; Einstein, 1950; Einstein and El-Samni, 1949; Elhakeem et al., 2017; Subhasish et al., 2020; Wu and Chou, 2003; Wu and Lin, 2002).

Herein, a probabilistic approach proposed by Bose and Dey (2013) can be utilized to determine the resuspension of a suspended sediment particle. The threshold of the sed-

doi:10.6342/NTU202300192

iment suspension is the comparison of vertical flow velocity fluctuation w' and settling velocity of a sediment particle. If the vertical velocity fluctuation exceeds the particle settling velocity, $w' > w_s$, then the particle will resuspend or remain suspension. In other words, whether a suspended particle would be picked-up by the near-bed flow turbulence caused by the bursting phenomenon is a random process that follows a one-sided exponential distribution that can be expanded by a truncated Gram–Charlier series,

$$\begin{aligned} P(w' \geq 0) &= \frac{1}{16}(17 + \hat{w} - \hat{w}^2)\exp\{-\hat{w}\} \\ P(w' < 0) &= 0, \end{aligned} \tag{5.7}$$

where $\hat{w} = w'/\sigma_{w'}$ is defined by the standard deviation of vertical velocity fluctuations $\sigma_{w'}$.

doi:10.6342/NTU202300192

5.2.2 Simulation results and discussions

The proposed FSD-PTM is used in the simulation to simulate suspended sediment transport between stations S12 and S07. The time-series in-situ concentration data measured at different elevations at the upstream station S12 is assumed to be the continuous sediment inputs. According to in-situ concentration data, every 30 minutes, different particle units would be released in the domain as the black lines demonstrated in Fig. 5.4(b). Then the sediment concentrations are calculated every 30 minutes, along with the simulation time at station S07. To give a more specific understanding of the simulation, Fig. 5.4 depicts some sample paths for demonstrations. Fig. 5.4 (a) shows the inputs at different elevations, and Fig. 5.4 (b) depicts some sample paths at the beginning and a later input after eight and half hours.

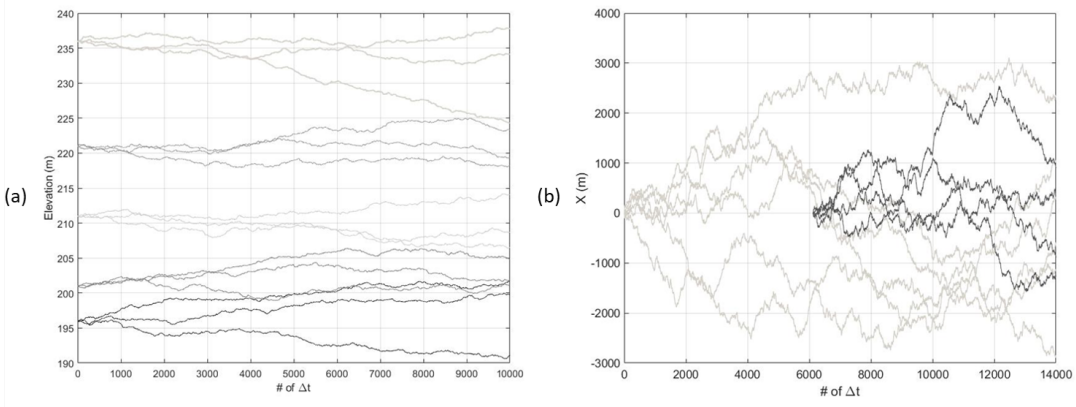

Figure 5.4: (a) Demonstration of input at different elevations. (b) Demonstration of continuous inputs.

Calculations of sediment concentration are based on the particle number at the 2.35 km downstream to compare with the in-situ concentration data at station S07. The Concentration results of one simulation at different elevations are shown in Fig. 5.5. The black dots represent the in-situ concentration data at downstream station S07, and the red circles are the concentration results from only one simulation. The in-suit measured concentra-

doi:10.6342/NTU202300192

tions data decreased along with the time since the simulation started when the discharge decreased after the peak discharge. On the other hand, as can be seen, the concentration results are close to zero at the beginning and then increase along with time. The zero values result from zero particles arriving at the downstream station S07 at such an early stage. With zero particles at the beginning, the concentration is zero in the simulation. Concentration increases when more and more particle units are released and transport downstream. Although the results of one simulation are only one plausible outcome, the purpose of demonstrating is to roughly make a comparison with the in-situ concentrations data, which are also one of plausible results that may happen in reality. The rough concentration comparison between simulation results and in-situ data reveals that without any particles in the domain initially, it would take some time for simulation results to be relevant. In this situation, it takes about 18 hours. A quick glance at Fig. 5.5 might suggest that the last 6 hours' simulation results and the field data points are from the same cluster. To further examine the simulation results, ensemble statistics should be calculated.

Via the Monte Carlo method, ensemble concentrations are calculated based on 1000 simulations and are shown in Fig. 5.6. Ensemble results plus or minus one standard deviation are drawn for the last 6 hours. Most in-situ data points fall within the range covered by the ensemble mean plus and minus one standard deviation. With zero mean velocity and constant diffusivity assumptions, the mean drift terms, except for the settling velocity, are equal to zero, and only the turbulence terms are left in the governing equation. The governing equation becomes the FGN process with diffusion coefficients acting as the weighting factors. Since the FGN is a Gaussian process, the Gaussian shape can be expected in the ensemble results. We have also used SD-PTM to model the suspended sediment transport to make a comparison. However, concentrations from the SD-PTM show that most par-

doi:10.6342/NTU202300192

ticles cannot arrive downstream station S07 before the end of the simulation. Ensemble concentration results of the SD-PTM depicted as the square points in Fig. 5.6 are almost always zero along with time. The substantial difference between ensemble concentration results of the proposed FSD-PTM and the SD-PTM shows the necessity of considering the memory effect in suspended particles' movement. With the Hurst parameter capturing the time-persistent property of carrying flow, the proposed FSD-PTM can then describe the non-Gaussian turbulent fluctuations by the fractional process with the specified Hurst value.

doi:10.6342/NTU202300192

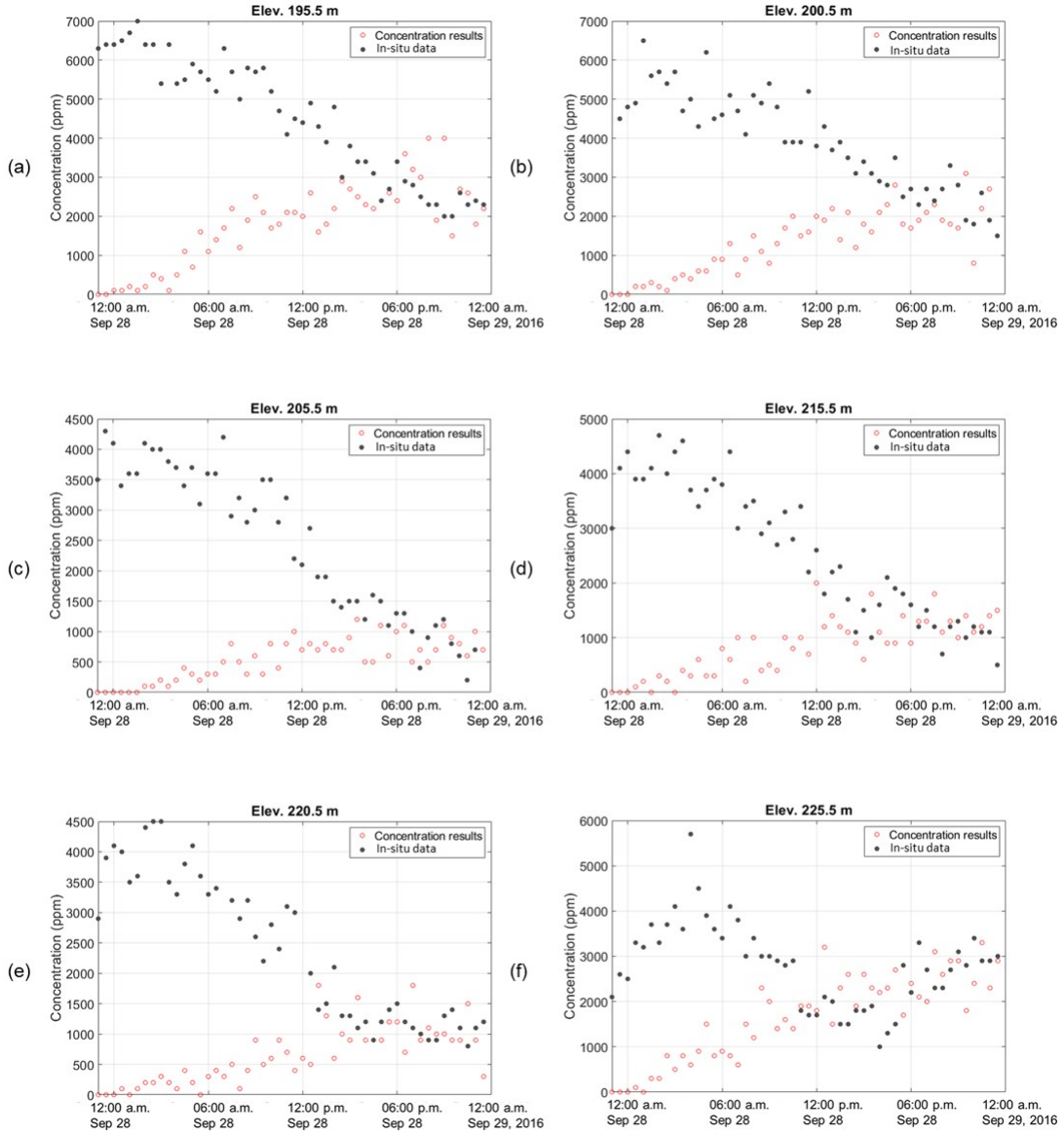

Figure 5.5: Concentrations results of one simulation at different elevations:(a) 195.5 m, (b) 200.5 m, (c) 205.5 m, (d) 215.5 m, (e) 220.5 m, and (f) 225.5 m.

doi:10.6342/NTU202300192

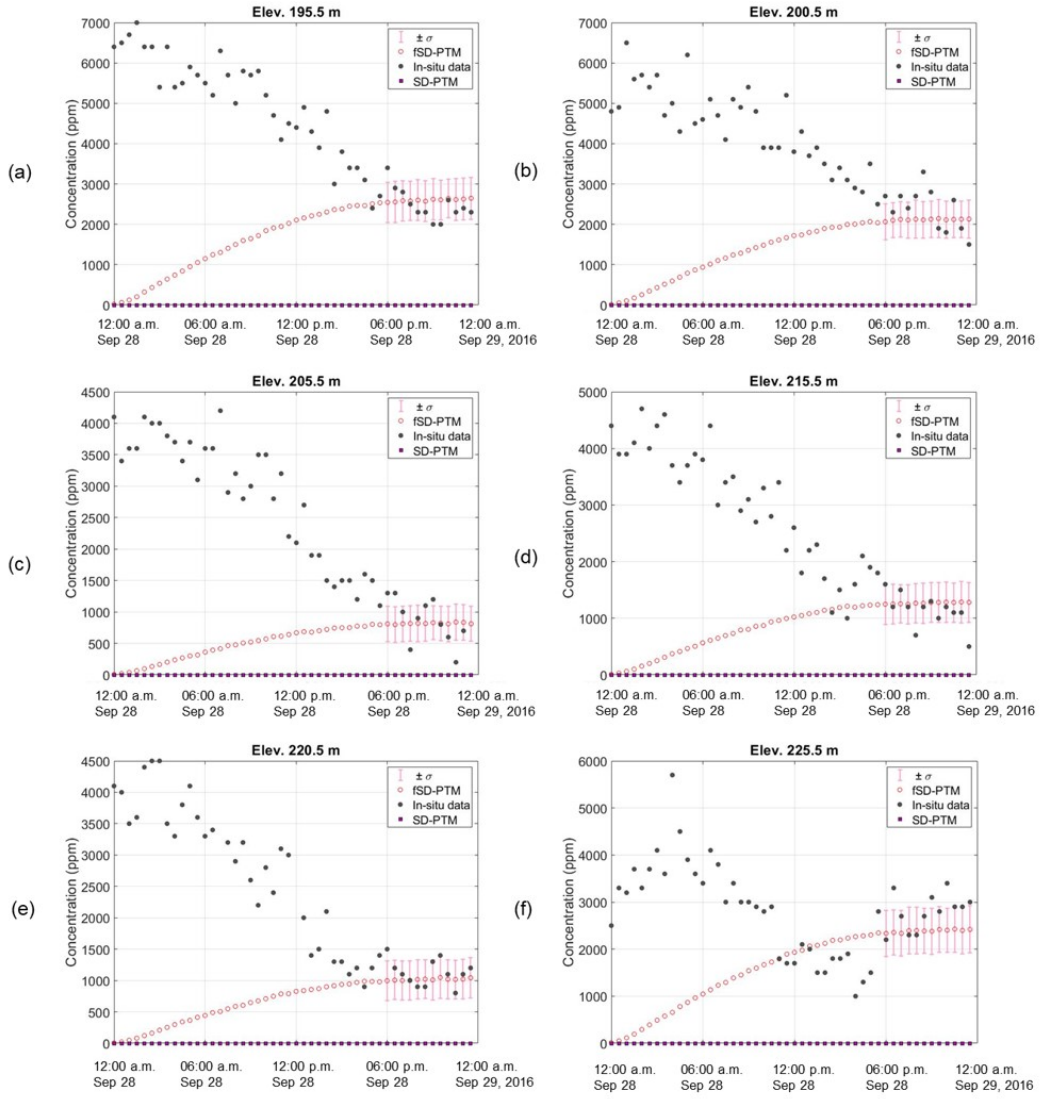

Figure 5.6: Ensemble concentrations results at different elevations:(a) 195.5 m, (b) 200.5 m, (c) 205.5 m, (d) 215.5 m, (e) 220.5 m, and (f) 225.5 m.

doi:10.6342/NTU202300192

5.2.3 Summaries of the application

Ever since the hydrologist Hurst examined the Nile river discharge variations and found the statistical dependency from the time-series water discharge data (Hurst, 1957), lots of research confirmed the non-Gaussian properties in geophysical records, such as stream-flow, rainfall, and floods (Mandelbrot and Van Ness, 1968; Mandelbrot and Wallis, 1969). It, therefore, appears to be necessary to consider the impact of this dependency property of flows on suspended sediment transport.

In this research, the underlying assumption is that when suspended sediments transport within the time-persistent flows, the spread of sediments will not follow the Fickian law. In order to describe the non-Fickian diffusive behaviors of sediments, this thesis introduces the fractional concept to PTMs. The proposed FSD-PTM aims to simulate the suspended sediment transport with memories. Herein, "memory" is mathematically defined as the long-range dependency of a stochastic process. The governing equation of the proposed FSD-PTM is an SDE driven by the FBM. The aim of replacing the Wiener process with the FBM is to describe the fractional fluctuations in suspended particles' movements caused by the long-time persistent flood. With Hurst parameter value larger than $1/2$, the auto-correlation value of the FBM increments, the FGN, is positive and therefore indicates the increments are dependent, not memoryless. The correlated increments of the FBM make the FSD-PTM a robust stochastic model to describe the random sediment movements with memories in time-persistent flow events.

The simulation of suspended sediment transport during a typhoon event in a reservoir is demonstrated in this chapter. The positive auto-correlation values of the flow discharges confirm the time-persistent flow property and also show the relevance of considering frac-

doi:10.6342/NTU202300192

tional fluctuations in suspended particles' movements. Results of sediment concentrations reveal that the proposed FSD-PTM has a better prediction than the SD-PTM. This study focuses on suspended sediment transport in a larger-time scale time-persistent flow. Though the application is oversimplified, it serves as a good start at the geo-morphological scale. We want to use this application to show how a Hurst parameter can be defined based on the long-ranged property of a flow event that carries suspended sediment particles.

doi:10.6342/NTU202300192

Chapter 6

Conclusions

This study proposes an advanced Lagrangian PTM for suspended sediment transport. The suspended sediment particles are settleable solids that are fine enough to be carried by turbulence. Consequently, turbulent flow properties significantly influence suspended particles' movements. Since the existence of coherent turbulent structures has been discovered, the interplay between time-persistent coherent structures and sediment particles has been examined by lots of field and flume experiments. It has been suggested that the ejections can pick sediment particles up, and sweeps cause more particles to deposit on the bed. The quadrant analysis of coherent structures revealed anisotropic flow velocity fluctuations near the boundary. Therefore, it is pointed out that the existence of time-persistent coherent structures in the inner layer ($z/h < 0.2$) causes the non-Gaussian anomalous fluctuations of suspended sediment particles' motions. The study introduces a fractional stochastic process, the FBM, to address the correlated fluctuations of particles' movements subject to anisotropic turbulence. The correlated increments of FBM make it a robust stochastic process to model dependent sediment increments in time-persistent flow events. The primary goal of the proposed model is to describe probabilistic sediment

doi:10.6342/NTU202300192

particle trajectories with *memories* caused by coherent turbulent structures. The aim is to better predict sediment concentration and particle velocity profiles near the boundary in open channel flows.

In the study, the proposed FSD-PTM is applied to a steady, incompressible, fully developed two-dimensional open channel flow. The flow conditions and particle properties are from the flume experiments conducted by Muste et al. (2005). While the previous SD-PTMs often applied a finer particle, such as NBS, for model validation, the proposed model chooses the particles with a natural sand density of 2650 kg/m^3. Without considering the correlated movements, concentration profiles of SD-PTM fail to reach an equilibrium in the long term in Fig. 4.8. The comparison of concentration profiles in Fig. 4.8 and particle streamwise velocity in Fig. 4.9 show that by including the influence of coherent structures in correlated increments, simulation results of the proposed FSD-PTM agree well with the experimental data points.

6.1 Advantages and limitations of the proposed FSD-PTM

The availability of this stochastic model can quantify the probabilistic characteristics and corresponding uncertainty of suspended sediment transport, accounting for the influence of time-persistent turbulent flow structures. Such stochastic descriptions via Monte Carlo simulations could better describe the randomness of correlated particle movements. Since the proposed FSD-PTM is a Lagrangian PTM model, the basic advantages include the followings: (1) it always follows mass conservation, (2) it is easy to visualize transport paths, and (3) it is able to calculate the PDF and different statistical moments of trajectories, velocity and corresponding velocity fluctuations of particles. In addition, compared

doi:10.6342/NTU202300192

with other PTMs, the proposed model utilizes the FBM instead of the Wiener process to consider the temporal correlation in particle movements. The substantial difference between the proposed FSD-PTM and the previous PTMs is that the correlated motion is embedded in the random term of the governing SDE without adding another additional term. Furthermore, the FBM can become the Wiener process when $H = 0.5$. Therefore, when turbulence velocity fluctuations become isotropic at the outer layer, the proposed FSD-PTM can still be applied.

On the other hand, the limitation of the model is that the computation expense is higher because ensemble statistics require more sample paths to have a meaningful result. This indicates that insufficient data might cause inexplicable noises. Moreover, the proposed model is a one-particle PTM derived and validated under dilute and equilibrium conditions. It does not consider the secondary flow. Particle-particle interactions such as collisions are not directly included in the model. From the previous discussion, it can be expected that if the particle-particle interaction can be quantified, it could extend the model's applicability. This might be achieved by giving different physical meanings to the Hurst value. The Hurst value is not yet directly calibrated in the application shown in chapter 4 by physical parameters. However, the Hurst value is a flexible parameter that can stand for various physical meanings for different purposes. Therefore, the application for suspended sediment transport in geophysical-scaled flood events is demonstrated in chapter 5. The flood event carrying suspended sediment particles has time-persistent properties, so particles' movements are not memoryless. Thus, the Hurst value can be determined by the flow discharge. In such a case, the determination of Hurst value can stand for a meaningful particle transport property by a robust calibration.

In summary, the FSD-PTM is proposed to describe the probabilistic suspended sed-

doi:10.6342/NTU202300192

iment particle trajectories subject to the influence of coherent structures. The simulation results can scientifically quantify the variations and uncertainties of suspended sediment concentrations and transport rates in open channel flows. Notably, when the probabilistic properties of sediment particles, such as ensemble mean, variance, and skewness of sediment transport rates and concentrations, are made available, a more robust risk assessment required for hydraulic structure design, sedimentation, and water quality control, can thus be calculated. In practice, such information would provide a valuable reference for evaluating the operation risk of hydraulic structures, such as reservoirs, dams, and bridges, in an uncertain future.

doi:10.6342/NTU202300192

Appendix A — Definition

A.1 Markovian property: Memorylessness

Markov process

A Markov process is a stochastic process that satisfies the Markovian property, the memorylessness. The memoryless is intuitively thought that the future prediction depends only on current situation and has nothing to do with the previous historic information. Herein, we provide the example of a type of Markov process: the continuous Markov chain.

Definition A.1.1 (Memorylessness)**.** A stochastic process $\{X(t),\ t \geq 0\}$ is a continuous-time Markov chain with states defined as i, j, and $x(k)$ for all $t \geq a \geq u > 0$, and is said to has memoryless property if

$$\begin{aligned} &\Pr\{X(t+s) = j |\ X(s) = i, X(u) = x(u),\ s \geq 0)\} \\ &\qquad = \Pr\{X(t+s) = j |\ X(s) = i\}. \end{aligned} \tag{A.1}$$

In Eq. A.1, $X(s) = i$ denotes the current state, while $X(u) = x(u)$ denotes all the other historic states the process had been to. In other words, Eq. A.1 shows that the future state only depends on the present state and is independent of the past. If the stochastic

doi:10.6342/NTU202300192

process is interpreted as the location of particles, states would be the particle's position. Then the memoryless property indicates that the next position of a particle depends only on the current locations implying the increments are independent ans stationary.

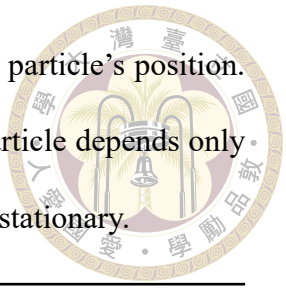

A.2 Memory

In this study, in comparison to the memoryless property with the independent increments, the term *memory* indicates the correlated increments of particles' movements. Specifically, memory shares the same definition of long-range dependence or long-range persistency.

Definition A.2.1 (long-range dependence)**.** If the auto-correlation function of a stochastic process, $\rho(n) := \mathrm{Cov}(X(k), X(k+n))$, decays slowly as n tends to infinity, then the sequence, $\{X(t),\, t \in \mathbb{R}\}$, is said to exhibits long-range dependence (Biagini et al., 2008; Pipiras and Taqqu, 2017).

$$\lim_{n\to\infty} \frac{\rho(n)}{c_1 n^{-\alpha}} = 1\,, \tag{A.2}$$

where $c_1 \in \mathbb{R}$ and $\alpha \in (0,1)$ are constants. The followings are the introductions of FBM and the descriptions of correlated increments.

doi:10.6342/NTU202300192

Appendix B — Stochastic process

This introductory section provides a brief overview of Gaussian process such as the Wiener process, fractional Brownian motion (FBM), fractional Gaussian noise (FGN). Additional stochastic process, the Poisson process, is introduced.

B.1 Gaussian process

Definition B.1.1 (Gaussian process)**.** A stochastic process $\{X(t),\, t \in T\}$ is a *Gaussian process* if one of the following equivalent conditions holds:

(1). For any finite sequence $0 \leq t_1 < ... < t_n$, the finite collection of random variables $\{X(t_1), ..., X(t_n)\}$ has a multivariate Gaussian distribution $\mathcal{N}(\mu, \Sigma)$.

(2). $a_1X(t_1) + ... + a_nX(t_n)$ is a Gaussian random variable for and for any $a_i \in \mathbb{R}$, $t_i \in T$.

(3). For any $a_i \in \mathbb{R}$, $t_i \in T$, when $\mathbb{E}[X(t)] = 0$,

$$\begin{aligned}\mathbb{E}[\exp\{i(a_1X(t_1) + ... + a_1X(t_1)\}] &= \exp\big\{-1/2\ \mathbb{E}[(a_1X(t_1) + ... + a_1ZX(t_1)]^2\big\} \\ &= \exp\left\{-1/2\ \sum_{i,j=1}^{n} a_ia_j\mathbb{E}[X(t_i)X(t_j)]\right\}.\end{aligned}$$

A multivariate Gaussian distribution denoted by $\mathcal{N}(\mu, \Sigma)$ is also known as joint Gaus-

doi:10.6342/NTU202300192

sian distribution. $\mathcal{N}(\mu, \Sigma)$ means a multivariate Gaussian distribution is defined by two parameters, a mean function μ and a covariance function Σ. A centered Gaussian process with mean 0 is completely defined by the second-order statistics, i.e., the covariance function $\Sigma = \text{Cov}(X(t), X(s))$.

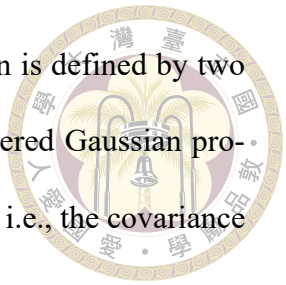

B.2 Wiener process

The Wiener process, sometimes referred to as the Brownian motion process, originated as a mathematical description of Brownian motion. A Wiener process is a centered Gaussian process with zero mean and covariance function listed below,

$$\mu = \mathbb{E}[W(t)] = 0, \quad \Sigma = \mathbb{E}[W(s)W(t)] = \min(s,t), \quad t, s \geq 0 \tag{B.1}$$

Definition B.2.1 (Wiener process)**.** A continuous stochastic process $\{W(t),\, t \geq 0\}$ is said to be a *Wiener process* if

(1). $W(0) = 0$ with probability 1

(2). $\{W(t),\, t \geq 0\}$ has stationary and independent increments

(3). $\{W(t),\, t \geq 0\}$ has Gaussian increments

(4). $\{W(t),\, t \geq 0\}$ is continuous but no where differentiable

The continuous property can be proved when a Wiener process is interpreted as the limit of a random walk,

$$\lim_{s \to 0}(W(t+s) - W(t)) = 0.$$

Stationary increments, as shown in Fig. B.1, indicate that the increments taken over the

doi:10.6342/NTU202300192

blue bold increments have the same distribution. Note that, according to the second property of the Wiener process, the increments $(W(t) - W(s)$ and $(W(t+l) - W(s+l))$ are independent and have the same distribution. The distribution is a Gaussian distribution with mean 0 and variance $(t - s)$ for all $t > s$.

Wiener process has some properties good in math, such as it is a martingale, and it has unbounded variation and finite quadratic variation, i.e., $[W(t), W(t)] = t$. The most important property of the Wiener process, the independent increments, make it becomes the most commonly and widely applied in mathematics, economics, and physics fields.

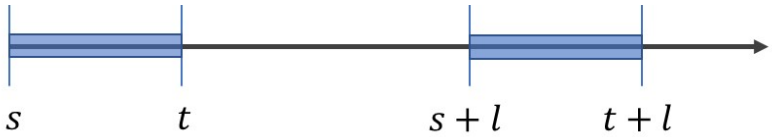

Figure B.1: Stationary increments. The increments $(W(t) - W(s))$ and $(W(t+l) - W(s+l))$

.

Simulation of a Wiener process

To simulate a Wiener process, one can link the simulation of a random walk at a finite subset of time instances. For a finite time T and any positive integer $N \in \mathbb{N}$, the time step is set as $\Delta t = T/N$. Since the initial value start from 0 and the increments of the Wiener process are normally distributed with the variance (Δt), the process can then be computed as,

$$W(t_{n+1}) = W(t_n) + \Delta W(t_n),\ n = 0, 1, 2, ...N. \tag{B.2}$$

where $\Delta W(t_n)$ denotes the increment of a Wiener process and $t_n = n * \Delta t$. The increment is an independent random variable with Gaussian distribution $\mathcal{N}(0, \Delta t)$.

doi:10.6342/NTU202300192

For demonstration, consider a simulation time region $[0, 1]$, with $N = 1000$. The time step is $\Delta t = 1/1000$. The increments are normally distributed with distribution $\mathcal{N}(0, \Delta t)$ or equally $\sqrt{\Delta t}\,\mathcal{N}(0, 1)$. By iteration relation (Eq.B.2), with initial value $W(0) = 0$, one can utilize the independent increments property of a Wiener process to do the cumulative sum up of the increments. Sample paths of the Wiener process are sketched in Fig. B.2. From Fig. B.2(a), 7 sample paths sketched as different colors are totally different. Fig. B.2(b) demonstrates 500 sample paths with a light gray color as long as their ensemble mean is drawn as the red line. As the number of sample paths is large enough, according to the large number law, the ensemble means of samples paths will reach the theoretical mean 0.

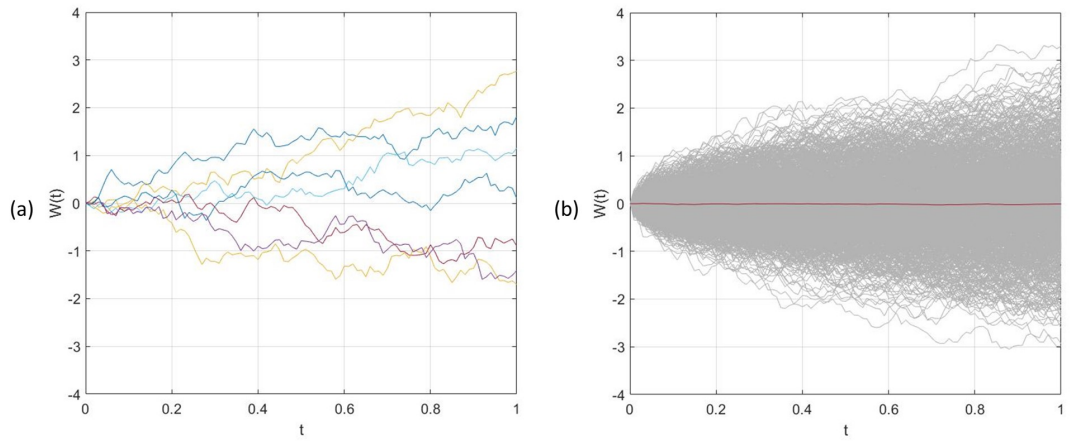

Figure B.2: Sample paths of the Wiener process over time $[0, 1]$ with $N = 1000$. (a). 7 sample paths of the Wiener process (b) 5000 sample paths with ensemble mean of 5000 sample paths (red line).

doi:10.6342/NTU202300192

B.3 Fractional Brownian motion process (FBM)

Initially introduced by Mandelbrot and Van Ness (1968), a standard FBM or fractional Brownian process, $\{B^H(t),\, t \geq 0\}$, with Hurst parameter $H \in (0,1)$ is a self-similar centered Gaussian process defined by the following covariance function,

$$\mathrm{Cov}(B^H(s), B^H(t)) = \mathbb{E}[B^H(s)B^H(t)] = \frac{1}{2}(|s|^{2H} + |t|^{2H} - |t-s|^{2H}), \quad \forall s,t \in \mathbb{R}\,. \tag{B.3}$$

Definition B.3.1 (fractional Brownian motion)**.** A FBM with a standard deviation σ_f has the following properties:

(1). $B^H(0) = 0$ with probability 1

(2). $\mathbb{E}[B^H(t)] = 0$ and $\mathbb{E}[(B^H(t))^2] = \sigma_f^2 t^{2H}$

(3). $\{B^H(t),\, t \geq 0\}$ is continuous but nowhere differentiable

(4). $\{B^H(t),\, t \geq 0\}$ is a self similar process

(5). $\{B^H(t),\, t \geq 0\}$ has stationary and correlated increments

From Eq. B.3, the covariance of FBM becomes the same covariance function of the Wiener process $\min(s,t)$ (Eq. B.1) when $H = 1/2$. Then a FBM turns into a Wiener process.

Simulation of a FBM

Compared with Wiener process with independent increments, the distinguished property of a FBM is that it allows its disjoint increments to be correlated. To get to the bottom

doi:10.6342/NTU202300192

of the dependency property of a FBM, let's consider the sequence of the FBM increments. The incremental process of a FBM is also known as a fractional Gaussian noise (FGN). The increment process $\{Y(t),\, t \geq 0\}$ is defined as,

$$Y(t) = B^H(t+1) - B^H(t). \tag{B.4}$$

A FGN is a stationary Gaussian process with corresponding autocorrelation,

$$\rho(Y(k), Y(k+n)) = \mathbb{E}[Y(k)Y(k+n)] = \frac{1}{2}(|n+1|^{2H} + |n-1|^{2H} - 2n^{2H}) \tag{B.5}$$

According to the autocorrelation function of FGN (Eq. B.5), the increments have a power law decay when $H \neq 1/2$, With $H < 1/2$, the increments are negatively correlated and it is called anti-persistent. Conversely, when $H > 1/2$ the increments are positively correlated, and the process is known as the persistent process. The autocorrelation of a FGN is zero when $H = 1/2$, indicating increments are independent. Thus the collection of the incremental process corresponds to the ordinary Brownian motion.

The sample paths of the FGN with different Hurst values are depicted in Fig. B.3. The variation range of the increments becomes larger when Hurst value become smaller. For the increments without dependency ($H = 1/2$) or anti-persistent ($H < 1/2$), the increments values fluctuate between positive and negative of a certain number. On the contrary, most values of increment when $H > 1/2$ in Fig. B.3 are negative. It can be found that the correlation makes the value of increments concentrated more on negative in this one sample path demonstration.

Having the incremental process, the fractional Brownian process can then be obtained by adding the increments with initial value $B^H(0) = 0$. Three sample paths with different

doi:10.6342/NTU202300192

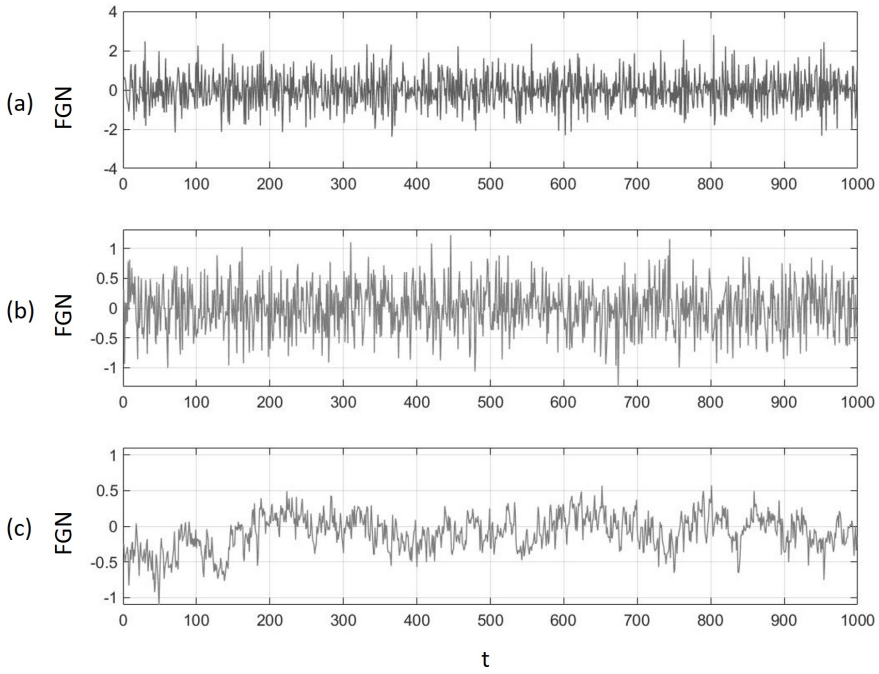

Figure B.3: Sample paths of the FGN: (a) $H = 0.2$, (b) $H = 0.5$, and (c) $H = 0.9$.

Hurst values, $0.2, 0.5,$ and 0.9, are demonstrated in Fig. B.4. The smaller the Hurst value is, the higher frequent fluctuations can be observed from the sample paths. With $H > 1/2$, the sample paths with positive correlations are smoother and can travel further due to the dependent increments.

Correlated increments

To prove the FBM has long-range dependence, one can apply L'Hôpital's rule on Eq. B.5 and find $\rho(Y(k), Y(k+n)) \approx H(2H-1)n^{2H-2}$ when $n \to \infty$. Set $c = H(2H-1)$ and $\alpha = 2 - 2H$, then one can obtain,

$$\lim_{n\to\infty} \frac{\rho(Y(k), Y(k+n))}{H(2H-1)n^{2H-2}}. \tag{B.6}$$

When $H \in \left(\frac{1}{2}, 1\right)$, Eq. B.6 would approach 1. According to definition of Eq. A.2, FBM has long-range persistency on its increments with $H > 1/2$.

doi:10.6342/NTU202300192

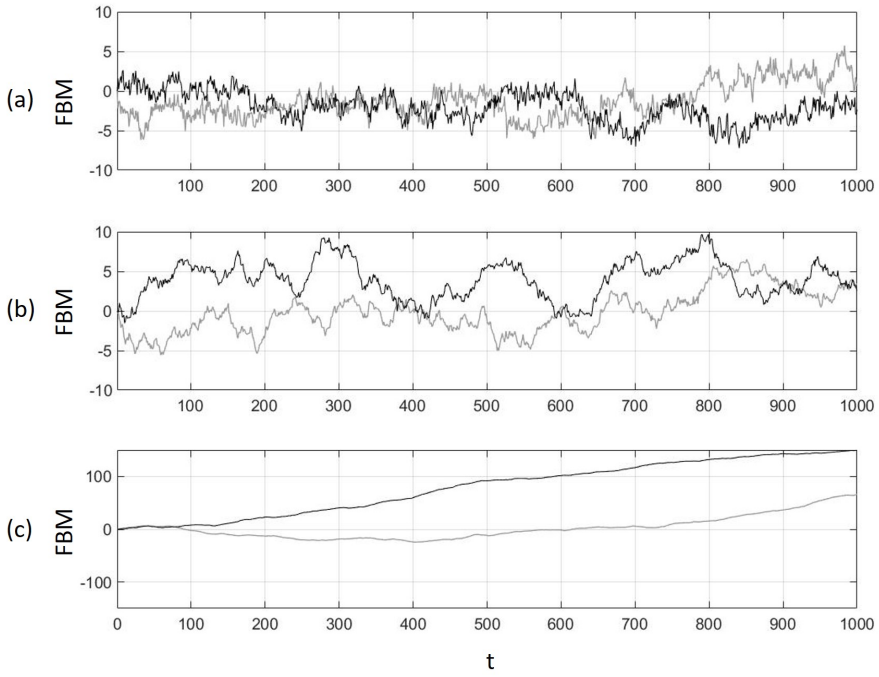

Figure B.4: Sample paths of the FBM: (a) $H = 0.2$, (b) $H = 0.5$, and (c) $H = 0.9$. The higher the Hurst value, the further the process can be. The different colour lines represents different sample paths.

B.4 Poisson process

A Poisson process is a well-known counting process. In this study, it is utilized to simulate the random occurrence of the coherent events. A Poisson process can be interpreted as a counting process denotes as $P(t), t \geq 0$. A counting process is used to count the total number of occurrences/ events that have occurred up to time t.

Definition B.4.1 (Poisson process)**.** A Poisson process is a counting process $P(t), t \geq 0$ with rate $\lambda > 0$ and the following properties:

(1). $P(0) = 0$ with probability 1

(2). The number of events is a Poisson random variable with mean equal to λt.

(3). $\{P(t),\ t \geq 0\}$ has independent increments

doi:10.6342/NTU202300192

The second property means, $\mathbb{E}[\{P(t)\}] = \lambda t$. A Poisson random variable will follow a Poisson distribution which is a probability mass function shown as,

$$\Pr\{P(t) = n\} = \frac{\lambda^n e^{-\lambda}}{n!}, \tag{B.7}$$

where $n = 0, 1, 2, ...$ is the number of the events that have happened. "!" is the factorial function.

The last property indicates that the interarrival times between events are independent. For an non-overlapping time $(t_1 < t_2 < t_3 < t_4)$, interarrival time is an exponential random variable with a mean $1/\lambda$. The second property implies the memoryless property of arriving events. In other words, the events occur randomly with a mean occurrence rate.

Simulation of a Poisson process

Since interarrival time between events in a Poisson process is independent of each other and is exponentially distributed, $\Pr\{\text{interarrival time} > t\} = \exp^{-\lambda t}$. Taking advantage of the memoryless property of interarrival time, accumulative sum of the random values drawn from a exponential distribution can be applied to simulate random arrivals of events as shown in Fig. B.5. By generating a random value from a exponential distribution, the first interarrival time $(t_1 - t_0)$ can be obtained. Then the arrival time of the first event t_1 is known. Repeat the steps, we can then use Poisson process to generate the random arrival process of the events.

doi:10.6342/NTU202300192

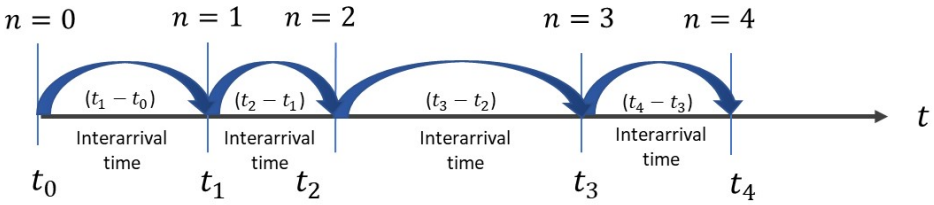

Figure B.5: Demonstration of random arrival process. n denotes the number of events.

doi:10.6342/NTU202300192

Appendix C — Stochastic differential equation (SDE)

C.1 SDE

A SDE is a differential equation with at least one term a stochastic process. In this appendix, we consider a one-dimensional Langevin equation that can describe the velocity change per unit mass due to forces impressed on a particle (Gardiner and others, 1985),

$$dX(t) = \mu(X(t), t) + \sigma(X(t), t)\xi(t)\,, \tag{C.1}$$

where $\mu(X(t), t)$ represents the velocity resulting from deterministic force and the second term on right-and side of the equation, $\sigma(X(t), t)\xi(t)$, denotes fluctuated velocity caused by the random force.

Let us first consider that the driving stochastic process is the Wiener process. The integration of the no-where differentiable stochastic process makes the same SDE have different names. The SDE is called an Ito SDE when the Ito stochastic integral is applied, while Stratonovich SDE represents the stochastic process integrated by Stratonovich integral. It is well-known that there is a *Ito-Stratonovich dilemma*. It points out that the very same SDE (Eq. C.1) might have different solutions depending on different stochastic

doi:10.6342/NTU202300192

integrals. The dilemma resides in the integral over the no-where differentiable stochastic process in the random term of the SDE. More specifically, for a non-constant diffusion coefficient, the Ito and Stratonovich interpretation of the same SDE can lead to different results.

C.1.1 Ito-Stratonovich dilemma

Consider the integration of a one-dimesional Langevin equation (Eq. C.1) in a time time $[t_0, t]$ with Ito and Stratonovich integral respectively,

$$X(t) = X(t_0) + \int_{t_0}^{t} \mu(X(s), s)ds + \int_{t_0}^{t} \sigma(X(s), s)dW(s), \tag{C.2}$$

$$X(t) = X(t_0) + \int_{t_0}^{t} \mu(X(s), s)ds + \int_{t_0}^{t} \sigma(X(s), s) \circ dW(s), \tag{C.3}$$

where the first integral is an ordinary Riemann integral. The key is the second integral $\int_{t_0}^{t} \sigma(X(s), s)dW(s)$. Because the sample path of a Wiener process is not differentiable, to deal with the problem, the Japanese mathematician, Kiyosi Ito, defined a new integral called *Ito stochastic integral* in the 1940s. Later in the 1960s, the Russian physicist R. L. Stratonovich proposed his stochastic integral known as *Stratonovich stochastic integral*. To distinct two different stochastic integrals, the symbol "$\circ$" is applied to denote the Stratonovich integral. Therefore, Eq. C.2 is often recognized as Ito SDE while Eq. C.3 is Stratonovich SDE.

The second key integral can be written in a general form as

$$\int_{t_0}^{t} \sigma(X(s), s)dW(s) = \lim_{\Delta \to 0} \sum_{k=0}^{m-1} \sigma(X(\tau_k), \tau_k)(W(t_{k+1}) - W(t_k)), \tag{C.4}$$

where $\Delta = (t_{k+1} - t_k)$ and τ_k denotes intermediary points, $\tau_k \in [t_{k+1} - t_k]$ for all

doi:10.6342/NTU202300192

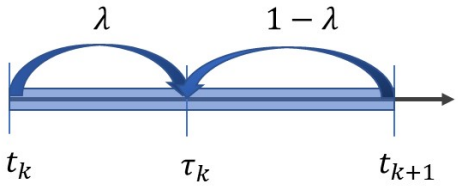

Figure C.1: The choice of τ_k, where the stochastic is evaluated.

$k \in \{0, 1, ..., n-1\}$. The different integral depends on different location choice of τ_k. For a Ito integral, $\tau_k = t_k$; while a Stratonovich is $\tau_k = (t_k + t_{k+1})/2$.

Example of the dilemma

Let's consider the integral ,

$$\int_{t_0}^{T} W(s)dW(s) \tag{C.5}$$

Set $\tau_k = (1-\lambda)t_k + \lambda t_{k+1}$, as shown in Fig. C.1. In this case, Ito integral has $\lambda = 0$ and Stratonovich has $\lambda = 1/2$. Then one can get,

$$\begin{aligned} \int_{t_0}^{T} W(s)dW(s) &= \lim_{m\to\infty} \sum_{k=0}^{m-1} W(\tau_k)(W(t_{k+1} - W(t_k)) \\ &= \frac{W(t)}{2} + (\lambda - \frac{1}{2})T\,. \end{aligned} \tag{C.6}$$

With the respective values of λ, the integration of Eq. C.5 becomes,

$$\int_{t_0}^{T} W(s)dW(s) = \frac{1}{2}W(t) - \frac{1}{2}T \tag{C.7}$$

$$\int_{t_0}^{T} W(s) \circ dW(s) = \frac{1}{2}W(t)\,. \tag{C.8}$$

It is clear, Eq. C.7 and Eq. C.8 are not the same. This example indicates using different stochastic integral on the same SDE, Ito and Stratonovich representations might not converge towards the same solution.

doi:10.6342/NTU202300192

C.1.2 Ito-Stratonovich drift correction formula

There is a correlation term known as *Ito-Stratonovich drift correction formula* that provide possibility to switch between the two different calculi.

$$dX(t) = \mu(X(t), t)dt + \sigma(X(t), t)dW(t) \tag{C.9}$$

$$dX(t) = \tilde{\mu}(X(t), t)dt + \sigma(X(t), t) \circ dW(t) \tag{C.10}$$

$$\tilde{\mu} = \mu - \frac{1}{2}\sigma'\sigma \tag{C.11}$$

where σ' is the first derivative of $\sigma(X(t), t)$. By using this correction in the drift term, the integration of the Stratonovich SDE can lead to the same result as the integration of the Ito SDE.

In the field of stochastic calculus, both the Ito and Stratonovich integrals have their respective advantages and disadvantages, and the choice between them is largely dependent on the specific requirements of the modeling problem at hand. In financial mathematics, the Ito interpretation is commonly utilized due to its inherent property of only taking into account information about the past. This property aligns with the underlying assumptions of financial models and is therefore well suited to financial applications. On the other hand, the Stratonovich interpretation is more frequently used in the physical sciences due to its better suitability for handling nonlinear systems and its closer relationship with classical calculus. However, the choice between the two integrals should be based on the specific needs of the modeling problem and the type of information that is available.

doi:10.6342/NTU202300192

Appendix D — SDE simulation

D.1 Convergence of numerical scheme

In the numerical methods, there are strong and weak convergence for accuracy. Strong convergence requires two stochastic processes are from the same random function. Weak convergence requires less strict condition. It only requires the characteristics of the stochastic state vector, such as statistical moments, remain the same as those found for the exact solution. The following definitions can be referred to Klebaner (2012).

Definition D.1.1 (Strong order of convergence)**.** Under suitable conditions of the SDE, for a fixed time T, the strong order of convergence is β_1 if there exist a positive constant K and a positive constant Δ such that $T = N\Delta t$:

$$\mathbb{E}\{|X(T) - \bar{X}(T_N)|\} \leq K(\Delta t)^{\beta_1}\,, \tag{D.1}$$

for all $0 < \Delta t < \Delta$. In Eq. D.1, $X(T)$ is the exact solution and $\bar{X}(T_N)$ the approximated solution. The strong concept measures the rate at which the mean of the error decays as $\Delta t \to 0$. While strong convergence requires a more stringent condition, if one only needs less demand of the convergence, such as the same distribution of the random process, this leads to the concept of weak convergence.

Definition D.1.2 (Weak order of convergence)**.** The weak order of convergence is β_2 if

doi:10.6342/NTU202300192

there exist a positive constant K and a positive constant Δ such that for a fixed time $T = N\Delta t$:

$$|\mathbb{E}\{f(X(T), T)\} - \mathbb{E}\{f(\bar{X}(T_N), T_N)\}| \leq K(\Delta t)^{\beta_2} \tag{D.2}$$

for all $0 < \Delta t < \Delta$ and for each functions f with polynomial growth.

D.2 Common numerical scheme

Note that the numerical schemes used to implement the Ito or Stratonovich SDE differ. Followings are some common ones.

D.2.1 Euler-Maruyama scheme

Euler-Maruyama scheme, also known as the Euler scheme, is a explicit scheme with a strong convergent order 0.5. It is a result of the stochastic Taylor expansion. It is a scheme for Ito SDE. The iterative form is shown as,

$$X_{n+1} = X_n + \mu(X_n)\Delta t + \sigma(X_n)\Delta W_n, \quad X_0 = x_0 \quad n = 0, 1, ..., N-1 \tag{D.3}$$

where $X_n = X(t_n)$, and $\Delta t = t_{n+1} - t_n$ is the step size, i.e., the fixed time step. For simulation, $\Delta W_n = [W_{t+\Delta t} - W_t] \sim \sqrt{\Delta t}\mathcal{N}(0, 1)$ with $W(t_0) = 0$.

From simplicity, the following notation is used: $\mu_n = \mu(X_n)$ and $\sigma_n = \sigma(X_n)$. Then Eq D.3 becomes,

$$X_{n+1} = X_n + \mu_n\Delta t + \sigma_n\Delta W_n\,. \tag{D.4}$$

Compared with Euler-Maruyama scheme, numerical scheme for Stratonovich SDE

doi:10.6342/NTU202300192

based on stochastic Taylor expansion is Euler-Heun scheme.

D.2.2 Euler-Heun scheme

For a Stratonovich SDE, instead of the Euler-Maruyama method, we should apply the Euler-Heun scheme,

$$X_{n+1} = X_n + \mu_n \Delta t + \frac{1}{2}\left[\sigma_n + \sigma(\bar{X}_n)\right] \Delta W_n, \tag{D.5}$$

where $\bar{X}_n = X_n + \sigma_n \Delta W_n$ and $\Delta W_n = [W_{t+\Delta t} - W_t] \sim \sqrt{\Delta t}\mathcal{N}(0,1)$.

D.2.3 Milstein scheme

The Milstein scheme is a explicit scheme with strong convergence order 1 to the solution of SDE. For a Ito SDE, the following Milstein scheme can be applied,

$$X_{n+1} = X_n + \mu_n \Delta t + \sigma_n \Delta W_n + \frac{1}{2}\sigma_n \sigma_n' [(\Delta W_n)^2 - \Delta t], \tag{D.6}$$

where where $\sigma_n' = \frac{\mathrm{d}\sigma(X_n)}{\mathrm{d}X_n}$ is the first derivative of σ_n. The Wiener process can be simulated by $\Delta W_n \& = [W_{t+h} - W_t] \sim \sqrt{\Delta t}\mathcal{N}(0,1)$.

For a Stratonovich SDE, on can use the following Milstein scheme,

$$X_{n+1} = X_n + \mu_n \Delta t + \sigma_n \Delta W_n + \frac{1}{2}\sigma_n \sigma_n' (\Delta W_n)^2. \tag{D.7}$$

Note that if the σ_n is constant and not a function of X_n, i.e., (additive noise), then both Ito and Stratonovich interpretations are equivalent because $\sigma_n' = 0$.

doi:10.6342/NTU202300192

doi:10.6342/NTU202300192

Notation

Stochastic processes

$\{X(t),\, t \in T\}$ / $\{\xi(t),\, t \in T\}$	an arbitrary stochastic process
$\{B^H(t),\, t \in T\}$	fractional Brownian motion process
$\{P(t),\, t \in T\}$	Poisson process with mean arrival rate λ
$\{W(t),\, t \in T\}$	Wiener process
$\{Y(t),\, t \in T\}$	fractional Gaussian noise

Math notations & dimensionless quantity

$\bar{\bullet}$	time-average value
$\langle \bullet \rangle$	ensemble average
$\mathbb{E}[\,\bullet\,]$	expected value of a random variable

doi:10.6342/NTU202300192

Cov(•)	covaraince function
ρ(•)	autocorrelation function
Pr{•}	probability
k^+	dimensionless turbulent kinetic energy, $k^+ = k/u_\tau^2$
u^+	dimensionless streamwise flow velocity, $u^+ = u/u_*$
Δt^+	event duration, where Δt_{cr}^+ is the threshold of a event duration
z^+	dimensionless vertical distance known as wall unit, $z^+ = zu_*/\nu$
$\tilde{z}$	dimensionless vertical distance, $\tilde{z} = z/h$
Re_*	shear Reynolds number, $\mathrm{Re}_* = u_* k_s/\nu$
Sc_t	Schmidt number
St	Stokes number

FUNCTIONS

$\boldsymbol{\mu}(\boldsymbol{X}(t), t)$	coefficient of drift term in Langevin equation	$[L^{-1}]$
$\boldsymbol{\sigma}_r(\boldsymbol{X}(t), t)$	coefficient of random/fluctuation term in Langevin equation	$[LT^{-1/2}]$
$\boldsymbol{X}(t)$	particle location at t, $\boldsymbol{X}(t) = \{X(t), Z(t)\}$	$[L]$

doi:10.6342/NTU202300192

δ_{ij}	the Kronecker delta, $\delta_{ij}(i=j)=1, \delta_{ij}(i\neq j)=0$	[–]

CONSTANT [UNIT]		**[UNIT]**
κ	the von Kármán constant	[–]
μ	fluid dynamic viscosity	$[ML^{-1}T^{-1}]$
ν	the kinematic viscosity	$[L^2T^{-1}]$
Π	Cole's wake parameter	[–]
ρ	flow density	$[ML^{-3}]$
h	water depth	$[L]$
k_s	effective sand roughness height	$[L]$
S_0	channel slope	[–]
u_*	shear velocity obtained from the momentum balance	$[LT^{-1}]$
u_τ	friction velocity	$[LT^{-1}]$
w_s	particle settling velocity	$[LT^{-1}]$
z_0	reference height	$[L]$

TENSOR	**[UNIT]**

doi:10.6342/NTU202300192

D_{ij}	diffusion coefficient in ADE	$[L^2T^{-1}]$
g_i	body force in i-direction	$[MLT^{-2}]$
u_i	the instantaneous flow velocity in i-direction	$[LT^{-1}]$
$\bar{u_i}$	the time-averaged flow velocity in i-direction.	$[LT^{-1}]$
u_i'	the velocity fluctuation in i-direction.	$[LT^{-1}]$
$\frac{\partial P}{\partial x_i}$	pressure gradient	$[ML^{-1}T^{-2}]$
$-\rho\overline{u_i'u_j'}$	Reynolds stress	$[ML^{-1}T^{-2}]$
λ_i	length scales of a bursting process	$[L]$

SCALAR AND COEFFICIENT		**[UNIT]**
C_{dfbm}	correction term for discrete FBM simulation	$[T]$
Δt	time step	$[T]$
γ_x, γ_z	the scaling diffusion exponents in x and z directions	$[-]$
γ_η	convergent rate of the modified Euler numerical scheme	$[-]$
μ_t	eddy viscosity	$[ML^{-1}T^{-1}]$
ν_t	turbulent diffusivity	$[L^2T^{-1}]$

doi:10.6342/NTU202300192

τ	total stress	$[ML^{-1}T^{-2}]$
τ_0	bed stress	$[ML^{-1}T^{-2}]$
$\varepsilon_x, \varepsilon_z$	particle diffusivity in x and z directions	$[L^2T^{-1}]$
c	concentration	$[-]$
k	turbulent kinetic energy	$[L^2T^{-2}]$
l	Prandtl mixing length	$[L]$
p	probability	$[-]$
r	particle displacement	$[L]$
t_b	duration of a bursting process	$[T]$

doi:10.6342/NTU202300192

doi:10.6342/NTU202300192

Abbreviation

ADE	advection diffusion equation
ADV	acoustic Doppler velocimeters
DNS	direct numerical simulation
FBM	fractional Brownian motion/ fractional Brownian process
FSD-PTM	fractional stochastic diffusion particle tracking model
HRV	Heart rate variability
LSM	large scale motion
NBS	neutrally-buoyant sand
NS	natural sand
PDF	probability density function

doi:10.6342/NTU202300192

PIV	particle image velocimetry
PTV	particle tracking velocimetry
PTM	particle tracking model
TKE	turbulence kinetic energy
RANS	Reynolds averaged Navier-Stokes equation
SDE	stochastic differential equation
SD-PTM	stochastic diffusion particle tracking model

doi:10.6342/NTU202300192

References

Absi, R. (2019). Eddy viscosity and velocity profiles in fully-developed turbulent channel flows. Fluid Dynamics, 54(1):137–147.

Absi, R. (2021). Analytical eddy viscosity model for velocity profiles in the outer part of closed- and open-channel flows. Fluid Dynamics, 56(4):577–586.

Absi, R., Marchandon, S., and Lavarde, M. (2011). Turbulent diffusion of suspended particles: analysis of the turbulent Schmidt number. In Defect and diffusion forum, volume 312, pages 794–799. Trans Tech Publ.

Agrawal, R., Ng, H. C.-H., Davis, E. A., Park, J. S., Graham, M. D., Dennis, D. J. C., and Poole, R. J. (2020). Low-and high-drag intermittencies in turbulent channel flows. Entropy, 22(10):1126.

Ancey, C. and Pascal, I. (2020). Estimating mean bedload transport rates and their uncertainty.

Argall, R., Sanders, B. F., and Poon, Y.-K. (2004). Random-walk suspended sediment transport and settling model. In Estuarine and Coastal Modeling (2003), pages 713–730.

Bagherimiyab, F. and Lemmin, U. (2018). Large-scale coherent flow structures in rough-

doi:10.6342/NTU202300192

bed open-channel flow observed in fluctuations of three-dimensional velocity, skin friction and bed pressure. Journal of Hydraulic Research, 56(6):806–824.

Biagini, F., Hu, Y., Øksendal, B., and Zhang, T. (2008). Stochastic calculus for fractional Brownian motion and applications. Springer Science & Business Media.

Borgas, M. S. and Sawford, B. L. (1994). A family of stochastic models for two-particle dispersion in isotropic homogeneous stationary turbulence. Journal of fluid mechanics, 279:69–99.

Bose, S. K. and Dey, S. (2010). Universal probability distributions of turbulence in open channel flows. Journal of Hydraulic Research, 48(3):388–394.

Bose, S. K. and Dey, S. (2013). Sediment entrainment probability and threshold of sediment suspension: exponential-based approach. Journal of Hydraulic Engineering, 139(10):1099–1106.

Boussinesq, J. (1877). Essai sur la théorie des eaux courantes, volume 2. Imprimerie nationale.

Brandt, L. and De Lange, H. C. (2008). Streak interactions and breakdown in boundary layer flows. Physics of fluids, 20(2):24107.

Cellino, M. and Lemmin, U. (2004). Influence of coherent flow structures on the dynamics of suspended sediment transport in open-channel flow. Journal of Hydraulic Engineering, 130(11):1077–1088.

Chen, X., Iwano, K., Sakai, Y., and Ito, Y. (2021). Effect of large-scale structures on

doi:10.6342/NTU202300192

bursting phenomenon in turbulent boundary layer. International Journal of Heat and Fluid Flow, 89:108811.

Cheng, N.-S. and Chiew, Y.-M. (1998). Modified logarithmic law for velocity distribution subjected to upward seepage. Journal of Hydraulic Engineering, 124(12):1235–1241.

Chien, N. and Wan, Z. (1999). Mechanics of sediment transport.

Coleman, N. L. (1986). Effects of suspended sediment on the open-channel velocity distribution. Water Resources Research, 22(10):1377–1384.

Coles, D. (1956). The law of the wake in the turbulent boundary layer. Journal of Fluid Mechanics, 1(2):191–226.

Davidson, L. (2015). Fluid mechanics, turbulent flow and turbulence modeling.

Delignières, D. (2015). Correlation Properties of (Discrete) Fractional Gaussian Noise and Fractional Brownian Motion. Mathematical Problems in Engineering, 2015:485623.

Dennis, D. J. C. (2015). Coherent structures in wall-bounded turbulence. Anais da Academia Brasileira de Ciências, 87:1161–1193.

Dey, S. (2014). Turbulence in open-channel flows BT - fluvial hydrodynamics: hydrodynamic and sediment transport phenomena. pages 95–187. Springer Berlin Heidelberg, Berlin, Heidelberg.

Dimou, K. N. and Adams, E. E. (1993). A random-walk, particle tracking model for well-mixed estuaries and coastal waters. Estuarine, Coastal and Shelf Science, 37(1):99–110.

Einstein, H. A. (1950). The bed-load function for sediment transportation in open channel flows, volume 1026. Citeseer.

doi:10.6342/NTU202300192

Einstein, H. A. and El-Samni, E.-S. A. (1949). Hydrodynamic forces on a rough wall. Reviews of Modern Physics, 21(3):520–524.

Elder, J. W. (1959). The dispersion of marked fluid in turbulent shear flow. Journal of fluid mechanics, 5(04):544–560.

Elhakeem, M., Papanicolaou, A. N. T., and Tsakiris, A. G. (2017). A probabilistic model for sediment entrainment: The role of bed irregularity. International Journal of Sediment Research, 32(2):137–148.

Fischer, H. B. (1966). Longitudinal dispersion in laboratory and natural streams. California Institute of Technology.

Flandrin, P. (1992). Wavelet analysis and synthesis of fractional Brownian motion. IEEE Transactions on information theory, 38(2):910–917.

Follett, E., Chamecki, M., and Nepf, H. (2016). Evaluation of a random displacement model for predicting particle escape from canopies using a simple eddy diffusivity model. Agricultural and Forest Meteorology, 224:40–48.

Furbish, D. J., Fathel, S. L., Schmeeckle, M. W., Jerolmack, D. J., and Schumer, R. (2017). The elements and richness of particle diffusion during sediment transport at small timescales. Earth Surface Processes and Landforms, 42(1):214–237.

Gardiner, C. W. and others (1985). Handbook of stochastic methods, volume 3. springer Berlin.

Heemink, A. W. (1990). Stochastic modelling of dispersion in shallow water. Stochastic Hydrology and hydraulics, 4(2):161–174.

doi:10.6342/NTU202300192

Hu, Y., Liu, Y., and Nualart, D. (2016). Rate of convergence and asymptotic error distribution of Euler approximation schemes for fractional diffusions. 26(2).

Hurst, H. E. (1957). A suggested statistical model of some time series which occur in nature. Nature, 180(4584):494.

Israelsson, P. H., Kim, Y. D., and Adams, E. E. (2006). A comparison of three Lagrangian approaches for extending near field mixing calculations. Environmental Modelling & Software, 21(12):1631–1649.

Jackson, R. G. (1976). Sedimentological and fluid-dynamic implications of the turbulent bursting phenomenon in geophysical flows. Journal of Fluid Mechanics, 77(3):531–560.

Jiménez, J. (2018). Coherent structures in wall-bounded turbulence. Journal of Fluid Mechanics, 842.

Kaftori, D., Hetsroni, G., and Banerjee, S. (1995a). Particle behavior in the turbulent boundary layer. I. Motion, deposition, and entrainment. Physics of Fluids, 7(5):1095–1106.

Kaftori, D., Hetsroni, G., and Banerjee, S. (1995b). Particle behavior in the turbulent boundary layer. II. Velocity and distribution profiles. Physics of Fluids, 7(5):1107–1121.

Keylock, C. J., Lane, S. N., and Richards, K. S. (2014). Quadrant/octant sequencing and the role of coherent structures in bed load sediment entrainment. Journal of Geophysical Research: Earth Surface, 119(2):264–286.

doi:10.6342/NTU202300192

Klebaner, F. C. (2012). Introduction to stochastic calculus with applications. World Scientific Publishing Company.

Kline, S. J., Reynolds, W. C., Schraub, F. A., and Runstadler, P. W. (1967). The structure of turbulent boundary layers. Journal of Fluid Mechanics, 30(4):741–773.

Lee, J., Lee, J. H., Choi, J.-I., and Sung, H. J. (2014). Spatial organization of large- and very-large-scale motions in a turbulent channel flow. Journal of Fluid Mechanics, 749:818–840.

Liu, W.-J. (2021). Incorporating backward forward stochastic particle tracking model into the EFDC model for probable sedimentation source identification in typhoon event. Technical Report 2021, National Taiwan University.

Liu, Y. and Tindel, S. (2019). First-order Euler scheme for SDEs driven by fractional Brownian motions: The rough case. The Annals of Applied Probability, 29(2):758–826.

Lu, S. S. and Willmarth, W. W. (1973). Measurements of the structure of the Reynolds stress in a turbulent boundary layer. Journal of Fluid Mechanics, 60(3):481–511.

Man, C. and Tsai, C. W. (2007). Stochastic partial differential equation-based model for suspended sediment transport in surface water flows. Journal of engineering mechanics, 133(4):422–430.

Mandelbrot, B. B. and Van Ness, J. W. (1968). Fractional Brownian motions, fractional noises and applications. SIAM review, 10(4):422–437.

Mandelbrot, B. B. and Wallis, J. R. (1969). Some long-run properties of geophysical records. Water resources research, 5(2):321–340.

doi:10.6342/NTU202300192

Martin, R. L., Jerolmack, D. J., and Schumer, R. (2012). The physical basis for anomalous diffusion in bed load transport. Journal of Geophysical Research: Earth Surface, 117(F1).

Mathieu, A., Chauchat, J., Bonamy, C., Balarac, G., and Hsu, T.-J. (2021). A finite-size correction model for two-fluid large-eddy simulation of particle-laden boundary layer flow. Journal of Fluid Mechanics, 913.

McKeon, B. J. (2017). The engine behind (wall) turbulence: perspectives on scale interactions. Journal of Fluid Mechanics, 817:P1.

Metzler, R. and Klafter, J. (2004). The restaurant at the end of the random walk: Recent developments in the description of anomalous transport by fractional dynamics. Journal of Physics A: Mathematical and General, 37(31):R161.

Muste, M., Yu, K., Fujita, I., and Ettema, R. (2005). Two-phase versus mixed-flow perspective on suspended sediment transport in turbulent channel flows. Water Resources Research, 41(10).

Muste, M., Yu, K., Fujita, I., and Ettema, R. (2009). Two-phase flow insights into open-channel flows with suspended particles of different densities. Environmental fluid mechanics, 9(2):161–186.

Nakagawa, H. and Nezu, I. (1981). Structure of space-time correlations of bursting phenomena in an open-channel flow. Journal of Fluid Mechanics, 104:1–43.

Nezu, I. (1993). Turbulence in open-channel flows. IAHR-monograph.

Nikora, V., Habersack, H., Huber, T., and McEwan, I. (2002). On bed particle diffusion in

doi:10.6342/NTU202300192

gravel bed flows under weak bed load transport. Water Resources Research, 38(6):11–17.

Nikuradse, J. (1932). Gesetzmassigkeiten der turbulenten Stromung in glatten Rohren. Ver Deutsch. Ing. Forschungsheft, 356.

Ninto, Y. and Garcia, M. H. (1996). Experiments on particle—turbulence interactions in the near‐wall region of an open channel flow: Implications for sediment transport. 326:285–319.

Noguchi, K. and Nezu, I. (2009). Particle-turbulence interaction and local particle concentration in sediment-laden open-channel flows. Journal of Hydro-environment Research, 3(2):54–68.

Oh, J. and Tsai, C. W. (2010). A stochastic jump diffusion particle-tracking model (SJD-PTM) for sediment transport in open channel flows. Water Resources Research, 46(10).

Oksendal, B. (2013). Stochastic differential equations: an introduction with applications. Springer Science & Business Media.

Ölçmen, S. M., Simpson, R. L., and Newby, J. W. (2006). Octant analysis based structural relations for three-dimensional turbulent boundary layers. Physics of Fluids, 18(2):025106.

Pierce, J. K. and Hassan, M. A. (2020). Back to Einstein: Burial-induced three-range diffusion in fluvial sediment transport. Geophysical Research Letters, 47(15):e2020GL087440.

Pipiras, V. and Taqqu, M. S. (2017). Long-range dependence and self-similarity, volume 45 of Cambridge Series in Statistical and Probabilistic Mathematics.

doi:10.6342/NTU202300192

Prandtl, L. (1925). Bericht über Untersuchungen zur ausgebildeten Turbulenz. ZAMM-Journal of Applied Mathematics and Mechanics/Zeitschrift für Angewandte Mathematik und Mechanik, 5(2):136–139.

Pusey, P. N. (2011). Brownian motion goes ballistic. Science, 332(6031):802–803.

Reynolds, O. (1895). On the dynamical theory of incompressible viscous fluids and the determination of the criterion. Philosophical Transactions of the Royal Society of London. (A.), 186:123–164.

Risken, H. (1989). The Fokker-Planck equation. Methods of solution and applications.

Robinson, S. K. (1991). Coherent motions in the turbulent boundary layer. Annual Review of Fluid Mechanics, 23(1):601–639.

Salim, S. and Pattiaratchi, C. (2020). Sediment resuspension due to near-bed turbulent coherent structures in the nearshore. Continental Shelf Research, 194:104048.

Salim, S., Pattiaratchi, C., Tinoco, R., Coco, G., Hetzel, Y., Wijeratne, S., and Jayaratne, R. (2017). The influence of turbulent bursting on sediment resuspension under unidirectional currents. Earth Surface Dynamics, 5(3):399–415.

Shin, J., Seo, J. Y., and Seo, I. W. (2020). Longitudinal dispersion coefficient for mixing in open channel flows with submerged vegetation. Ecological Engineering, 145:105721.

Smith, C. R. and Metzler, S. P. (1983). The characteristics of low-speed streaks in the near-wall region of a turbulent boundary layer. Journal of Fluid Mechanics, 129:27–54.

Smith C (1996). Coherent flow structures in smooth-wall turbulent boundary layers: Facts, mechanisms and speculation. Coherent Flow Structures in Open Channels, page 1.

doi:10.6342/NTU202300192

Subhasish, D., Zeeshan, A. S., and Ellora, P. (2020). Hydrodynamic lift on sediment particles at entrainment: Present status and its prospect. Journal of Hydraulic Engineering, 146(6):3120001.

Thomson, D. J. (1987). Criteria for the selection of stochastic models of particle trajectories in turbulent flows. Journal of Fluid Mechanics, 180:529–556.

Tsai, C. W. and Huang, S. (2019). Modeling suspended sediment transport under influence of turbulence ejection and sweep events. Water Resources Research, 55(7):5379–5393.

Tsai, C. W., Huang, S.-H., and Hung, S. Y. (2021). Incorporating the memory effect of turbulence structures into suspended sediment transport modeling. Water Resources Research, 57(3):e2020WR028475.

Tsai, C. W., Hung, S. Y., and Oh, J. (2018). A stochastic framework for modeling random-sized batch arrivals of sediment particles into open channel flows. Stochastic Environmental Research and Risk Assessment, 32(7):1939–1954.

Tsai, C. W., Hung, S. Y., and Wu, T.-H. (2020). Stochastic sediment transport: anomalous diffusions and random movement. Stochastic Environmental Research and Risk Assessment, 34(2):397–413.

Volino, R. J. and Simon, T. W. (1994). An application of octant analysis to turbulent and transitional flow data.

Wu, F.-C. and Chou, Y.-J. (2003). Rolling and lifting probabilities for sediment entrainment. Journal of Hydraulic Engineering, 129(2):110–119.

Wu, F.-C. and Lin, Y.-C. (2002). Pickup probability of sediment under log-normal velocity distribution. Journal of Hydraulic Engineering, 128(4):438–442.

doi:10.6342/NTU202300192

Yeragani, V. K., Pohl, R., Berger, R., Balon, R., Ramesh, C., Glitz, D., Srinivasan, K., and Weinberg, P. (1993). Decreased heart rate variability in panic disorder patients: A study of power-spectral analysis of heart rate. Psychiatry Research, 46(1):89–103.

doi:10.6342/NTU202300192